Electronic Structure of the Reduced Blue Copper Active Site: Contributions to Reduction Potentials and Geometry

Jeffrey A. Guckert, Michael D. Lowery, and Edward I. Solomon*

Contribution from the Department of Chemistry, Stanford University, Stanford, California 94305

Received November 17, 1994[⊗]

Abstract: A detailed electronic structure description of the reduced blue copper active site has now been developed. To date, the Cu(I) $3d^{10}$ oxidation state of this site has been generally inaccessible to the spectroscopic techniques commonly employed in the extensive studies of the open shell, oxidized blue copper active site. Photoelectron spectroscopy (PES) of imidazole, dimethyl sulfide, and methanethiolate bound to Cu(I) sites at single crystal surfaces has been used to define normal Cu(I) bonding to ligands relevant to the blue copper site. Variable photon energy PES has been used to assign valence band spectra, assess metal−ligand covalency, and probe specific orbital contributions to Cu(I) bonding. Self Consistent Field-Xα-Scattered Wave (SCF-Xα-SW) molecular orbital calculations calibrated to the photoelectron spectra have been performed to quantitatively complement the experimental bonding descriptions. These calculations have been extended to the reduced blue copper active site in plastocyanin, the prototypical blue copper protein, to detail the electronic structure changes that occur relative to normal Cu(I) bonding and upon oxidation. It is found that the weakened axial interaction associated with the elongated Cu−thioether bond is compensated by a strong Cu−thiolate equatorial π bond, which activates the cysteine residue as an effective superexchange pathway for electron transfer. The metal−ligand bonding at the reduced blue copper site is found to be dominated by ligand p → Cu(I) 4p charge transfer. Upon oxidation new Cu 3d bonding contributions arise as a result of the hole created in the Cu(II) $3d_{x^2-y^2}$ orbital. In particular, the thiolate S π orbital exhibits significant overlap with the $d_{x^2-y^2}$ orbital, which leads to a considerable increase in the thiolate π donor strength of the Cu−S(thiolate) bond. Ionization energies have been used to estimate the electronic structure contributions to the reduction potential. The long Cu−thioether axial bond present at the active site destabilizes the oxidized state and is therefore a key determining factor in the high reduction potentials generally observed for blue copper proteins. Linear coupling terms have been evaluated for the distortions of a blue copper site unconstrained by the protein backbone. The geometry changes which occur in the blue copper site upon oxidation are found to be consistent with the changes in the electronic structure. Therefore, the reduced Cu(I) geometry is not imposed on the oxidized site by the protein environment. Rather, the structural constraints due to the protein matrix are present in the reduced site, where the long Cu−thioether bond lowers the site symmetry and eliminates the electronic degeneracy of the ground state and, thus, the Jahn−Teller distortion that would normally occur upon oxidation. As a result the geometric changes are small, giving rise to a low Franck−Condon barrier to electron transfer.

I. Introduction

Ubiquitous in nature, blue copper proteins function as rapid, long-range electron-transfer centers in biological systems. It has long been a goal to understand the electronic origins of the unique spectral features of these centers and to relate them to the redox properties of the proteins. Blue copper proteins containing a single metal active site most notably include the plastocyanins, azurins, amicyanin, stellacyanin, and cucumber basic blue. In addition, the blue copper center is found in multicopper proteins such as nitrite reductase, nitrous oxide reductase, ascorbate oxidase, laccase, and ceruloplasmin.

The active site structure of oxidized poplar plastocyanin (*Populus nigra*) has been defined by Freeman *et al.*[1] and serves as a useful geometric prototype of the blue copper center. In the plastocyanin active site, the copper ion is at the center of a C_{3v} elongated pseudotetrahedral coordination sphere. The Cu ion is ~0.36 Å above the NNS plane of the three equatorial ligands—two histidine (His) residues at 1.92 and 2.04 Å, and a cysteine (Cys) residue at 2.07 Å. Bound axially to the Cu ion, approximately along the trigonal (z) axis, is a methionine (Met) amino acid at an unusually long bond length of 2.82 Å. EPR studies,[2] in conjunction with ligand-field calculations,[3,4] have identified the Cu $3d_{x^2-y^2}$ as the half-occupied ground-state orbital, oriented approximately in the NNS equatorial plane. These studies also demonstrate that the g_z direction of the site is ~5° off the Cu−S(Met) bond. The crystal structures reported for other blue copper proteins, including algal plastocyanin,[5] several azurins,[6−9] nitrite reductase,[10−12] and ascorbate oxidase,[13]

[⊗] Abstract published in *Advance ACS Abstracts*, February 15, 1995.

(1) Guss, J. M.; Bartunk, H. D.; Freeman, H. C. *Acta Crystallogr.* **1992**, *B48*, 790−811.

(2) Penfield, K. W.; Gay, R. R.; Himmelwright, R. S.; Eickman, N. C.; Norris, V. A.; Freeman, H. C.; Solomon, E. I. *J. Am. Chem. Soc.* **1981**, *103*, 4382−8.

(3) Solomon, E. I.; Hare, J. W.; Dooley, D. M.; Dawson, J. H.; Stephens, P. J.; Gray, H. B. *J. Am. Chem. Soc.* **1980**, *102*, 168.

(4) Solomon, E. I.; Hare, J. W.; Gray, H. B. *Proc. Natl. Acad. Sci. U.S.A.* **1976**, *73*, 1389−92.

(5) Collyer, C. A.; Guss, J. M.; Freeman, H. C. *J. Mol. Biol.* **1990**, *211*, 617.

(6) Baker, E. N. *J. Mol. Biol.* **1988**, *203*, 1071.

(7) Shepard, W. E. B.; Anderson, B. F.; Lewandoski, D. A.; Norris, G. E.; Baker, E. N. *J. Am. Chem. Soc.* **1990**, *112*, 7817−9.

(8) Nar, H.; Messerschmidt, A.; Huber, R.; van de Kamp, M.; Canters, G. W. *J. Mol. Biol.* **1991**, *221*, 765−72.

(9) Zhu, D. W.; Dahms, T.; Willis, K.; Szabo, A. G.; Lee, X. *Arch. Biochem. Biophys.* **1994**, *308*, 469−70.

(10) Coyle, C. L.; Zumft, W. G.; Kroneck, P. M. H.; Korner, H.; Jakob, W. *Eur. J. Biochem.* **1985**, *153*, 459−67.

(11) Godden, J. W.; Turley, S.; Teller, D. C.; Adman, E. T.; Liu, M. Y.; Payne, W. J.; LeGall, J. *Science* **1991**, *253*, 438−42.

0002-7863/95/1517-2817$09.00/0

all exhibit a highly conserved active site geometry similar to that of poplar plastocyanin.

The geometry of the blue copper active site gives rise to unique spectroscopic features in the EPR and absorption spectra.[14-23] Most notably, an unusually small parallel hyperfine splitting is observed in the EPR spectrum ($\sim 65 \times 10^{-4}$ cm^{-1} for plastocyanin) relative to that of normal Cu(II) systems ($\sim 170 \times 10^{-4}$ cm^{-1}), and an exceptionally intense low-energy band is observed in the absorption spectrum at 600–630 nm ($\epsilon \approx 5000$ M^{-1} cm^{-1}) that is not found in the spectra of normal Cu(II) complexes. The small EPR hyperfine splitting has been ascribed to the extremely high covalency of the oxidized Cu $3d_{x^2-y^2}$ HOMO,[24] which from X-ray absorption spectroscopy (XAS) at the S K-edge[25] and Cu L-edge[26] contains 38% S character and only ~40% Cu character. From low-temperature MCD, the intense 600-nm "blue band" in the oxidized blue copper electronic absorption spectrum has been attributed to a strong S(Cys)p $\rightarrow$ Cu $3d_{x^2-y^2}$ π charge transfer (CT) transition,[27] while the Cys σ charge transfer at higher energy is much weaker. The blue copper absorption spectrum is in sharp contrast to the spectra of normal Cu(II) systems which exhibit weak low-energy π CT bands and higher energy, intense σ CT transitions. Self Consistent Field-Xα-Scattered Wave (SCF-Xα-SW) calculations, calibrated to experimental blue copper g values, reveal that the covalency of the Cu $3d_{x^2-y^2}$ HOMO is highly anisotropic, with the SCF-Xα-SW derived HOMO wave function composed of 42% Cu (in agreement with XAS experiments), 36% S(Cys), and <2% each of the His nitrogens.[27] The strong π interaction of S(Cys) with the Cu ion orients the Cu $3d_{x^2-y^2}$ orbital so that the Cu–S(Cys) bond axis bisects the lobes of this Cu d orbital, leading to the inverted π/σ intensity pattern in the absorption spectrum and providing a favorable superexchange pathway for electron transfer through the cysteine residue.

In the present study we address the electronic structure of the *reduced* blue copper active center as it relates to normal Cu(I) bonding and the electronic effects on the reduction potential and the geometry of the site. The reduction potentials of blue copper proteins are generally quite high (200–780 mV), favoring the reduced Cu(I) oxidation state. To date, the high potentials of these proteins have been ascribed to the approximate T_d geometry of the oxidized state and the presence of the soft thioether and thiolate sulfur ligands.[28-31] In the reduced X-ray crystal structure of poplar plastocyanin the Cu–Met bond length is 2.9 Å, the Cu–Cys bond length is 2.10 Å, and the Cu–His bonds are 2.25 and 2.12 Å. EXAFS on the reduced site has placed the average Cu–His distance closer to the Cu(I) ion at 2.05 Å. In addition to the general contraction of the bonds on oxidation, a small angular distortion is also observed, wherein the Cu ion is shifted slightly toward the NNS equatorial plane. The relatively small distortions of the site on oxidation have been attributed to an entatic or rack state of the protein imposing the reduced Cu(I) geometry on the oxidized site.[32-35]

A detailed investigation of the reduced site, similar in scope to the extensive studies of the oxidized site, has been limited to this point by the fact that most of the usual spectroscopic techniques employed to probe the oxidized site (EPR, absorption spectroscopy, etc.) are not effective for studying the closed shell Cu(I) d^{10} system. The exception is high-energy XAS at the Cu K-edge, but XAS is a lower-resolution method that yields limited bonding information. In this study, we have used synchrotron radiation photoelectron spectroscopy (PES) in conjunction with SCF-Xα-SW molecular orbital calculations to define the electronic structure of the reduced blue copper active site.

While PES allows the study of the valence levels of closed shell systems, electron-yield photoelectron experiments on protein active sites are somewhat limited. The metal ion of the active site is often buried within the protein structure, deeper than the escape depth of the photoelectron.[36] Additionally, the small number of metal ions in the protein relative to the abundance of organic atoms complicates the distinction of metal ionizations in the low-energy, valence-orbital region of the photoemission spectrum. Therefore, we have studied simpler systems, involving small molecules chemisorbed to coordinatively unsaturated Cu(I) sites at single-crystal surfaces to model the individual bonding interactions found at the blue copper active site. Specifically, we have investigated imidazole and dimethyl thioether bound to the CuCl(111) surface as a model of Cu(I)–histidine and Cu(I)–methionine interactions, and methanethiol bound to the Cu_2O(111) surface as a model of Cu(I)–cysteine interactions. The CuCl(111) surface consists of coordinatively unsaturated C_{3v} Cu(I) sites in a tetrahedral geometry with the axial coordination site vacant. The nonpolar Cu_2O(111) surface consists of coordinatively unsaturated Cu(I) and oxide sites. The Cu_2O(111) surface was chosen for methanethiol adsorption experiments because the oxide sites of this surface act as Brønsted basic centers which have been shown to facilitate the deprotonation of acidic adsorbates such as CH_3OH and H_2S.[37]

Using synchrotron radiation, variable photon energy PES permits the assignment of valence band spectra and the

(12) Jin, H.; Thomann, H.; Coyle, C. L.; Zumft, W. G. *J. Am. Chem. Soc.* **1989**, *111*, 4262–9.
(13) Messerschmidt, A.; Ladenstein, R.; Huber, R.; Bolognesi, M.; Avigliano, L.; Petruzzelli, R.; Rossi, A.; Finazzi-Agro, A. *J. Mol. Biol.* **1992**, *224*, 179–205.
(14) Blumberg, W. E.; Peisach, J. *Biochim. Biophys. Acta* **1966**, *126*, 269.
(15) Brill, A. S.; Bryce, G. F. *J. Chem. Phys.* **1968**, *48*, 4398–404.
(16) Fee, J. A. *Struct. Bonding* **1975**, *23*, 1–60.
(17) Gray, H. B.; Solomon, E. I. In *Copper Proteins*; Spiro, T. G., Ed.; Wiley: New York, 1981; pp 1–39.
(18) Solomon, E. I. In *Copper Coordination Chemistry: Biochemical and Inorganic Perspectives*; Karlin, K., Zubieta, J., Eds.; Adenine Press: Guilderland, NY, 1982; pp 1–22.
(19) Solomon, E. I.; Penfield, K. W.; Wilcox, D. E. *Struct. Bonding (Berlin)* **1983**, *53*, 1–57.
(20) Dorfman, R.; Bereman, X.; Whango, M. In *Copper Coordination Chemistry: Biochemical and Inorganic Perspectives*; Karlin, K., Zubieta, J., Eds.; Adenine Press: Guilderland, NY, 1982.
(21) Blair, D. F.; Campbell, G. W.; Schoonover, J. R.; Chan, S. I.; Gray, H. B.; Malmstrom, B. G.; Pecht, I.; Swanson, B. I.; Woodruff, W. H.; Cho, W. K.; English, A. M.; Fry, H. A.; Lum, V.; Norton, K. A. *J. Am. Chem. Soc.* **1985**, *107*, 5755–66.
(22) Roberts, J. E.; Cline, J. F.; Lum, V.; Freeman, H. C.; Gray, H. B.; Reisach, J.; Reinhammer, B.; Hoffman, B. *J. Am. Chem. Soc.* **1984**, *106*, 5324.
(23) Scott, R. A.; Hahn, J. E.; Boniach, S.; Freeman, H. C.; Hodgson, K. O. *J. Am. Chem. Soc.* **1985**, *107*, 5755.
(24) Penfield, K. W.; Gewirth, A. A.; Solomon, E. I. *J. Am. Chem. Soc.* **1985**, *107*, 4519–29.
(25) Shadle, S. E.; Penner-Hahn, J. E.; Schugar, H. J.; Hedman, B.; Hodgson, K. O.; Solomon, E. I. *J. Am. Chem. Soc.* **1993**, *115*, 767–76.
(26) George, S. J.; Lowery, M. D.; Solomon, E. I.; Cramer, S. P. *J. Am. Chem. Soc.* **1993**, *115*, 2968–9.
(27) Gewirth, A. A.; Solomon, E. I. *J. Am. Chem. Soc.* **1988**, *110*, 3811–9.
(28) Zanello, P. *Comm. Inorg. Chem.* **1988**, *8*, 45–78.
(29) Augustin, M. A.; Yandell, J. K.; Addison, A. W.; Karlin, K. D. *Inorg. Chim. Acta* **1981**, *55*, L35–L37.
(30) Karlin, K. D.; Yandell, J. K. *Inorg. Chem.* **1984**, *23*, 1184–8.
(31) Sakaguchi, U.; Addison, A. W. *J. Chem. Soc., Dalton Trans.* **1979**, 600–8.
(32) Lumry, R.; Eyring, H. *J. Phys. Chem.* **1954**, *58*, 110–20.
(33) Williams, R. J. P. *J. Mol. Catal.* **1985**, *30*, 1–26.
(34) Malmström, B. G. *Eur. J. Biochem.* **1994**, *223*, 711–8.
(35) Gray, H. B.; Malmström, B. G. *Comm. Inorg. Chem.* **1983**, *II*, 203–9.
(36) Seah, M. P.; Dench, W. A. *SIA, Surf. Interface Anal.* **1979**, *1*, 2–11.
(37) Lin, J.; May, J. A.; Didziulis, S.; Solomon, E. I. *J. Am. Chem. Soc.* **1992**, *114*, 4718–27.

determination of specific orbital contributions to the ligand bonding with the Cu(I) sites. The photoemission intensity is largely dependent on the photoionization cross sections associated with the atomic orbitals contributing to the molecular orbital that is ionized. Ligand 2p/3p contributions can be distinguished from metal 3d contributions as a result of the significant difference in the cross sections of these orbitals through photon energies of 25−100 eV.[38,39] Ratios of peak intensity may then be used to evaluate relative metal−ligand covalencies in the valence molecular orbitals. In the valence band photoelectron spectra of CuCl and Cu_2O, shake-up satellite peaks are observed, corresponding to a $3d^{10}$ ionization plus a Cu 3p → Cu 4s, transition.[40−42] The intensity of these satellites is resonance enhanced at photon energies corresponding to the Cu M-edge; therefore, the position of the satellite resonance intensity maximum can be used as a probe of the Cu 4s bonding interaction with the chemisorbed ligand.[43] Satellite structure may also arise in the ligand core XPS, associated with the direct ionization of a core electron plus a charge transfer from a neighboring atomic center that compensates for the positive charge associated with the core hole. Therefore, the intensity of the core satellite corresponds to the extent of Cu(I) → ligand charge transfer and reflects the strength of metal-to-ligand back bonding involved in the Cu(I)−L bond.[43−48]

SCF-Xα-SW calculations have been performed on $[Im-CuCl_3]^{2-}$, $[(CH_3)_2S-CuCl_3]^{2-}$, $[CH_3S-Cu(OH)_2]^{2-}$, and $[CH_3S-CuCl_3]^{3-}$ models to complement the PES experiments of the surface complexes. The calculations have been adjusted using atomic sphere radii to reproduce the experimental valence band photoemission spectra and evaluated relative to the PES results. Having established the utility of the SCF-Xα-SW method in describing the d^{10} Cu(I) bonding of the surface systems, these calculations have been extended to the reduced blue copper active site, shown in Figure 1. The electronic structure description of the blue copper site has been analyzed relative to the normal Cu(I)−L bonding description developed from the surface studies. In addition, to define the electronic structure changes that occur upon oxidation, SCF-Xα-SW calculations have also been performed for a parallel Cu(II) C_s cluster, using bond lengths from the most recent X-ray crystal structure of oxidized plastocyanin.[1]

The detailed description of the reduced blue copper active sites provides the opportunity to evaluate the electronic structure origins of the reduction potentials and geometry changes that occur upon oxidation observed for these proteins. The electronic structure contributions to the high reduction potentials have been addressed by systematically building a blue copper active site model from a constrained CuN_4 cluster.[49] As with the blue copper site, the CuN_4 cluster undergoes only a limited geometry change upon oxidation relative to the appreciable distortions associated with the oxidation of normal Cu(I) complexes,

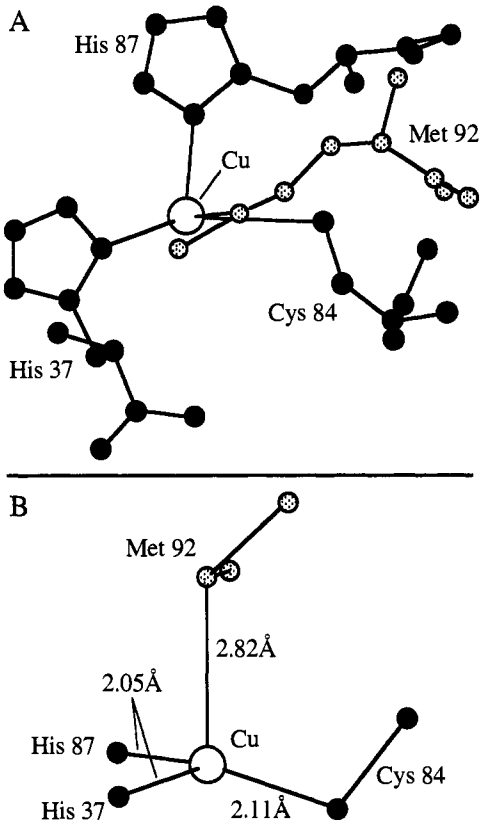

Figure 1. Structure of the reduced blue copper active site of poplar plastocyanin showing (A) the amino acid residues bound to the Cu center and (B) the approximate elongated C_{3v} site symmetry of the site including the Cu(I) bond lengths used for the calculation of the rBC model.

enabling us to focus on the electronic contributions to the reduction potential. Individual Cu−ligand bonding contributions to ionization potentials have been evaluated by substituting the ligands of the CuN_4 model with methyl thioether, methanethiolate, and imidazole. The small geometry changes that occur upon oxidation of the blue copper site result in a low Franck−Condon barrier and rapid rates of electron transfer.[50,51] The electronic structure origins of the limited geometry changes have been analyzed by evaluating the linear coupling terms that are associated with the distortions of a blue copper site unconstrained by the protein environment. In this manner it has been possible to address whether or not a constrained reduced Cu(I) geometry is imposed on the oxidized blue copper site by an entatic or rack conformational state of the protein.

II. Experimental Section

A. Sample Preparation. The CuCl(111) surface was prepared by cutting a 1 mm plate from a single crystal of CuCl. The orientation was checked to within ±1° by Laue back scattering. This surface was polished with alumina grit to 0.1 μm until no visible pits were apparent and chemically etched with a mixture of concentrated HCl and anhydrous ethanol followed by an acetone rinse. Ultrahigh-vacuum (UHV) *in situ* surface cleaning was achieved by Ar^+ sputtering and annealing. To prevent preferential sputtering of chlorine, which occurs at Ar^+ energies >1.1 keV, ion energies were maintained between 900

(38) Yeh, J. J.; Lindau, I. *At. Data Nucl. Data Tables* **1985**, *32*, 1.
(39) Solomon, E. I. *Comm. Inorg. Chem.* **1984**, *3*, 225−320.
(40) Didziulis, S. V.; Cohen, S. L.; Gewirth, A. A.; Solomon, E. I. *J. Am. Chem. Soc.* **1988**, *110*, 250−68.
(41) Thuler, M. R.; Benbow, R. L.; Hurych, Z. *Phys. Rev. B* **1982**, *26*, 669.
(42) Ishii, T.; Taniguchi, M.; Kakizaki, A.; Naito, K.; Sugawara, H.; Nagakura, I. *Phys. Rev. B* **1986**, *33*, 5664.
(43) Lin, J.; Jones, P.; Guckert, J.; Solomon, E. I. *J. Am. Chem. Soc.* **1991**, *113*, 8312−26.
(44) Brundle, C. R.; Bagus, P. S.; Menzel, D.; Hermann, K. *Phys. Rev. B* **1981**, *24*, 7041.
(45) Bagus, P. S.; Seel, M. *Phys. Rev. B* **1981**, *23*, 2065.
(46) Plummer, E. W.; Chen, C. T.; Ford, W. K.; Eberhardt, W.; Messmer, R. P.; Freund, H. J. *Surf. Sci.* **1985**, *158*, 58.
(47) Norton, P. R.; Tapping, R. L.; Goodale, J. W. *Surf. Sci.* **1978**, *72*, 33.
(48) Umbach, E. *Surf. Sci.* **1982**, *117*, 482.
(49) Knapp, S.; Keenan, T. P.; Xiaohua, Z.; Fikar, R.; Potenza, J. A.; Schugar, H. J. *J. Am. Chem. Soc.* **1990**, *112*, 3452−64. The measured value of 110 mV *vs* a standard calomel electrode (SCE) in CH_3CN was adjusted by 250 mV to account for the difference in the SCE in aqueous solution relative to the NHE. This correction is approximate since the properties of the SCE differ in aqueous *vs* nonaqueous solutions.
(50) Sykes, A. G. *Adv. Inorg. Chem.* **1991**, *36*, 377−408.
(51) Sykes, A. G. *Struct. Bonding* **1991**, *75*, 177−224.

and 1000 eV during sputter cycles. Annealing the surface at 350 K for time periods equal to the sputter times restructured the surface and compensated for any disproportionate loss of chlorine.

The $Cu_2O(111)$ surface was prepared similarly by cutting a 1-mm plate from a single crystal of Cu_2O and the orientation was verified to within $\pm 1°$ by Laue back scattering. The surface was polished with alumina grit to 0.1 μm and chemically etched with nitric acid (pH = 1−2). UHV surface cleaning was achieved by Ar^+ sputtering at ion energies of 250−300 eV. At ion energies greater than 300 eV, preferential loss of oxide ions is observed. The sample was maintained at 720 K during sputter cycles and annealed at the same temperature after each sputter process to allow for restructuring of the surface. Low-energy electron diffraction (LEED) has been previously used to show that the sputter conditions used for both the CuCl and Cu_2O single crystals produce clean CuCl(111) and $Cu_2O(111)$ surfaces with no evidence of reconstruction for either surface.

B. PES. Photoemission experiments employing synchrotron radiation were performed on SPEAR beam line III-1 at the Stanford Synchrotron Radiation Laboratory (SSRL) using a grasshopper monochromator. Variable entrance and exit slits on the monochromator allowed a constant energy resolution of 0.3 eV at most photon energies employed. A Perkin-Elmer Φ UHV experimental chamber was used equipped with a double-pass cylindrical mirror analyzer (CMA), a low-energy electron flood gun, and an ion sputter gun. The base pressure of the system was maintained at $\sim 2 \times 10^{-10}$ Torr. The CMA accepts a 6° cone of electrons with a half angle of 42.5° off the CMA axis. For UPS valence band studies narrow analyzer slits and a pass energy of 15 eV allowed for a constant instrument resolution of 0.3 eV, whereas wider analyzer slits and higher pass energies were required for sufficient signal-to-noise ratios in core level PES experiments. The incident synchrotron radiation was fixed at 75° with respect to the central axis of the CMA and impinged on the samples at small grazing angles relative to the crystal surfaces (i.e. electron detection was nearly normal to the sample surface).

Constant Initial State (CIS) spectra were obtained at the Cu 3p → 4s edges. The photoelectron kinetic energy and the photon energy were simultaneously scanned through the absorption edge maintaining a constant initial state, or "binding energy", throughout the experiment. The constant initial state used corresponded to the observed binding energy of the Cu 3d valence satellite maximum in the photoemission spectrum.

For PES adsorption experiments, gases were maintained in a separate UHV manifold and introduced into the main chamber by a variable inlet leak valve. Imidazole was collected in the gas manifold by sublimation of imidazole crystals at ~40 °C. Dimethyl sulfide gas was obtained by collecting the vapor of liquid $(CH_3)_2S$. Research purity grade methanethiol gas was purchased from Matheson Gases. To ensure the highest purity of the gases the UHV gas manifold was thoroughly evacuated and baked prior to the introduction of any new species. During gas exposures, pressures in the main chamber were kept below 5×10^{-7} Torr and monitored using a standard ion gauge. Sample temperatures were maintained at 80−90 K during all adsorption experiments using a LN2 trap on the sample manipulator. At low temperatures sample charging of the p-type Cu_2O semiconductor was compensated with a low-energy electron flood gun operated at ~1.5 V; 2.0 A. All PE spectra were signal averaged until a satisfactory signal-to-noise level was reached and normalized to the incident photon flux which was monitored by collecting the total electron yield from a high-transmission nickel mesh freshly coated with Au in UHV. Ionization energies are referenced to the vacuum level since the conductivity of Cu_2O is poor at low temperatures and the resulting surface charging and band bending complicates the determination of the Fermi level.

C. SCF-Xα-SW Calculations. The 1982 QCPE release of the SCF-Xα-SW program[52−57] was used for electronic structure calculations.

Scheme 1. N_2 2p Contributions to the Lowest Energy Molecular Orbitals of Imidazole

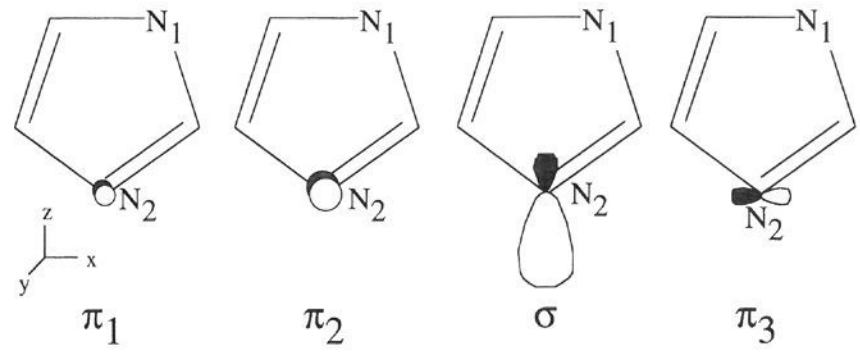

The code was implemented using a MIPS Fortran compiler on a Digital 3100 computer system. To achieve reasonable computation times, the C_s(met) approximation to the plastocyanin site[24,27,58] was employed for all calculations of the blue copper site. In this approximation, the plastocyanin active site is modeled by $Cu[S(CH_3)_2(SCH_3)(N_2C_3H_4)_2]$ where dimethyl sulfide replaces Met92, methanethiolate replaces Cys84, and imidazoles replace the His37 and His87 residues of the protein. In addition, the position and orientation of the imidazoles have been altered slightly to achieve C_s symmetry about the Cu, with a mirror plane defined by the S(Cys), Cu, and S(Met) atoms bisecting the His residues. We have previously shown that the C_s approximation is in good general agreement with a calculation of the blue copper site in the actual C_1 symmetry of the protein,[24] while greatly reducing computational time.

Atomic exchange parameters, α, were taken from Schwarz[59] and the valence-electron-weighted average of the atomic α values was used for the inter- and outersphere α values. A Watson sphere with a radius equal to that of the outersphere and a charge equal to but opposite in sign to the molecule was used in all calculations for ground-state orbital descriptions of charged species. Calculations were accepted as converged when the largest deviation of the atomic potentials between successive SCF iterations was $<10^{-4}$ Ry. The atomic sphere radii [Cu(I) = 2.95 bohr; N(imidazole) = 1.90 bohr; S(thioether) = 2.30 bohr; S(thiolate) = 2.50 bohr] used for the surface and protein models were adjusted to match calculated transiton-state energies to valence photoemission spectra of the small molecules bound to the CuCl(111) and $Cu_2O(111)$ surfaces. The same adjusted sphere radii for the reduced blue copper active site model (rBC) were used in the calculation of the oxidized site (oBC). Complete tables listing all atomic sphere radii and Cartesian coordinates for all calculations performed in this study are provided as supplementary material.

III. PES Results and Spectral Assignments

A. Imidazole on CuCl(111). The highest occupied molecular orbitals of imidazole (Im) are depicted in Scheme 1 and include, from highest to lowest energy, the π_1, π_2, σ, and π_3 orbitals. In the orientation in Scheme 1 the z axis is coincident with the Cu(I)−N_2(imidazole) bond, where N_2 refers to the unprotonated nitrogen of the ligand. The π_1 and π_2 molecular orbitals both involve the N_2 $2p_y$ orbital which is oriented perpendicular to the ligand plane; however, the nitrogen coefficient of the π_1 wave function is considerably smaller than that of the π_2 level. The imidazole σ MO involves contributions from the N_2 $2p_z$ orbital which lies in the ligand plane and bisects the carbon atoms coordinated to the nitrogen. The π_3 orbital involves contributions from the N_2 $2p_x$ orbital, perpendicular to N_2 $2p_y$ in the ligand plane.

The valence band photoelectron spectrum ($h\nu$ = 35 eV) of the clean CuCl single crystal in Figure 2A is consistent with

(52) Johnson, K. H. *Adv. Quantum Chem.* **1973**, *7*, 143−85.
(53) Johnson, K. H.; Norman, J. G., Jr.; Connolly, J. W. D. In *Computational Methods for Large Molecules and Localized States in Solids*; Herman, F.; McLean, A. D., Nesbet, R. K., Eds.; Plenum: New York, 1973; pp 161−201.
(54) Rosch, N.; Kemperer, W. G.; Johnson, K. H. *Chem. Phys. Lett.* **1973**, *23*, 149−54.
(55) Rosch, N. In *Electrons in Finite and Infinite Structures*; Phariseu, P., Scheire, L., Eds.; Wiley: New York, 1977.
(56) Slater, J. C. *The Calculation of Molecular Orbitals*; John Wiley & Sons: New York, 1979; pp 104.
(57) Connolly, J. W. D. In *Semiempirical Methods of Electronic Structure Calculations, Part A: Techniques*; Segal, G. A., Ed.; Plenum: New York, 1977.
(58) Gewirth, A. A.; Cohen, S. L.; Schugar, H. J.; Solomon, E. I. *Inorg. Chem.* **1987**, *26*, 1133−6.
(59) Schwarz, K. *Phys. Rev. B* **1972**, *5*, 2466.

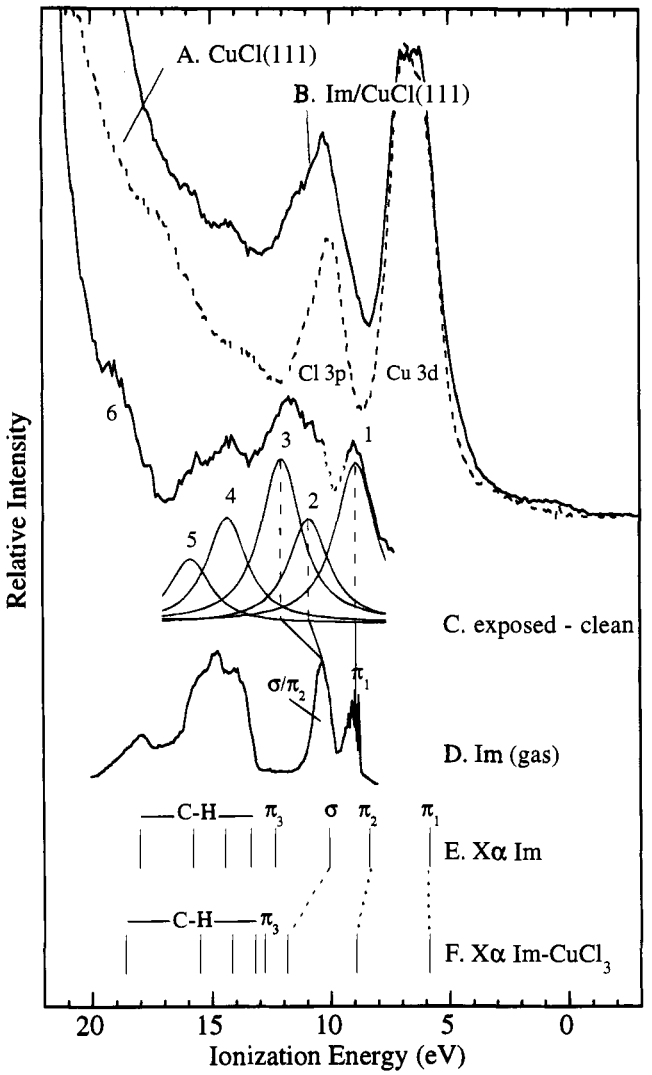

Figure 2. Experimental and calculated valence band spectra of Im−Cu(I) bonding. (A) PES of clean CuCl(111) ($h\nu$ = 35 eV). (B) PES of CuCl(111) exposed to 10 langmuirs of imidazole ($h\nu$ = 35 eV). (C) Difference spectrum of B − A, and Gaussian/Lorentzian resolution of the low-energy region. The difference spectrum was obtained with the Cu 3d band of the exposed surface spectrum scaled to the Cu 3d band of the clean surface spectrum. The dotted region of the spectrum at ~10 eV represents an artifact of the subtraction procedure which is not evident at all photon energies. (D) He I PES of gas-phase imidazole.[61] (E) SCF-Xα-SW Slater transition state energies of the highest occupied molecular orbitals of Im aligned to the deepest energy C−H ionization of the gas-phase imidazole spectrum at 18 eV. (F) SCF-Xα-SW Slater transition state energies of the highest occupied molecular orbitals of $[Im-CuCl_3]^{2-}$ aligned to peak 6 in the difference spectrum of C.

previously reported spectra[40,60] and includes a Cu 3d ionization band centered at 6 eV and a Cl 3p ionization band centered at 10 eV. Exposure of the clean CuCl(111) surface to 10 langmuirs of gas-phase imidazole results in new features in the valence band photoemission spectrum in the energy range of 8−20 eV, Figure 2B. A spectrum of these new featurs, arising from chemisorbed imidazole ionizations, is shown in Figure 2C, obtained by scaling the Cu 3d ionization band of the Im/CuCl(111) spectrum to the Cu 3d ionization band of clean CuCl(111), followed by subtraction of the clean surface spectrum from that of the exposed. The He I gas-phase imidazole photoemission spectrum[61] is also included in Figure 2D and

(60) Didziulis, S. V.; Cohen, S. L.; Butcher, K. D.; Solomon, E. I. *Inorg. Chem.* **1988**, *27*, 2238.

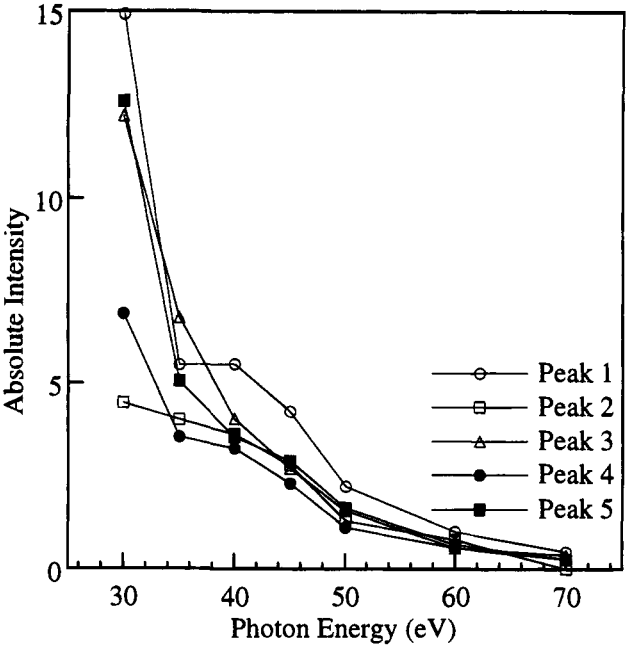

Figure 3. Absolute intensity profiles of the highest energy ionizations of imidazole on CuCl(111) plotted as a function of photon energy. Peaks 1−5 correspond to Figure 2C.

can be considered in two regions. In the lower energy region of the gas-phase spectrum (8−11 eV) are observed the ionizations of the π_1, π_2, and σ orbitals, with the π_2 and σ ionizations nearly degenerate. The deeper energy region, below 13 eV, includes ionizations of the imidazole π_3 MO and the ligand orbitals involved mainly in intra-ring bonding.

The photoemission intensity is dependent on the atomic photoionization cross sections associated with the atomic orbitals contributing to photoionized level. Both the N 2p and C 2p cross sections decay rapidly at photon energies above threshold.[38] Absolute intensities of the Cu(I)-bound imidazole ionizations in Figure 2C are plotted as a function of photon energy ($h\nu$) in Figure 3. The broad band at 13−16 eV in Figure 2C is comprised of several ligand orbital overlapping ionizations; therefore, this region has been treated as two effective peaks (4−5) at ionization energies of 14.5 and 15.5 eV. The intensity profiles of peaks 1−5 in the Cu(I)-bound imidazole spectrum all exhibit a monotonic decay with increasing photon energy, characteristic of nitrogen and carbon 2p cross sections and consistent with assignment of these peaks as imidazole valence ionizations.[62]

Comparison of the surface-bound imidazole spectrum with the gas-phase imidazole spectrum provides insight into specific imidazole valence orbital contributions to the Cu(I)−Im bond. In the lower ionization energy region of the chemisorbed imidazole spectrum (Figure 2C) the energy of the π_1 ionization is not shifted from the gas-phase value in Figure 2D, indicating no significant interaction of this MO in bonding to the surface Cu(I) site. The lack of π_1 interaction is consistent with the very small N_2 coefficient of the π_1 wave function (Scheme 1) which precludes significant overlap with the metal. Relative to the gas-phase imidazole spectrum, a significant intensity shift is observed in the region between 10 and 13 eV of the chemisorbed imidazole spectrum, which is attributed primarily to a 1.2-eV stabilization of the σ molecular orbital (peak 3, Figure 2C) upon

(61) Cradock, S.; Findlay, R. H.; Palmer, M. H. *Tetrahedron* **1973**, *29*, 2173−81.

(62) The apparent maximum at ~45 eV in the intensity profile of peak 1 is due to the overlap of this peak with the Cu-3d manifold in the valence band photoemission spectrum.

adsorption to the CuCl(111) surface. At the low adsorbate coverages maintained in this study, imidazole is expected to bind to the surface copper with the plane of the ligand ring perpendicular to the crystal surface. Therefore, the ligand σ orbital will be oriented along the Cu(I)−imidazole bond axis, resulting in strong overlap with Cu(I) d_z2 and $4p_z$ and significant stabilization of the σ MO. Also contributing to the intensity shift in this region is a smaller, 0.5-eV stabilization of the imidazole π_2 level (peak 2, Figure 2C) upon adsorption. The smaller energy shift of π_2 indicates significantly weaker involvement of this MO in Cu(I) bonding relative to the imidazole σ level. The π_2 orbital overlap with Cu(I) is weaker than the σ interaction due to the π orientation of the N_2 $2p_y$ component of the imidazole π_2 orbital with respect to the metal, but it is stronger than π_1 interaction because of the larger N_2 coefficient of the π_2 wave function. The chemisorbed imidazole ionizations at energies greater than 13 eV, associated with ligand ring bonding orbitals, do not appear to be shifted relative to the free ligand spectrum, indicating no participation of these levels in Cu(I) bonding.

Cu(I) 4s contributions to Cu(I)−Im bonding are manifested as a shift in the intensity maximum of the Cu 3d shake-up satellite in the constant initial state (CIS) spectrum. The Cu valence satellite, which appears ~13 eV to deeper binding energy from the main Cu 3d ionization band in the clean CuCl spectrum in Figure 4A, corresponds to a Cu 3d ionization plus a 3d → 4s "shake-up" transition. The shake-up satellite intensity mechanism[41,42,60]

$$Cu\ 3p^6 3d^{10} 4s^0 \xrightarrow{h\nu} 3p^5 3d^{10} 4s^1 \xrightarrow{SCK} 3p^6 3d^8 4s^1$$

involves the excitation of an electron from the filled Cu 3p level to the unoccupied Cu 4s orbital, followed by a rapid Super Coster−Kronig (SCK) Auger decay, resulting in the $3p^6 3d^8 4s^1$ final state configuration; therefore, the intensity of the satellite is resonance enhanced at photon energies corresponding to the Cu 3p → 4s adsorption edge. In a constant initial state (CIS) resonance PES experiment, photoemission intensity is monitored at a constant binding energy (*i.e.* initial state) by simultaneously sweeping the photon energy and the kinetic energy of detection. In the CIS spectrum of the clean CuCl Cu 3d satellite, shown in Figure 4C, the resonance intensity maximum occurs at ~76 eV. Imidazole bonding interaction with the Cu 4s orbital would destabilize the 4s orbital energy and increase the 3p → 4s transition energy, shifting the satellite resonance intensity maximum. No such shift in the intensity maximum is observed in the satellite CIS spectrum of the Im/CuCl(111) surface system in Figure 4D, indicating that the Cu 4s orbital does not participate significantly in Cu(I)−Im bonding.

It has been previously determined that the appearance of shake-up satellite structure in the C 1s core level spectrum of CO bound to transition metals is an indication of metal-to-ligand π back bonding.[43−48] The core satellite derives from a screening of the direct photoionization ligand core hole by charge donation from the filled metal d levels into the unoccupied ligand π^* levels. Therefore, two core ionizations are observed, corresponding to the unscreened and screened final states, and the intensity of the screened final state, *i.e.*, the satellite, is a measure of the back bonding present in the ligand−metal complex. The N 2s photoemission spectrum of Im/CuCl(111) in Figure 5A consists of two peaks associated with the two chemically distinct nitrogens of the surface-bound imidazole. At 37.1 eV, the Cu(I)-coordinated N_2 2s ionization is chemically shifted by 1.4 eV from the 2s ionization of the protonated imidazole nitrogen. The absence of any deeper binding energy satellite structure in the N 2s spectrum indicates little contribution of Cu 3d to imidazole π^* back donation in the Im/CuCl(111) system.

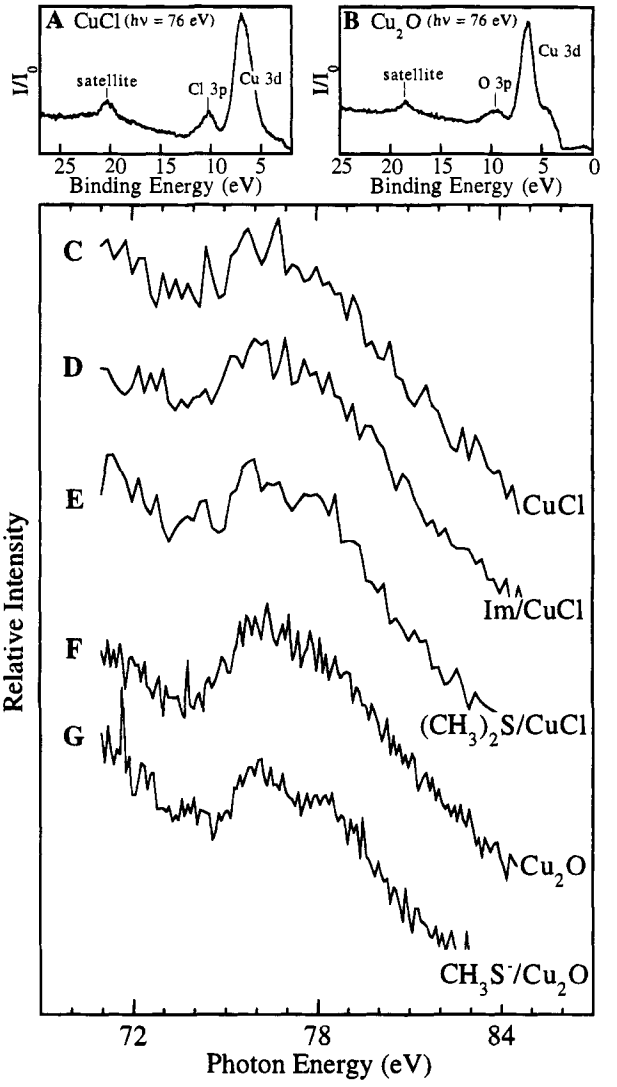

Figure 4. Valence band satellites of (A) CuCl and (B) Cu_2O ($h\nu$ = 76 eV). Constant initial state (CIS) resonance photoemission spectra, collected at an initial state corresponding to the valence satellites in A and B, of (C) clean CuCl(111), (D) 10 langmuirs of Im/CuCl(111), (E) 10 langmuirs of $(CH_3)_2S$/CuCl(111), (F) clean Cu_2O(111), and (G) 10 langmuirs of CH_3S^-/Cu_2O(111).

B. Dimethyl Sulfide on CuCl(111). The three highest occupied molecular orbitals of dimethyl sulfide, pictured in Scheme 2, all consist primarily of S 3p contributions. In Scheme 2 the *z*-axis is coincident with the molecular C_2 axis, and the *x*-axis lies in the molecular mirror plane bisecting the two methyl carbon atoms. The highest occupied thioether valence level (b_1) corresponds to the nonbonding ligand lone pair and consists predominantly of a contribution from the S $3p_y$ orbital, perpendicular to the CSC ligand plane. The a_1 MO involves primarily a contribution from the S $3p_z$ orbital; and to deeper energy, the b_2 MO consists chiefly of S $3p_x$ orbital character in the CSC plane.

The valence band photoemission spectrum of a clean CuCl(111) single crystal ($h\nu$ = 40 eV) is presented in Figure 6A. Exposure of the clean CuCl(111) surface to 10 langmuirs of gas-phase dimethyl sulfide results in the appearance of new features in the valence band spectrum in Figure 6B. These features are associated with ionization of the chemisorbed thioether and are elucidated in Figure 6C by the subtraction of the clean CuCl spectrum from the $(CH_3)_2S$/CuCl(111) spectrum

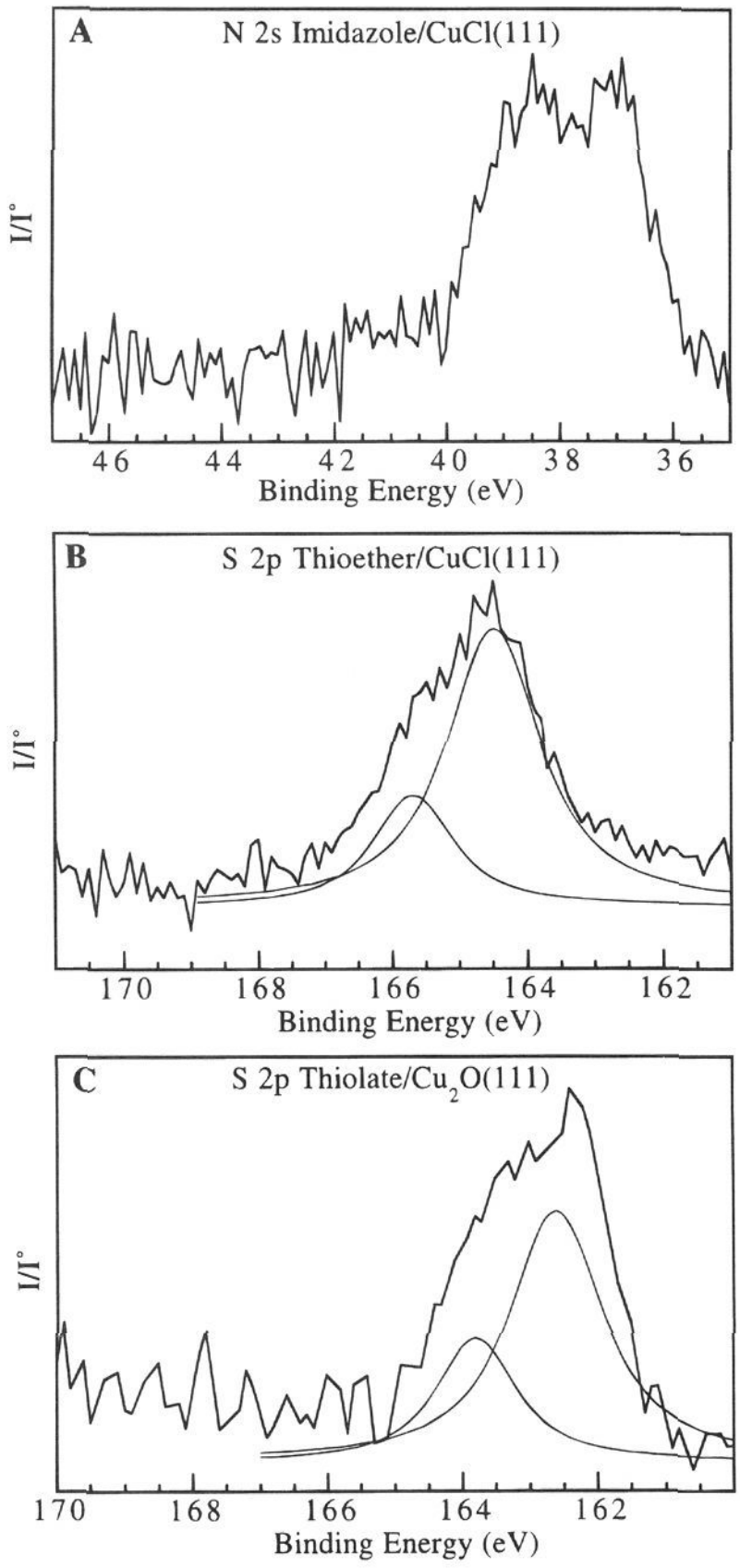

Figure 5. Core XPS of ligands bound to Cu(I) surface sites. (A) N 2s spectrum of 10 langmuirs of Im/CuCl(111) ($h\nu = 90$ eV). (B) S 2p spectrum of 10 langmuirs of $(CH_3)_2S$/CuCl(111) ($h\nu = 210$ eV and (C) S 2p spectrum of 10 langmuirs of $CH_3S^-/Cu_2O(111)$ ($h\nu = 210$ eV), showing the Gaussian/Lorentzian resolution of the $2p_{3/2}$ and $2p_{1/2}$ ionizations.

as described above for the Im/CuCl(111) system. To deeper binding energy in Figure 6C are the S 3s ionization at 19 eV (peak 5) and the C−H ionizations centered at 16.5 eV (peak 4). A broad feature appears centered at ~12 eV that can be fit to a minimum of two Gaussian/Lorentzian peaks while maintaining reasonable full-width-at-half-maximum (fhwm) values and are labeled as peaks 2 and 3 at binding energies of 11.2 and 12.5 eV. The lowest energy ionization, peak 1, occurs at 9.8 eV. Comparison of Figure 6C with the gas-phase $(CH_3)_2S$ He I photoemission spectrum[63] in Figure 6D allows the assignment of peaks 1−3 as the thioether b_1, a_1, and b_2 ionizations, respectively.

The absolute intensities of peaks 1−3 in the chemisorbed thioether photoemission spectrum are plotted as a function of photon energy in Figure 7. The atomic photoionization cross sections associated with photoemission from atomic orbitals that have at least one radial node, *e.g.* S 3p, exhibit a Cooper minimum[64,65] where the regions of positive and negative overlap between the initial state atomic radial wave function and the plane-wave final state are equal and the intensity approaches zero. In the intensity profiles of peaks 1−3 the S 3p Cooper minimum expected at ~37 eV is notably absent, indicating the presence of C 2s and Cu 3d mixing into these ligand valence levels. The C 2s wave function does not have a radial node; therefore, the carbon character from the two methyl groups in the S 3p peaks masks the Cooper minimum.[66] The atomic photoionization cross section associated with orbitals with l quantum numbers ≥ 1 exhibits a delayed maximum at photon energies beyond threshold energies. The delayed maximum arises as a result of the centrifugal barrier that exists at lower photon energies which prevents penetration of the plane wave final state.[67,68] For copper 3d photoionization, the delayed maximum occurs at $h\nu \approx 45$ eV; therefore, Cu 3d mixing in peaks 1−3 will also mask the S 3p Cooper minimum which occurs in the same region. The relative amounts of Cu 3d mixing in the thioether valence orbitals can be evaluated by plotting the relative intensities of peaks 1−3 vs photon energy, shown in the inset of Figure 7. The rise in the intensity of peak 1 relative to peaks 2 and 3 through photon energies of 25−45 eV indicates a greater delayed maximum contribution, and therefore a greater amount of Cu 3d character in the b_1 level.

Scheme 2. S 3p Contributions to the Lowest Energy Molecular Orbitals of Thioether

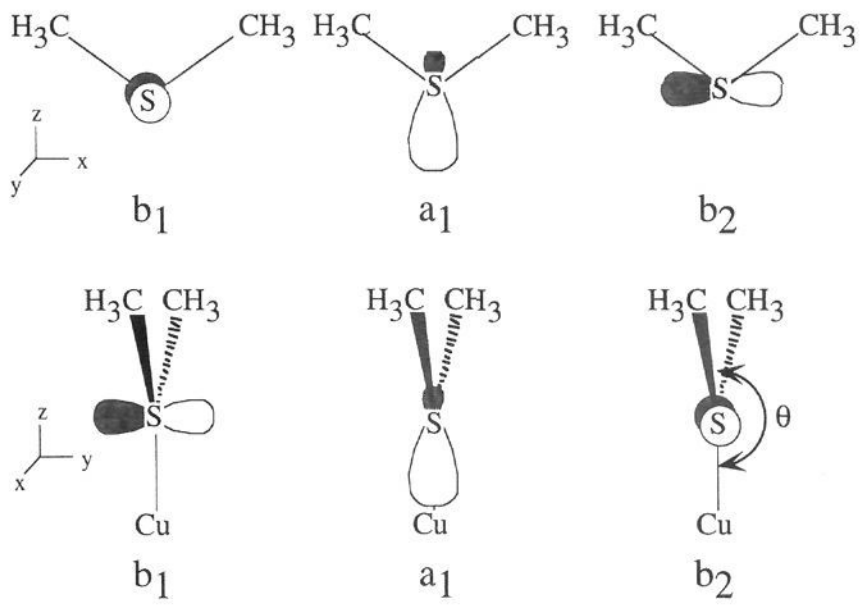

Comparison of the Cu(I)-bound (Figure 6C) and gas-phase (Figure 6D) thioether photoemission spectra yields insight into the individual thioether valence orbital contributions to Cu(I)−thioether bonding at the CuCl(111) surface. The most striking difference in the two spectra is the 1.2-eV stabilization of the thioether b_1 ionization upon adsorption to the surface. The thioether a_1 orbital is stabilized to a much lesser extent, 0.4 eV, upon chemisorption; and the energy of the ligand b_2 ionization is unchanged. At a Cu(I)−thioether bonding geometry of $\theta = 180°$, where the angle θ is defined by the Cu(I)−S bond and the C−S−C ligand plane (Scheme 2), the thioether b_1 and b_2 orbitals would be oriented purely π with respect to the surface Cu(I) site, while the ligand a_1 orbital would be oriented directly along the Cu(I)−S bond axis and would be

(63) Frost, D. C.; Herring, F. G.; Katrib, A.; McDowell, C. A.; McLean, R. A. N. *J. Phys. Chem.* **1972**, *76*, 1030−4.

(64) Fano, U.; Copper, J. W. *Rev. Mod. Phys.* **1968**, *40*, 441.

(65) Cooper, J. W. *Phys. Rev.* **1962**, *128*, 681.

(66) Glass, R. S.; Broeker, J. L.; Jatcko, M. E. *Tetrahedron* **1989**, *45*, 1263−72.

(67) Manson, S. T.; Cooper, J. W. *Phys. Rev.* **1968**, *165*, 126.

(68) Eastman, D. E.; Kuznietz, M. *J. Appl. Phys.* **1971**, *42*, 1396.

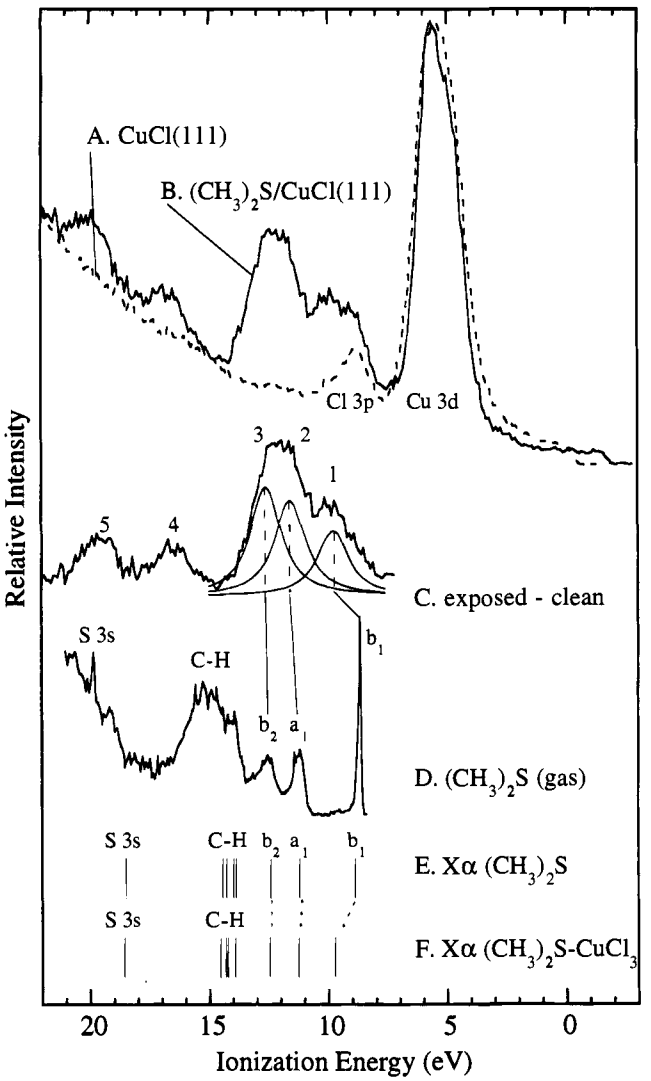

Figure 6. Experimental and calculated valence band spectra of $(CH_3)_2S$–Cu(I) bonding. (A) PES of clean CuCl(111) ($h\nu$ = 40 eV). (B) PES of CuCl(111) exposed to 10 langmuirs of gaseous dimethyl thioether ($h\nu$ = 40 eV). (C) Difference spectrum of B − A and Gaussian/Lorentzian resolution of the low-energy region. The difference spectrum was obtained with the Cu 3d ionization band of the exposed surface spectrum scaled to the Cu 3d band of the clean surface spectrum. (D) He I PES of gas-phase dimethyl thioether.[63] (E) SCF-Xα-SW Slater transition state energies of the highest occupied molecular orbitals of $(CH_3)_2S$ aligned to the S 3s ionization of the gas-phase thioether spectrum. (F) SCF-Xα-SW Slater transition state energies of the highest occupied molecular orbitals of $[(CH_3)_2S-CuCl_3]^{2-}$, at θ = 110°, aligned to the S 3s ionization of the difference spectrum of C.

expected to dominate the Cu(I)–thioethers bonding interactions. At smaller angles θ, the thioether a_1 MO is rotated off the Cu(I)–S bond axis, decreasing overlap with the metal, while the thioether b_1 orbital is rotated toward the Cu(I)–S bond, gaining σ character and increasing overlap with the metal. In the surface-bound photoemission spectrum of Figure 6C, the b_1 ionization exhibits the greatest amount of stabilization upon bonding to Cu(I) and exhibits the greatest amount of Cu 3d character in the relative peak intensity profiles in Figure 7 (inset), indicating that the thioether binds to the CuCl(111) surface at an angle θ significantly less than 180°. Changes in the bonding angle have no effect on the metal–ligand overlap involving the thioether b_2 orbital since the S $3p_x$ component of this MO is oriented π with respect to Cu(I) at any value of θ. Furthermore, the small sulfur coefficient in thioether b_2 MO precludes significant overlap with the Cu(I) ion, and no stabilization of this level upon surface adsorption is observed in Figure 6C relative to Figure 6D.

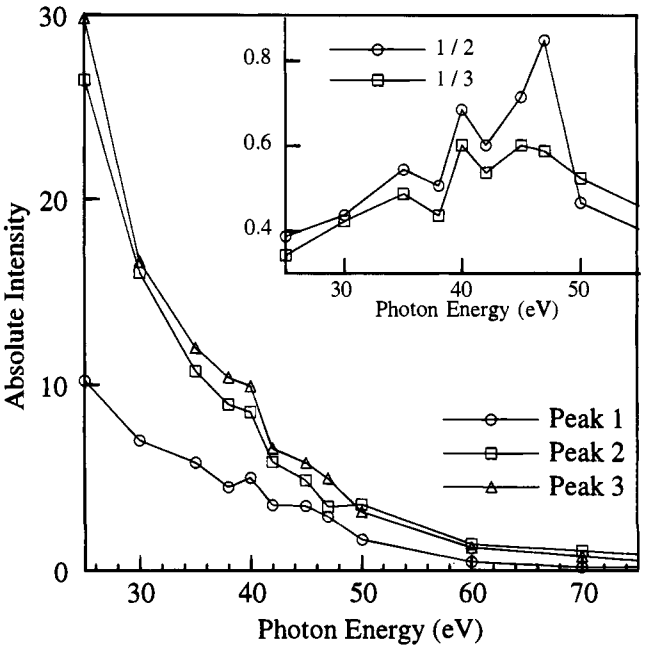

Figure 7. Absolute intensity profiles of the three highest energy ionizations of $(CH_3)_2S$–CuCl(111) plotted as a function of photon energy. Peaks 1–3 correspond to Figure 6C. Inset: Intensity ratios of peak 1 relative to peaks 2 and 3 as a function of photon energy.

CIS resonance photoemission of thioether on CuCl(111) is presented in Figure 4E. Similar to the CIS results presented for imidazole on CuCl(111), no shift is seen in the resonance intensity maximum of the Cu 3d valence satellite upon adsorption of thioether on the CuCl(111) surface, demonstrating very little Cu 4s participation in Cu(I)–thioether bonding.

The S 2p core level photoemission spectrum of $(CH_3)_2S$/CuCl(111) is presented in Figure 5. The surface-bound S $2p_{3/2}$ and $2p_{1/2}$ ionizations at 164.5 and 165.6 eV, respectively, represent a chemical shift of ~1.5 eV to higher binding energy relative to typical gas-phase RSR S $2p_{3/2}$ values of ~163 eV,[69] arising from an increased effective nuclear charge on the sulfur center as electron density is donated to the positively charged Cu(I) surface site. No satellite structure is observed in the S 2p core spectrum, indicating no significant Cu 3d → S 3d back bonding contribution to the Cu(I)–thioether bond.

C. Methanethiolate on Cu_2O(111). The highest occupied molecular orbitals of CH_3SH are depicted in Scheme 3A and include a non-bonding a″ lone pair and two bonding a′ levels associated with the S–C and S–H bonds. All three of these MO's consist predominantly of S 3p contributions. Importantly, in the He I gas-phase PES of methanethiol, the ionizations of the three highest occupied orbitals are well separated in energy, with the a″ level at 9.4 eV, the a′(S–C) level at 12.0 eV, and the a′(S–H) level at 13.9 eV.[63] Removal of the acidic proton to create a CH_3S^- thiolate species should result in a dramatically different orbital splitting pattern, with two degenerate nonbonding lone pair orbitals and one σ S–C orbital (Scheme 3B).

The Cu_2O(111) surface was used in this study to facilitate the deprotonation of CH_3SH. The S $2p_{3/2}$ and S $2p_{1/2}$ core level ionizations in Figure 5C are observed at 162.4 and 163.5 eV for the Cu(I)-bound ligand. Protonated thiol bound to copper should exhibit S 2p binding energies very close to those of Cu(I)-bound thioether;[69,70] however, the ionization energies in

(69) Best, S. A.; Brant, P.; Feltham, R. D.; Rauchfuss, T. B.; Roundhill, D. M.; Walton, R. A. *Inorg. Chem.* **1977**, *16*, 1976–9.

Scheme 3. S 3p Contributions to the Lowest Energy Molecular Orbitals of

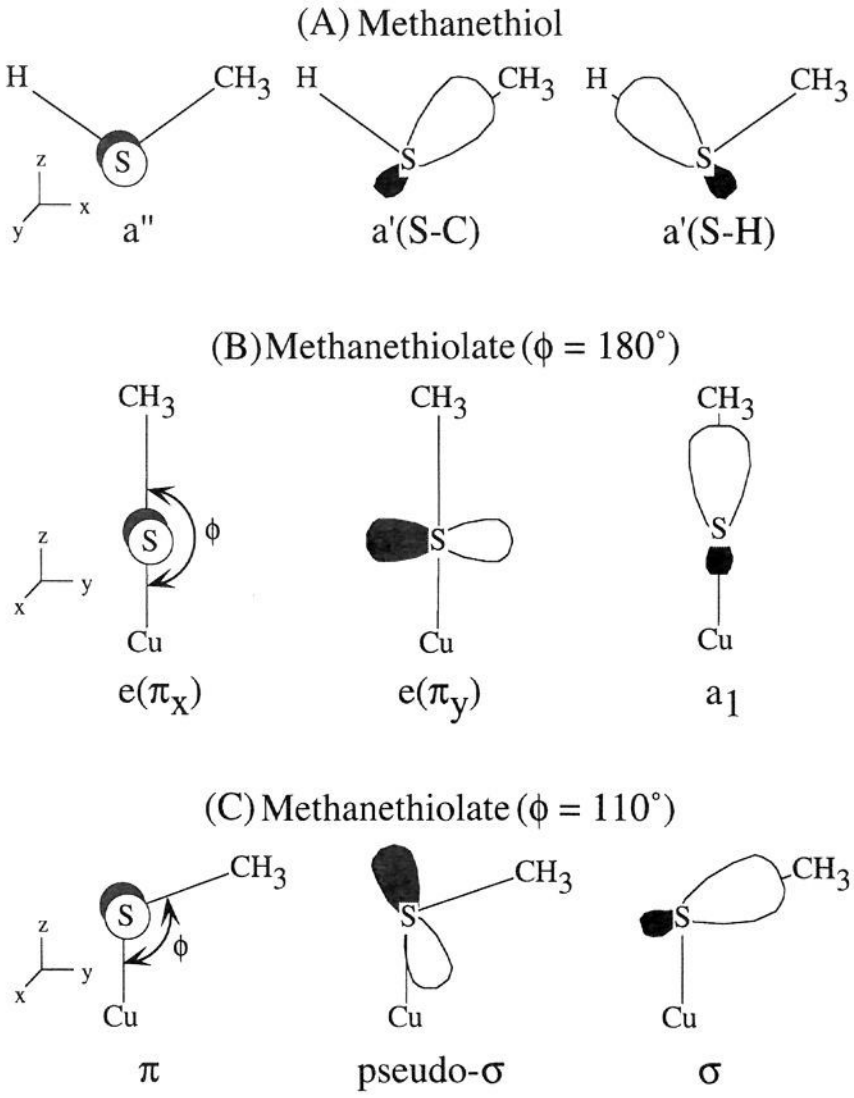

Figure 5C are chemically shifted by 2.1 eV to lower binding energy relative to the Cu(I)−thioether system and at least 0.5 eV lower than typical free ligand thiol S 2p values ($Sp_{3/2}$ = 162.9−163.3 eV),[70] consistent with the deprotonation of the thiol on the $Cu_2O(111)$ surface to form a Cu(I)−SCH_3 species.

The valence band photoemission spectrum ($h\nu$ = 40 eV) of the clean $Cu_2O(111)$ single crystal is shown in Figure 8A and is comprised of a Cu 3d ionization band at 5−8 eV and an O 2p ionization band at 9−12 eV, consistent with previously reported results.[37] Exposure of the $Cu_2O(111)$ surface to 10 langmuirs of CH_3SH results in new features in the $Cu_2O(111)$ valence band photoemission spectrum in the energy range 11−20 eV, Figure 8B. These new features are associated with photoemission from the chemisorbed thiolate and are presented in the difference spectrum in Figure 8C, obtained as described above. The broad band labeled peak 4 in Figure 8C centered at ~20.5 eV is comprised of ionizations from the S 3s orbital (~21 eV) and the C−H bonding orbitals (19−20 eV). The two bands at lower ionization energy are associated with photoemission from the three thiolate S 3p orbitals. The band centered at 13 eV can be fit to a minimum of two peaks while maintaining reasonable fwhm values, labeled as peaks 1 and 2 at 12.7 and 13.5 eV, respectively. These lowest energy ionizations arise from photoemission of the two thiolate S 3p lone pairs. As described above, the near degeneracy of the lone pair ionizations provides additional evidence of deprotonation of the thiol upon chemisorption to the $Cu_2O(111)$ surface; however, the fact that these ionizations are split by 0.8 eV indicates that the thiolate bonds to the surface at a ∠Cu−S−C angle (ϕ) less than 180°, with one of the lone pairs rotated toward the Cu(I)−S bond axis. Peak 3 occurs at 17 eV and is assigned as the deeper energy thiolate σ orbital involved in S−C bonding.

(70) Srinivasan, V.; Stiefel, E. I.; Walton, R. A. *J. Am. Chem. Soc.* **1979**, *101*, 2611−4.

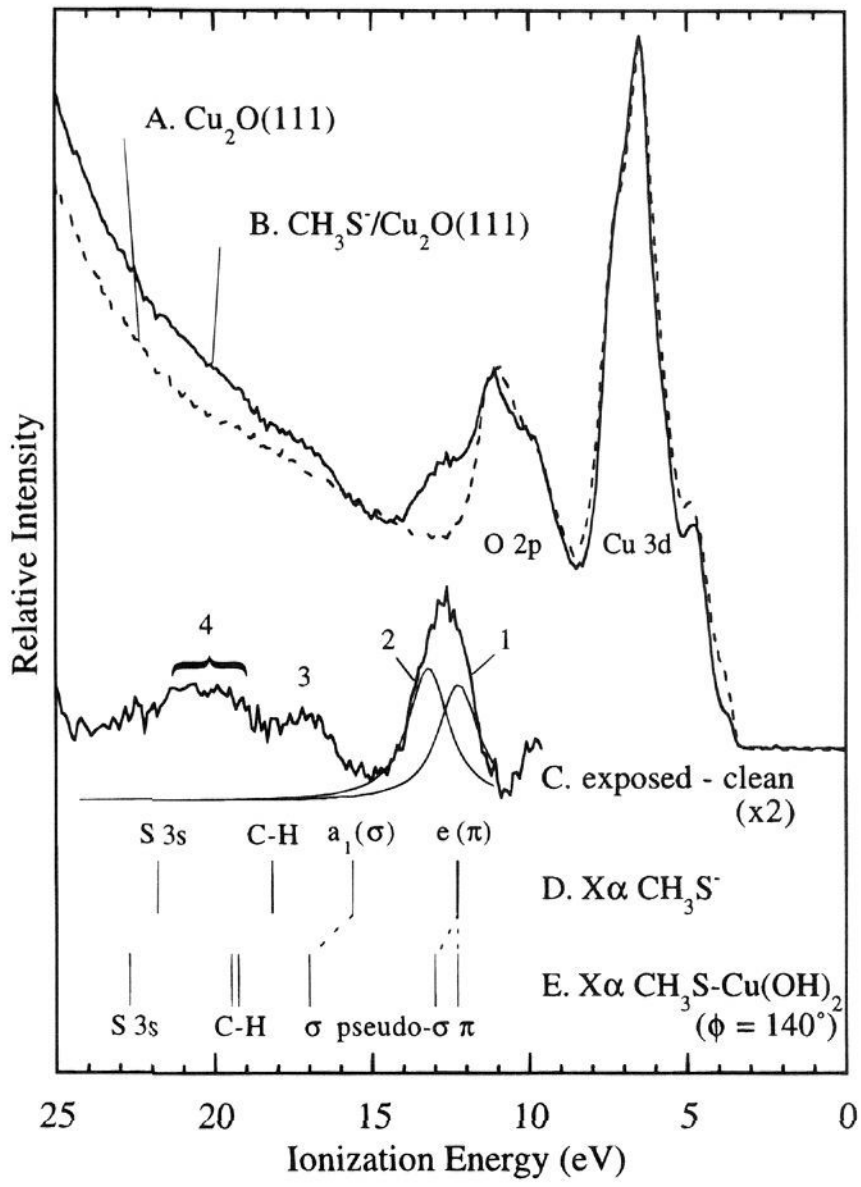

Figure 8. Experimental and calculated valence band spectra of CH_3S−Cu(I) bonding. (A) PES of clean $Cu_2O(111)$ ($h\nu$ = 40 eV). (B) PES of $Cu_2O(111)$ exposed to 10 langmuirs of methanethiol ($h\nu$ = 40 eV). (C) Difference spectrum of B − A, and Gaussian/Lorentzian resolution of the low-energy region. The difference spectrum was obtained by scaling the Cu 3d ionization band of the exposed surface spectrum to the Cu 3d band of the clean surface spectrum. (D) SCF-Xα-SW Slater transition state energies of the highest occupied molecular orbitals of CH_3S^- aligned to the calculated π ionization of E. (E) SCF-Xα-SW Slater transition state energies of the highest occupied molecular orbitals of $[CH_3S-Cu(OH)_2]^{2-}$, at ϕ = 110°, aligned to the lowest energy ionization of the difference spectrum of C.

As no PES has been reported on the gas-phase CH_3S^- ion, the energy stabilization of the thiolate orbitals from Cu(I) interactions cannot be experimentally assessed; however, relative bonding contributions of the thiolate valence orbitals have been evaluated using variable-energy PES. Absolute intensities of peaks 1−3 of the surface-bound thiolate spectrum in Figure 8 are plotted as a function of photon energy in Figure 9. For all three ionizations a Cooper minimum at ~37 eV is observed in the monotonic intensity decays with increasing photon energy, characteristic of the S 3p cross section and consistent with the assignment of these peaks as ionizations from thiolate-derived orbitals. Relative intensity plots (Figure 9, inset) reveal a strong delayed maximum in the intensities of peaks 1 and 2 relative to peak 3, indicating significantly more Cu 3d character in the thiolate π levels compared to the thiolate σ orbital. The relatively weak σ overlap in the Cu(I)−thiolate system results from the dominant S−C interaction in the thiolate σ MO (Scheme 3B), which shifts electron density from the Cu(I)−S bond. The π orbitals, on the other hand, participate only weakly in S−C bonding, and, therefore, can overlap with the Cu(I) ion to a greater extent.

The Cu 3d valence satellite of $Cu_2O(111)$ in Figure 4B is observed 12 eV to deeper binding energy than the main Cu 3d

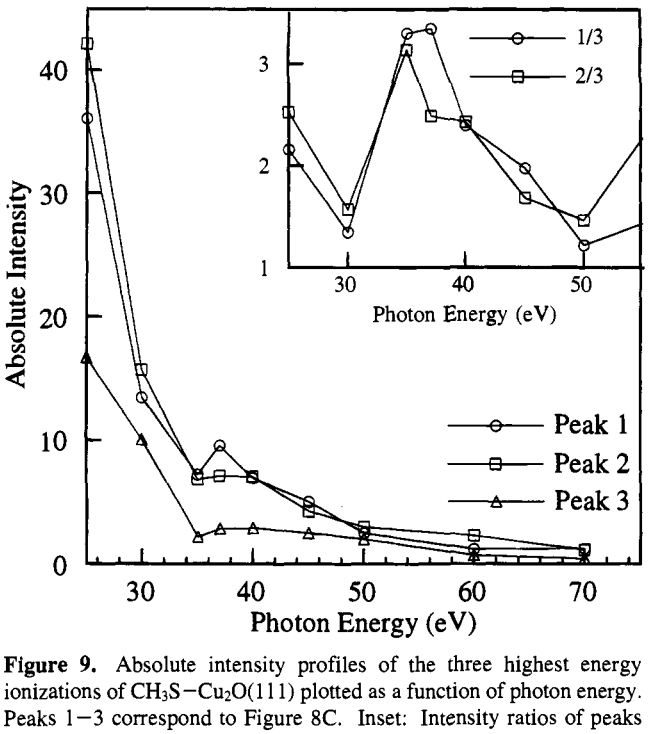

Figure 9. Absolute intensity profiles of the three highest energy ionizations of $CH_3S-Cu_2O(111)$ plotted as a function of photon energy. Peaks 1–3 correspond to Figure 8C. Inset: Intensity ratios of peaks 1 and 2 relative to peak 3 as a function of photon energy.

ionization band. Similar to CuCl, CIS resonance PES of the clean $Cu_2O(111)$ surface in Figure 4F reveals resonance intensity enhancement at photon energies near 76 eV, corresponding to the Cu 3p → 4s absorption edge. Upon chemisorption of thiolate to the $Cu_2O(111)$ surface, no shift is observed in the resonance intensity maximum of the Cu 3d valence satellite, Figure 4G, indicating no change in the Cu 3p → 4s absorption edge and, thus, no significant Cu 4s contribution to Cu(I)–thiolate bonding. Finally, no satellite structure is observed in the S 2p photoemission spectrum in Figure 5C, suggesting little contribution from Cu 3d → S 3d back bonding to the Cu(I)–thiolate bond in the $CH_3S^-/Cu_2O(111)$ system.

IV. Analysis

A. Electronic Structure of Cu(I)–Ligand Bonding. 1. Imidazole. SCF-Xα-SW molecular orbital calculations have been performed on an unbound imidazole molecule and imidazole axially coordinated to a C_{3v} $CuCl_3^{2-}$ cluster to complement the PES experiments on the Im/CuCl(111) system presented in Section III.A. In the calculation of the $[Im-CuCl_3]^{2-}$ cluster, a Cu–N bond length of 2.05 Å was used, and a C_s geometry was assumed in which imidazole binds to Cu(I) with the plane of the ligand ring perpendicular to the CuCl(111) crystal surface. The free imidazole ligand was calculated in the same orientation as the Cu(I)-bound ligand to facilitate comparisons between the two calculations. Complete lists of atomic coordinates and input for the calculations of both species are available as supplementary material.

The SCF-Xα-SW Slater transition state energies of the highest occupied molecular orbitals of unbound imidazole and Cu(I)-bound imidazole, shown in Figure 2, spectra E and F, are qualitatively consistent with the valence band PES results in Figure 2, spectra C and D. In the deeper energy region of the imidazole valence region the calculated ionization energies of the imidazole ring bonding orbitals, which are not involved in Cu(I) bonding, match the unbound and chemisorbed imidazole PES data particularly well. In the lower energy region, the energies of the imidazole σ ionizations also agree well with the experimental spectra; but, the calculated π ionizations are too low in energy relative to the experimental values. Adjusting the atomic sphere radii failed to yield better results. The energetic description of out-of-plane π orbitals of planar molecules is a documented shortcoming of the SCF-Xα-SW method arising from the considerable size of the constant-potential intersphere region in these calculations. Since the imidazole π_1 and π_2 orbitals extend significantly above and below the plane of the ring ito the intersphere region, the SCF-Xα-SW energies of these levels are less reliable than the calculated energies of the σ-type orbitals.

SCF-Xα-SW electron density contour plots of the three highest occupied imidazole valence orbitals (π_1, π_2, and σ) are presented in Figure 10 for the unbound (Figure 10B–D) and surface-bound imidazole (Figure 10F–H) calculations. SCF-Xα-SW molecular orbital charge distributions are presented in Table 1, where His refers to the imidazole ligand, and ground-state energy level diagrams of unbound imidazole and $[Im-CuCl_3]^{2-}$ are presented in Figure 11.[71] From Table 1, the highest energy C–H orbital (level 11a′) exhibits no Cu(I) mixing in the $[Im-CuCl]^{2-}$ cluster; therefore no stabilization of this MO is expected upon bonding to the Cu(I) surface site, and the energies in Figure 11 have been aligned to the corresponding C–H level in the free ligand.

Consistent with the PES results for the free imidazole ligand and imidazole chemisorbed to the CuCl(111) surface, the SCF-Xα-SW results in Table 1 demonstrate that all imidazole contributions to Cu(I) bonding arise from the three highest occupied ligand valence orbitals, π_1, π_2, and σ. The dominant Cu(I)–imidazole interaction is seen in the 12a′ His σ level, which contains 28% Cu character (Table 1). The large amount of Cu(I) mixing in the His σ orbital results in a 2.0-eV stabilization of this level upon bonding to the metal site, Figure 11. The electron density contour plot of the His σ orbital in Figure 10B reveals a significant amount of N_2 $2p_z$ electronic density available for Cu(I) bonding. From Figure 10F, the N $2p_z$ of the His σ MO of $[Im-CuCl_3]^{2-}$ is oriented directly along the Cu(I)–N bond axis resulting in strong overlap with the metal. The 3a″ His π_2 level interacts to a much lesser degree with Cu(I), containing only 5% Cu character in the $[Im-CuCl_3]^{2-}$ cluster (Table 1) and undergoing a 0.7-eV stabilization upon bonding to the Cu(I) surface, Figure 11. The electronic contour plot of the unbound imidazole π_2 MO in Figure 10C reveals that the electron density centered on the bonding N_2 atom is comparable to that in the free imidazole σ orbital, but overlap of π_2 with Cu(I) is limited by the π orientation of this level with respect to the metal, Figure 10G. Finally, the highest energy ligand-derived orbital, the 8a″ His π_1 level, undergoes virtually no interaction with Cu(I) in the $[Im-CuCl_3]^{2-}$ model, containing only 1% metal character (Table 1), and stabilized by only 0.2 eV, Figure 11. Similar to the π_2 orbital, Cu(I) overlap with π_1 is limited by the π orientation of the orbital with respect to the metal. Additionally, the N_2 coefficient of the π_1 MO is much smaller in Figure 10D than that of π_2, further reducing effective overlap with the surface Cu(I) site in Figure 10H.

Any Cu(I) mixing in the π_1, π_2, and σ ligand valence orbitals will shift these ligand levels to deeper energy. It is important to emphasize, however, that the interaction of the filled Cu(I)

(71) The ground state orbital energies in Figure 11, 14, and 17 have been adjusted to compensate for the differences in intersphere volumes between the SCF-Xα-SW calculations of the free ligands and surface complexes. Since the intersphere region is described at a constant potential, disparate contributions from this region have been compensated by shifting each level by the coefficient of the intersphere in the wave function times the value of the constant potential for that cluster.

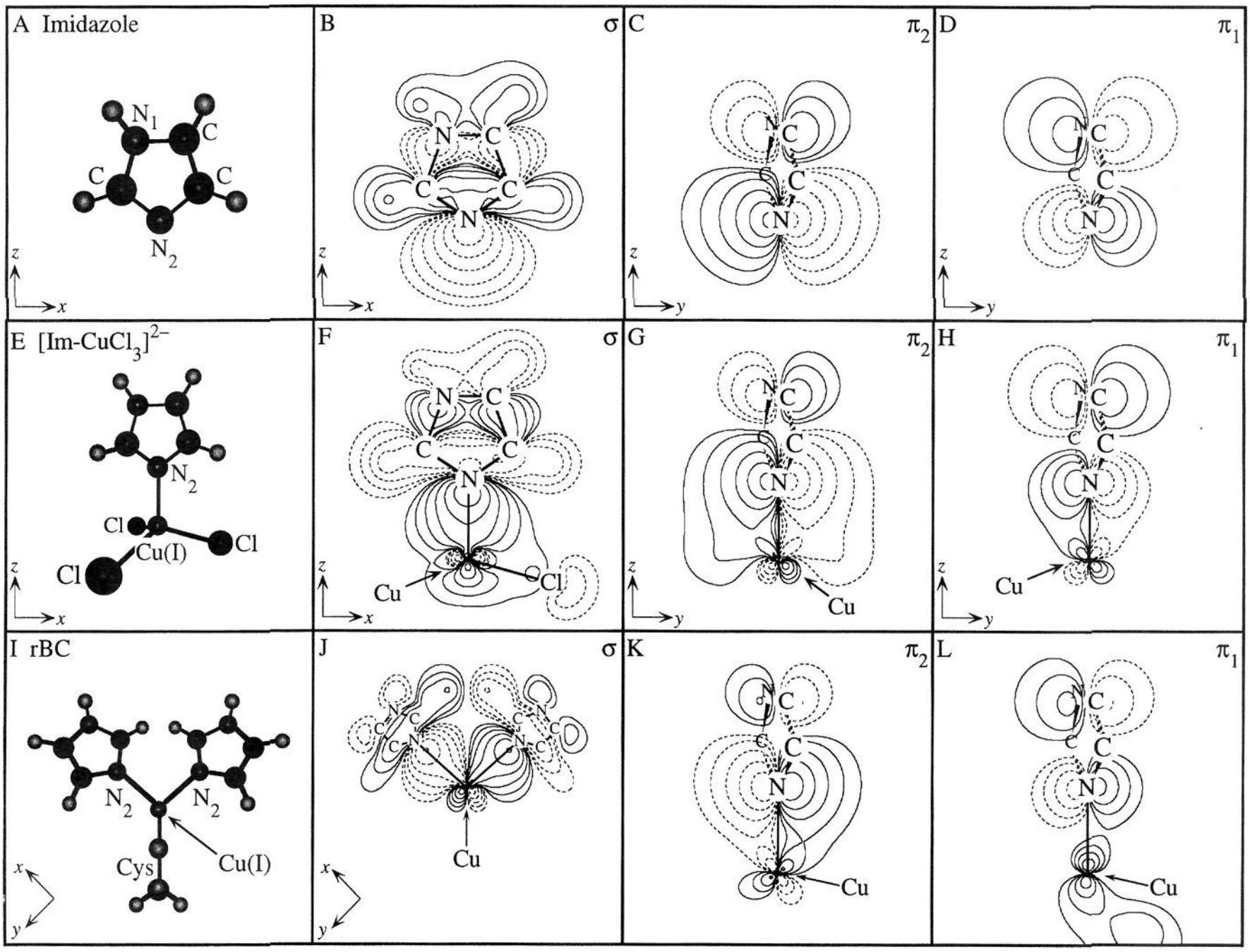

Figure 10. (A) Model of the unbound imidazole ligand in the Cu(I) bonding orientation used in the SCF-Xα-SW calculations. (B−D) SCF-Xα-SW electronic density contour diagrams of highest occupied molecular orbitals of imidazole—(B) σ (ligand in the plane of the page), (C) π_2, and (D) π_1 (ligand plane perpendicular to the page). (E) Model of $[Im-CuCl_3]^{2-}$ in the SCF-Xα-SW geometry. (F−H) SCF-Xα-SW electronic density contour diagrams of the three highest energy imidazole valence bonding orbitals of $[Im-CuCl_3]^{2-}$ in the same orientation as B−D—(F) imidazole σ, (G) imidazole π_2, and (H) imidazole π_1. (I) Model of rBC, where the Met has been removed for clarity. (J−L) SCF-Xα-SW electronic density contour diagrams of the three highest energy His valence bonding orbitals of rBC, in the same orientation as B−D—(J) His σ, (K) His π_2, and (L) His π_1. Contour lines represent electron densities of ±0.01, ±0.02, ±0.04, ±0.008, ±0.16, ±0.32 $(e^-/bohr^3)^{1/2}$.

Table 1. SCF-Xα-SW Results for $[Im-CuCl_3]^{2-}$

			% Cu				% N_2 (Im)[a]				
level	orbital label	energy (eV)	s	p	d	f	s	p	d	% Im[b] (total)	% Cl (total)
20a′	Cu d_{z^2}	−1.36	0	6	76	1	1	3	1	3	9
10a″	Cu d_{xy}	−1.50		3	82	0		0	0	1	13
19a′	Cu $d_{x^2-y^2}$	−1.52	0	3	83	0	0	0	0	0	14
9a″	Cu d_{yz}	−1.82		0	91	0		0	1	3	5
18a′	Cu d_{xz}	−1.87	0	0	93	0	0	0	1	0	6
8a″	His π_1	−3.59		0	1	0		6	3	89	2
3a″	His π_2	−6.21		3	2	0		47	0	40	7
12a′	His σ	−8.53	9	7	8	3	8	42	1	20	2
2a″	His π_3	−9.80		0	0	0		7	0	92	0
11a′	His C−H	−9.80	0	0	0	0	0	7	2	91	0
10a′	His C−H	−10.67	0	0	0	0	0	4	0	95	0
9a′	His C−H	−11.61	0	0	0	0	1	6	0	93	0
8a′	His C−H	−15.65	0	0	0	0	1	21	3	74	0

[a] The coordinating nitrogen of imidazole. [b] Sum of charges for all atoms in the imidazole ring except N_2.

3d orbitals will *not* contribute to the overall stability of the Cu(I)−imidazole bond. Therefore, the strength of the Cu(I)−imidazole bond derives chiefly from ligand interaction with the Cu 4s and 4p orbitals. From Table 1, the greatest Cu 4s and 4p contributions to the Cu(I)−imidazole bond arise as σ overlap with the 12a′ His σ MO, which includes a total of 16% Cu(I) 4s and 4p character, whereas only 3% Cu(I) 4p character is observed in the 3a″ imidazole π_2 orbital, indicating very weak π contributions to Cu(I)−imidazole bonding.

The dominant σ interactions of the Cu(I)−imidazole bond are also revealed in the sums of the valence electron occupations for the calculations of imidazole, $CuCl_3^{2-}$, and $[Im-CuCl_3]^{2-}$, listed in Table 2. Shifts in electron occupancies for imidazole and $CuCl_3^{2-}$ upon bonding to each other are also listed in the

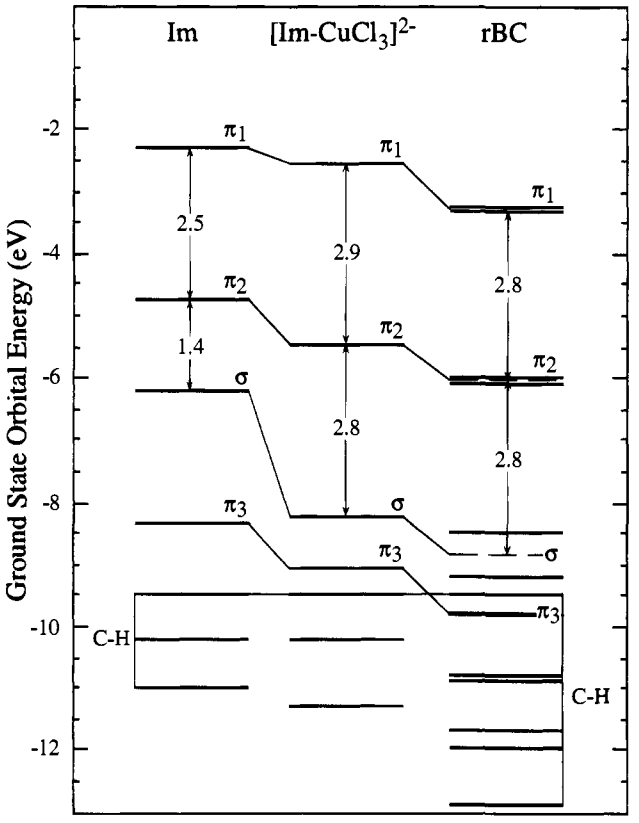

Figure 11. Valence molecular levels from SCF-Xα-SW calculations of imidazole, $[Im-CuCl_3]^{2-}$ and rBC. The highest energy C−H orbitals have been aligned to the unbound ligand. Orbital energies have been adjusted for intersphere constant potential contributions. The chloride-derived levels are not shown.

Table 2. Electron Populations for $CuCl_3^{2-}$, Imidazole, and $[Im-CuCl_3]^{2-}$

orbital	$CuCl_3^{2-}$	$[Im-CuCl_3]^{2-}$	Δe^-
Cu s	0.62	0.59	−0.03
Cu p_x	0.39	0.37	−0.02
Cu p_y	0.39	0.39	+0.00
Cu p_z	0.12	0.43	+0.31
Cu $d_{x^2-y^2}$	2.10	2.09	−0.01
Cu d_{xz}	2.02	2.01	−0.01
Cu d_{z^2}	1.97	1.96	−0.01
Cu d_{yz}	2.02	2.00	−0.02
Cu d_{xy}	2.10	2.10	−0.00
orbital	imidazole	$[Im-CuCl_3]^{2-}$	Δe^-
N_2 s	1.28	1.19	−0.09
N_2 p_x	1.27	1.26	−0.01
N_2 p_y	1.16	1.10	−0.06
N_2 p_z	1.50	1.27	−0.23

final column of the table. The results in Table 2 indicate that nearly all of the charge donated by imidazole is transferred to the $4p_z$ orbital of Cu(I) and the charge donated to Cu(I) originates almost entirely from the ligand N_2 p_z orbital, the primary component of the imidazole σ MO. Significantly less electronic charge is lost from the N_2 $2p_y$ orbital upon bonding to the surface site, a further indication of weak π bonding since the N_2 $2p_y$ orbital is the main component of the imidazole π_1 and π_2 orbitals. The 12a′ imidazole σ orbital contains 9% Cu 4s character (Table 1); however, no increase is seen in the total electron occupation of the 4s orbital summed over all the valence levels (Table 2), indicating that no additional Cu(I) 4s bonding contribution is associated with imidazole binding to the surface. The lack of additional Cu(I) 4s bonding in the $[Im-CuCl_3]^{2-}$ calculation is consistent with resonance PES of the surface complex in Figure 4D, which exhibits no shift in the Cu 4s energy upon imidazole bonding. Thus, the ligand donation in the Cu(I)−imidazole bond consists primarily of imidazole σ → Cu(I) $4p_z$ charge transfer.

Although the filled Cu 3d orbitals do not contribute to bonding through overlap with the filled ligand valence orbitals, Cu 3d orbitals may contribute to the Cu(I)−imidazole bond strength through back donation of electronic charge into the unoccupied imidazole π* orbitals. However, no substantial loss of Cu 3d electron density is observed in Table 2, indicating very little metal-to-ligand π* back bonding in agreement with the N 2s XPS results for Cu(I)-bound imidazole in Figure 5A. In summary, the Cu(I)−imidazole bond can be described as predominantly σ donation arising from imidazole σ → Cu $4p_z$ charge transfer, with weak π contributions and no significant participation from Cu 3d → Im π* back bonding.

In a number of instances throughout this study, NH_3 has been substituted for the imidazole ligand in calculating the electronic structure of Cu(I) models. Molecular orbital calculations of $[H_3N-CuCl_3]^{2-}$ indicate that NH_3, a pure σ donor, donates 0.30 electron to Cu(I) compared to 0.22 electron donated by the σ orbital of imidazole. Thus, the NH_3 substitution greatly reduces the time required per calculation while not significantly altering the SCF-Xα-SW Cu(I)−N bonding description.

2. Dimethyl Sulfide. SCF-Xα-SW molecular orbital calculations have been performed on an unbound dimethyl sulfide molecule and $(CH_3)_2S$ axially coordinated to a C_{3v} $CuCl_3^{2-}$ cluster to quantitatively complement the PES experiments on the $(CH_3)_2S$/CuCl(111) surface system presented in Section III.A. The unbound thioether molecule was oriented for the calculation such that the *xz*-plane contains the sulfur atom and both methyl carbon atoms. In both model clusters, the thioether ∠C−S−C angle was fixed at 98.6° and a S−C bond length of 1.82 Å was used. A Cu(I)−thioether bond length of 2.30 Å was used in the $[(CH_3)_2S-CuCl_3]^{2-}$ cluster, consistent with typical Cu(I)−thioether compounds. A complete list of atomic coordinates and input values for the $[(CH_3)_2S-CuCl_3]^{2-}$ calculation is available as supplementary material.

The SCF-Xα-SW Slater transition state energies for unbound thioether in Figure 6E agree well with the experimental ionization energies of the gas-phase thioether photoemission spectrum[63] in Figure 6D. Importantly, the experimental splittings of the highest occupied ligand orbitals (b_1, a_1, and b_2) are accurately reproduced by the calculation, with the b_1 ionization at 8.8 eV, the a_1 ionization at 11.1 eV, and the b_2 ionization at 12.3 eV.

In order to reproduce the chemisorbed thioether photoemission spectrum in Figure 6C, $[(CH_3)_2S-CuCl_3]^{2-}$ model calculations were carried out at a series of C_s geometries, where the angle θ formed by the C−S−C thioether plane and the molecular *z*-axis (Scheme 2) was varied from 90 to 180° while maintaining a constant Cu(I)−S bond length. In Figure 12, shifts in electronic charge density of the ligand and metal bonding orbitals are plotted as a function of θ. These electronic shifts reveal that the most effective charge donation of the thioether S 3p orbitals occurs at angles near 100°, and the amount of electronic charge gained in the Cu 4p orbitals exhibits a broad maximum between 100 and 120°; therefore, the strongest ligand−metal interaction is expected at $\theta \approx 110°$. Typical sterically unconstrained Cu(I)−thioether complexes do in fact exhibit θ values near 110°. For the $[(CH_3)_2S-CuCl_3]^{2-}$ calculation, the best agreement with the PES ionization energies in Figure 6C was found for $\theta = 110°$, indicating that the Cu(I)−thioether bonding at the CuCl(111) surface is sterically unstrained. The $[(CH_3)_2S-CuCl_3]^{2-}$ Slater transition state

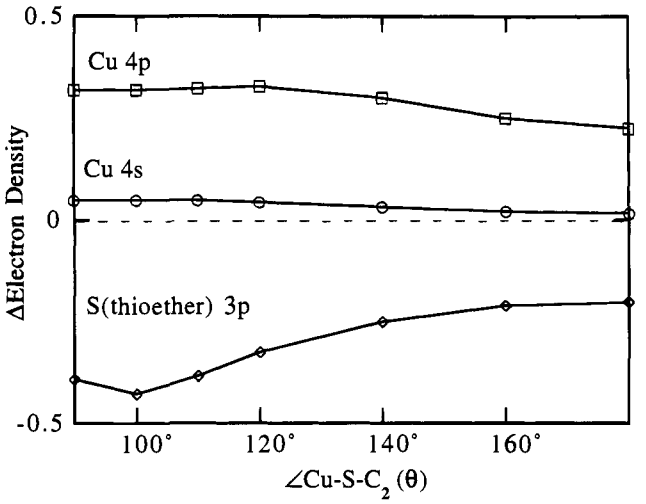

Figure 12. Cu 4s, Cu 4p, and S 3p electron density changes upon bonding for $[(CH_3)_2S-CuCl_3]^{2-}$ plotted as a function of θ, the angle between the Cu(I)−S bond and the C−S−C plane of the $(CH_3)_2S$ ligand.

energies of the three highest occupied ligand valence orbitals, shown in Figure 6F, also match the experimental values extremely well, with the b_1 ionization at 9.8 eV, the a_1 ionization at 11.3 eV, and the b_2 ionization at 12.1 eV.

SCF-Xα-SW electron density contour plots of the thioether b_1, a_1, and b_2 molecular orbitals are presented in Figure 13 for unbound thioether (Figure 13B−D) and thioether bound to $CuCl_3^{2-}$ (Figure 13F−H). SCF-Xα-SW descriptions of the highest occupied valence orbitals of $[(CH_3)_2S-CuCl_3]^{2-}$ are presented in Table 3, where Met refers to the thioether ligand, and ground state energy level diagrams of unbound thioether and $[(CH_3)_2S-CuCl_3]^{2-}$ are presented in Figure 14. As described for the corresponding Cu(I)−Im energy level diagram, the highest energy C−H level of the surface model (level 4a″) has been aligned to the corresponding C−H level of the free ligand since no Cu(I) character is gained in this MO upon bonding to the $CuCl_3^{2-}$ cluster (Table 3), and, therefore, no stabilization of this level is expected.

Consistent with the PES data presented in Section III.A, the SCF-Xα-SW results in Table 3 indicate that Cu(I)−thioether bonding consists predominantly of thioether b_1 and a_1 orbital interactions. The 10a′ Met b_1 orbital exhibits the greatest amount of Cu(I) mixing upon bonding to the Cu(I) surface site, containing 21% Cu character (Table 3). As a result of the significant Cu(I) overlap, the b_1 level is stabilized by 1.5 eV from the free ligand value in Figure 14. The contour plot in Figure 13D indicates that the unbound thioether b_1 orbital consists of a lone pair, nonbonding with respect to the methyl carbons, and the large S 3p coefficient in the b_1 wave function provides effective overlap with the metal. In addition, at a geometry of $\theta = 110°$, the S 3p lobe of the b_1 MO is oriented only 20° off the Cu(I)−thioether bond axis, forming a strong σ interaction with the Cu $4p_z$ and $3d_{z^2}$ orbitals, seen in Figure 13H. Significant metal character (14%) is also observed in the 7a′ Met a_1 level (Table 3) leading to a 0.9-eV stabilization of this level, Figure 14. Considerable S 3p electron density is available for Cu(I) bonding in the unbound thioether a_1 MO in Figure 13C; however, overlap with the metal is limited by the bonding geometry of the system. While at $\theta = 110°$ thioether a_1 interaction with Cu(I) is still predominantly σ in nature, as seen in Figure 13G, overlap is limited by the fact that the S 3p of the a_1 MO is oriented at an angle of 70° relative to the Cu(I)−thioether bond axis, resulting in a weaker interaction than observed for the b_1 orbital. The 5a″ Met b_2 level contains only 1% Cu(I) character, Table 3. Cu(I) mixing in this orbital is limited by a small sulfur coefficient and by the orientation of the thioether b_2 orbital, which remains purely π with respect to the metal at all angles of θ, Scheme 2.

The sums of the valence electron occupations for each basis function in the SCF-Xα-SW calculations of $(CH_3)_2S$, $CuCl_3^{2-}$, and $[(CH_3)_2S-CuCl_3]^{2-}$ are listed in Table 4, with shifts in electron occupancies listed in the last column. As described above for the Cu(I)−Im system, the strength of the Cu(I)−thioether bond derives chiefly from configurational interaction of the unoccupied Cu 4s and 4p orbitals with the filled ligand valence orbitals. Of the ligand-centered valence orbitals, only the 10a′ Met b_1 nd 7a′ Met a_1 levels contain any significant Cu 4s and 4p character, a total of 9% in each (Table 3). The electronic shifts listed in Table 4 reveal that the Cu(I) 4p participation consists almost entirely of σ charge donation into the Cu $4p_z$ orbital, which gains 0.30 electron, and that the charge donated to the metal center originates from the σ overlap of the S 3p components of Met b_1 (0.24 electron) and a_1 (0.13 electron). The charge donation from the b_1 orbital is greater than that of the a_1 MO because the S 3p component of b_1 is more nearly collinear with the Cu(I)−S bond axis, allowing greater σ overlap. Virtually no charge is donated (0.02 electron, Table 4) by the π-symmetry S 3p component of the thioether b_2 MO. Although the 7a′ Met a_1 orbital wave function contains 6% Cu 4s character (Table 3), the sum of Cu 4s electron occupancy summed over all valence levels remains essentially unchanged in $[(CH_3)_2S-CuCl_3]^{2-}$ relative to the $CuCl_3^{3-}$ cluster; therefore, the orbital energy of the Cu 4s level is not expected to shift upon thioether bonding, consistent with PES results which show no shift in the intensity resonance maximum of the Cu 3d valence satellite in Figure 4E. Finally, in agreement with the S 2p XPS spectrum of the surface-bound thioether, in which no shakeup satellite structure is observed, the lack of any significant electron loss in the Cu 3d manifold upon thioether binding in Table 4 indicates an absence of any significant Cu 3d back donation into the unoccupied thioether S 3d orbitals. The apparent gain of 0.16 electron in the Cu $3d_{z^2}$ orbital represents a redistribution of electron density within the 3d manifold, which sums to a negligible gain of +0.03 electron.

In summary, for a bonding geometry of $\theta = 110°$, the Cu(I)−thioether bond can be described as a strong σ bond comprised primarily of thioether b_1, $a_1 \rightarrow$ Cu $4p_z$ σ charge transfer. At this angle, the b_1 orbital dominates the bonding scheme, contributing twice the charge to Cu(I) as the a_1 MO. No significant π bonding or metal-to-ligand back donation contributes to the Cu(I)−thioether electronic structure.

3. Methanethiolate. SCF-Xα-SW molecular orbital calculations have also been performed on an unbound CH_3S^- anion and a series of clusters to model thiolate bonding to Cu(I) surface sites. A constant Cu(I)−S bond length of 2.20 Å was maintained for all surface-bonding models, consistent with typical Cu(I)−thiolate compounds, and a S−C bond length of 1.82 Å was used. The Slater transition state energies for the highest occupied levels of unbound CH_3S^- are presented in Figure 8D, with the degenerate π lone pair ionizations at 12.3 eV and the a_1 (S−C) σ ionization at 15.7 eV.

Thiolate bound to the $Cu_2O(111)$ surface was modeled using a $[CH_3S-Cu(OH)_2]^{2-}$ cluster, in which the two oxygen atoms form a 120° angle with copper in the *xz*-plane. Protons were added to the oxides to compensate for the positive charge of Cu ions in the extended lattice of the crystal. SCF-Xα-SW calculations on the $[CH_3S-Cu(OH)_2]^{2-}$ cluster were performed for a range of C_s geometries where the ∠Cu−S−C angle (ϕ) was varied from 90 to 180° by rotating the S−C bond in the

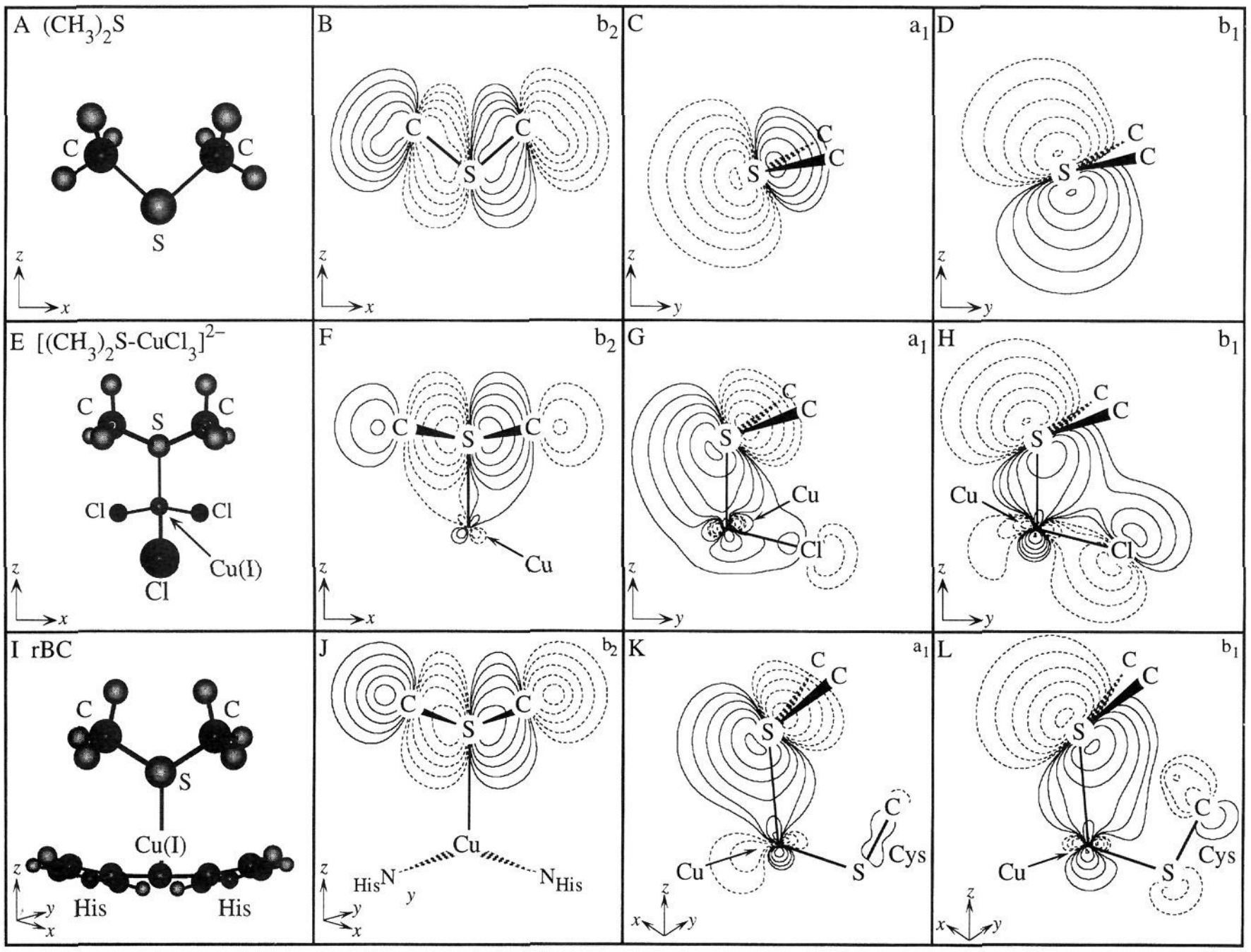

Figure 13. (A) Model of the unbound dimethyl thioether ligand in the Cu(I) bonding orientation used in the SCF-Xα-SW calculations. (B−D) SCF-Xα-SW electronic density contour diagrams of the three highest energy valence bonding orbitals of thioether—(B) b_2 (CSC plane in the plane of the page), (C) a_1, and (D) b_2 (CSC plane perpendicular to the plane of the page). (E) Model of $[(CH_3)_2S{-}CuCl_3]^{2-}$ in the SCF-Xα-SW geometry ($\theta = 110°$). (F−H) SCF-Xα-SW electronic density contour diagrams of the three highest energy thioether valence bonding orbitals of $[(CH_3)_2S{-}CuCl_3]^{2-}$ in the same orientation as B−D—(F) thioether b_2, (G) thioether a_1, and (H) thioether b_1. (I) Model of rBC, where the Cu(I)−S(Met) bond corresponds to the z-axis in the plane of the page. (J−L) SCF-Xα-SW electronic density contour diagrams of the three highest energy Met valence bonding orbitals of the rBC in the same orientation as B−D—(J) Met b_2, (K) Met a_1, and (L) Met b_1. Contour lines represent electron densities of ± 0.01, ± 0.02, ± 0.04, ± 0.008, ± 0.16, ± 0.32 $(e^-/bohr^3)^{1/2}$.

Table 3. SCF-Xα-SW Results for $[(CH_3)_2S{-}CuCl_3]^{2-}$

			% Cu				% S (thioether)				
level	orbital label	energy (eV)	s	p	d	f	s	p	d	% $(CH_3)_2$ (total)	% Cl (total)
16a′	Cu d_{z^2}	−1.02	0	4	78	1	0	6	1	1	8
15a′	Cu $d_{x^2-y^2}$	−1.13	0	4	79	0	0	0	0	0	15
11a″	Cu d_{xy}	−1.13		4	79	0		0	0	0	15
14a′	Cu d_{yz}	−1.49	0	0	91	0	0	0	1	1	7
10a″	Cu d_{xz}	−1.52		0	88	0		0	1	1	8
10a′	Met b_1	−4.85	0	9	11	1	0	53	0	9	16
7a′	Met a_1	−7.17	6	3	3	1	3	47	2	30	3
5a″	Met b_2	−8.27		0	0	0		34	4	62	0
4a″	C−H	−9.66		0	0	0		5	0	95	0
3a″	C−H	−10.02		0	0	0		4	0	95	0
6a′	C−H	−10.06	0	0	0	0	0	4	1	95	0
5a′	C−H	−10.40	0	0	0	0	0	4	0	94	0
4a′	S 3s	−14.45	1	1	1	0	42	0	0	53	0

yz-plane (Scheme 3). In Figure 15, shifts in electronic charge density of the ligand and metal bonding orbitals plotted as a function of ϕ reveal that thiolate S 3p charge donation and Cu 4p and 4s charge acceptance are most effective for values of ϕ near 110°, consistent with the bonding angles generally observed for Cu(I)−thiolate species. However, an angle of $\phi = 140°$ was required to match the SCF-Xα-SW Slater transition state energies in Figure 8E to the photoemission spectrum of $CH_3S/Cu_2O(111)$ in Figure 8C. A space-filling model of the Cu_2O-(111) surface using ionic radii indicates that a Cu−S−C angle of at least 120° is required to avoid close contacts of the thiolate methyl hydrogens with the oxides of the $Cu_2O(111)$ surface.

Compared to the PES results in Figure 8C, the Slater transition state energies for the $[CH_3S{-}Cu(OH)_2]^{2-}$ calculation at $\phi =$

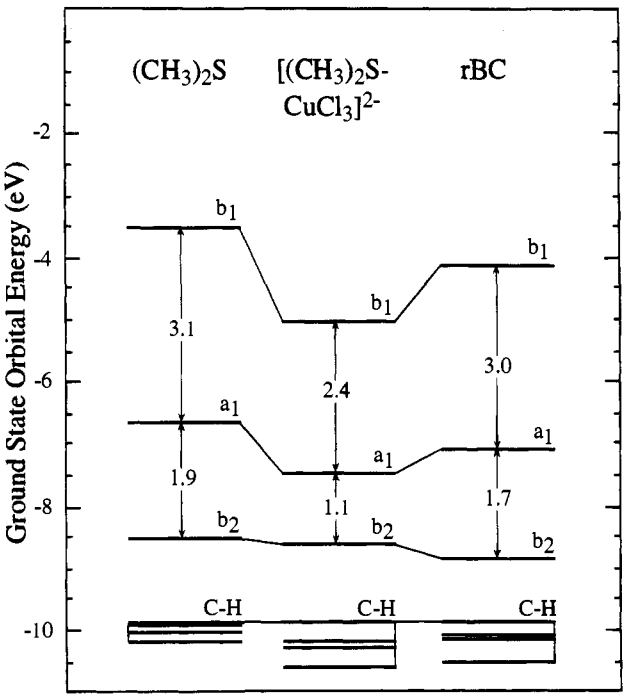

Figure 14. Valence molecular levels from SCF-Xα-SW calculations of $(CH_3)_2S$, $[(CH_3)_2S-CuCl_3]^{2-}$ (θ = 110°), and rBC. The highest energy C−H orbitals have been aligned to the unbound ligand. Orbital energies have been adjusted for interesphere constant potential contributions. The chloride-derived levels are not shown.

Table 4. Electron Populations for $CuCl_3^{2-}$, $(CH_3)_2S$, and $[(CH_3)_2S-CuCl_3]^{2-}$ (θ = 110°)

orbital	$CuCl_3^{2-}$	$[(CH_3)_2S-CuCl_3]^{2-}$	Δe^-
Cu s	0.62	0.67	+0.05
Cu p_x	0.39	0.40	+0.01
Cu p_y	0.39	0.40	+0.01
Cu p_z	0.12	0.42	+0.30
Cu $d_{x^2-y^2}$	2.10	2.06	−0.04
Cu d_{xz}	2.02	1.98	−0.04
Cu d_{z^2}	1.97	2.13	+0.16
Cu d_{yz}	2.02	2.00	−0.02
Cu d_{xy}	2.10	2.07	−0.03
orbital	$(CH_3)_2S$	$[(CH_3)_2S-CuCl_3]^{2-}$	Δe^-
S s	1.71	1.69	−0.02
S p(b_1)	1.76	1.52	−0.24
S p(a_1)	1.28	1.15	−0.13
S p(b_2)	0.98	0.96	−0.02

140° accurately reproduce the experimental ionization energies, with the (S−C)σ orbital at 17.1 eV, and the degenerate π lone pairs of the free ligand split by 0.8 eV upon bonding to the $Cu_2O(111)$ surface. At a linear bonding geometry, ϕ = 180°, both the thiolate S 3p lone pairs are oriented π with respect to the Cu(I) ion. As the S−C bond is rotated in the *yz*-plane (ϕ < 180°), the in-plane π lone pair is rotated toward the Cu(I)−S bond axis and overlap with Cu(I) becomes increasingly σ in character; therefore, this lone pair is referred to as the pseudo-σ orbital (Scheme 3C). The greater σ overlap in the pseudo-σ orbital results in greater stabilization of this level relative to the thiolate π orbital. The Cu(I) overlap with the out-of-plane lone pair remains purely π with respect to the Cu(I) ion for all values of ϕ.

Having effectively reproduced the Cu(I)−thiolate bonding observed experimentally using PES, SCF-Xα-SW calculations were also performed on $[CH_3S-Cu(OH)_2]^{2-}$ with an unconstrained Cu(I)−S(thiolate) angle of ϕ = 110°. The charge distributions of the highest occupied molecular orbitals of

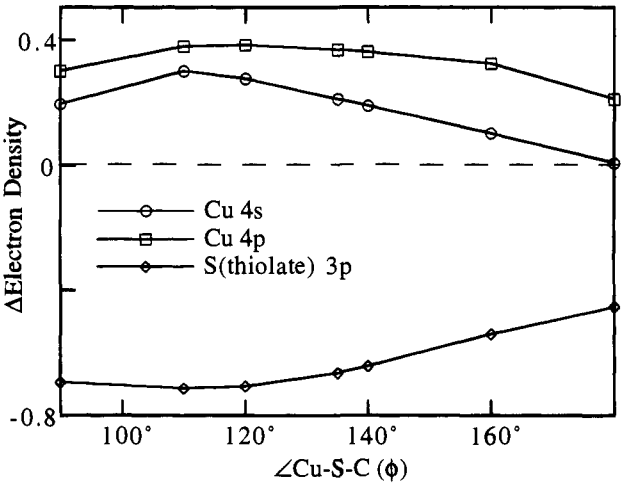

Figure 15. Cu 4s, Cu 4p, and S 3p electron density changes upon bonding for $[CH_3S-CuCl_3]^{2-}$ plotted as a function of ∠CSCu (ϕ).

$[CH_3S-Cu(OH)_2]^{2-}$ at ϕ = 110° and 140° are presented in Table 5, where Cys refers to the thiolate ligand. The largest difference observed in the bonding descriptions of the two models is a small, 5% decrease in Cu(I) character in the Cys σ orbital on reducing ϕ by 30°, indicating that only minor quantitative bonding differences exist between the two geometric models. Additionally, to facilitate comparisons with the calculated electronic structure descriptions of Cu(I)−thioether and Cu(I)−imidazole bonding, SCF-Xα-SW calculations were also performed on thiolate bound to a $CuCl_3^{2-}$ cluster. For the $[CH_3S-CuCl_3]^{3-}$ calculation, the unconstrained geometry of ϕ = 110° was used. The SCF-Xα-SW wave functions of the highest occupied molecular orbitals pf $[CH_3S-CuCl_3]^{3-}$ (Table 5) indicate that the electronic structure description of thiolate bonding to $CuCl_3^{2-}$ at ϕ = 110° is consistent with the description of CH_3S^- bound to $Cu(OH)_2^-$ in the same geometry. The most significant change on going to the $[CH_3S-CuCl_3]^{3-}$ model is a 5% increase in the Cu character of the Cys pseudo-σ orbital. Thus, the qualitative SCF-Xα-SW electronic structure description of Cu(I)−thiolate bonding is consistent in the three models investigated, $[CH_3S-Cu(OH)_2]^{2-}$ is ϕ = 140° and 110° and $[CH_3S-CuCl_3]^{3-}$ at ϕ = 110°. All succeeding discussions of Cu(I)−thiolate electronic structure refer to the results of the $[CH_3S-CuCl_3]^{3-}$ model calculation at a bonding angle of ϕ = 110°. Complete lists of atomic coordinates and input values for the calculations of free thiolate and thiolate bound to $Cu(OH)_2^-$ and $CuCl_3^{2-}$ are available as supplementary material.

SCF-Xα-SW electron density contour plots are presented in Figure 16 for the ligand-derived π, pseudo-σ, and σ molecular orbitals of unbond thiolate (Figure 16, parts B−D) and $[CH_3S-CuCl_3]^{3-}$ (Figure 16, parts F−H). A more complete description of the SCF-Xα-SW derived valence orbitals of the $[CH_3S-CuCl_3]^{3-}$ model is presented in Table 6, and the ground state orbital energy level diagrams of unbound thiolate and $[CH_3S-CuCl_3]^{3-}$ (ϕ = 110°) are presented in Figure 17. Consistent with the alignment used in the energy level diagrams of imidazole and thioether, the highest energy 2a″ C−H level of the $[CH_3S-CuCl_3]^{3-}$ calculation (Table 6) has been aligned to the corresponding free ligand C−H level in Figure 17 since this level exhibits no Cu(I) mixing in $[CH_3S-CuCl_3]^{3-}$.

The SCF-Xα-SW orbital wave functions in Table 6 reveal significant Cu(I) interaction with all three of the highest occupied thiolate valence orbitals (π, pseudo-σ, and σ) of $[CH_3S-CuCl_3]^{3-}$. Of the three highest occupied Cys valence orbitals, the 12a′ Cys pseudo-σ orbital exhibits the highest Cu(I) covalency, containing 34% Cu(I) character in the $[CH_3S-$

Table 5. SCF-Xα-SW Comparison of Three CH_3S−Cu(I) Surface Models

	% charge											
	$[CH_3S-Cu(OH)_2]^{2-}$ ($\phi = 140°$)				$[CH_3S-Cu(OH)_2]^{2-}$ ($\phi = 110°$)				$[CH_3S-CuCl_3]^{3-}$ ($\phi = 110°$)			
orbital	Cu	S	CH_3	OH	Cu	S	CH_3	OH	Cu	S	CH_3	Cl_3
Cu d_{z^2}	76	10	1	13	79	8	1	12	69	15	4	12
Cu d_{xz}	70	21	1	6	72	19	1	6	72	13	2	13
Cu $d_{x^2-y^2}$	86	0	0	14	88	0	0	12	83	1	0	16
Cu d_{xy}	85	8	2	5	91	4	2	3	83	7	0	9
Cu d_{yz}	98	1	0	1	99	1	0	0	90	2	1	7
Cys π	24	54	2	17	23	57	3	15	23	59	5	14
Cys pseudo-σ	31	60	6	2	29	57	8	6	34	55	5	6
Cys σ	19	49	31	1	14	51	34	0	15	47	31	7
C−H	0	4	96	0	1	6	93	0	1	5	93	0
C−H	0	4	96	0	0	4	96	0	0	4	96	0
S 3s	12	58	30	0	11	56	33	0	10	57	33	0

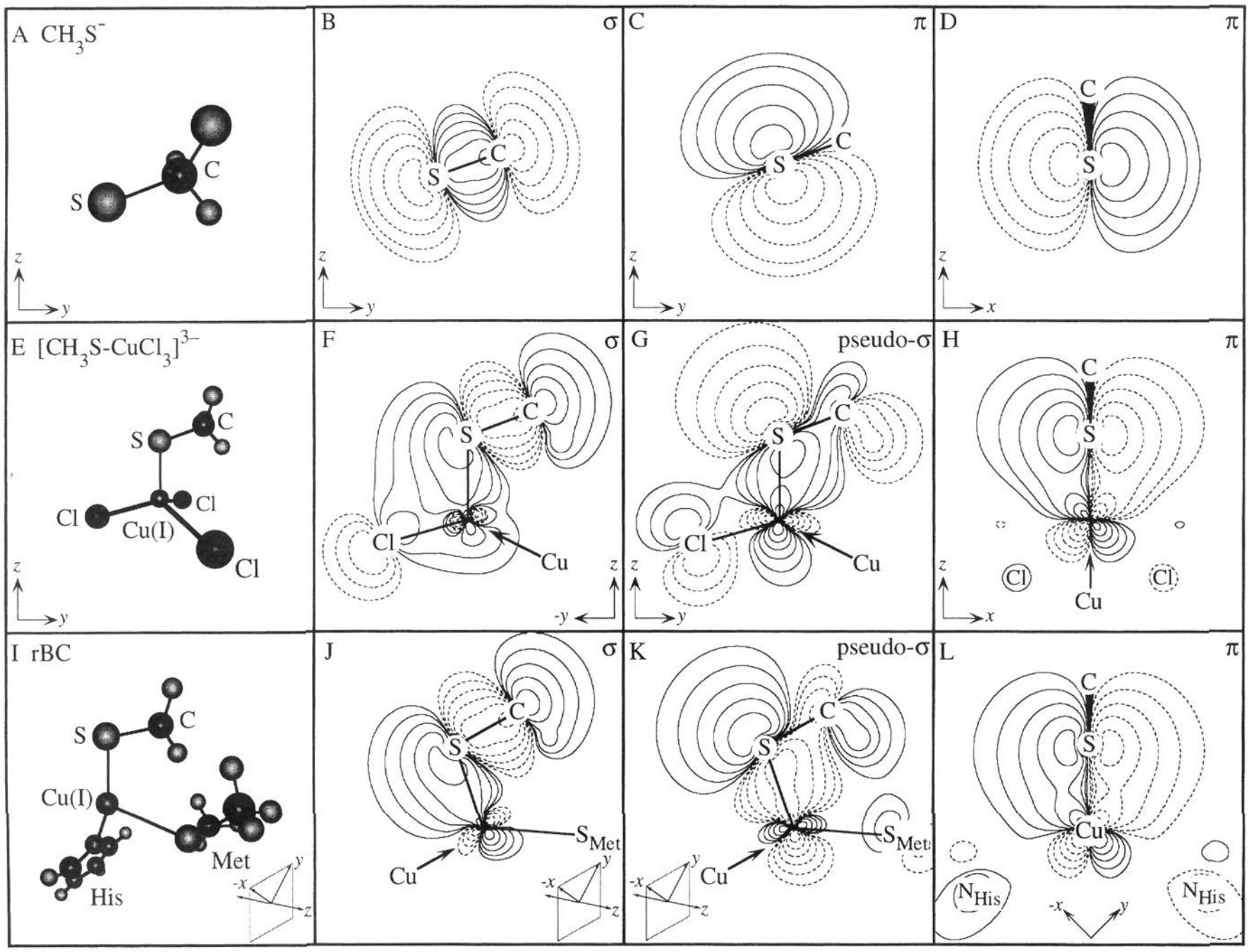

Figure 16. (A) Model of the unbound methanethiolate ligand in the Cu(I) bonding orientation used in the SCF-Xα-SW calculations. (B−D) SCF-Xα-SW electronic density contour diagrams of the three highest energy valence bonding orbitals of thiolate—(B) σ and (C) in-plane π (S−C bond in the plane of the page), and (D) out-of-plane π (rotated 90° about the z-axis so that the S−C bond is coming out of the page). (E) Model of $[CH_3S-CuCl_3]^{3-}$ in the SCF-Xα-SW geometry ($\phi = 110°$). (F−H) SCF-Xα-SW electronic density contour diagrams of the three highest energy methanethiolate valence bonding orbitals of $[CH_3S-CuCl_3]^{3-}$, in the same orientation as B−D—(F) thiolate σ, (G) thiolate pseudo-σ, and (H) thiolate π. (I) Model of the rBC (CuSC plane in the plane of the page). (J−L) SCF-Xα-SW electronic density contour diagrams of the three highest energy Met valence bonding orbitals of the rBC in the same orientation as B−D—(J) Met σ, (K) Met pseudo-σ, and (L) Met π. Contour lines represent electron densities of ±0.01, ±0.02, ±0.04, ±0.008, ±0.16, ±0.32 $(e^-/bohr^3)^{1/2}$.

$CuCl_3]^{3-}$ complex (Table 6). The strong Cu(I) overlap in the pseudo-σ level is reflected in a greater stabilization of this level from the free ligand π value in Figure 17. As described above, the pseudo-σ orbital derives from the degenerate π lone pairs of the free ligand, which are available for bonding to the Cu(I) surface site since these orbitals are nonbonding with respect to the thiolate methyl group, consisting mostly of S 3p character (Figure 16, parts C and D). At $\phi = 110°$ the S 3p component of the pseudo-σ orbital is oriented only 20° off the Cu(I)−S bond axis, resulting in the strong σ overlap with Cu(I) seen in Figure 16G and the high metal−ligand covalency seen in Table 6. Considerable Cu(I) mixing is also seen in the out-of-plane 7a″ Cys π orbital which contains 23% Cu character (Table 6). Relative to the in-plane pseudo-σ orbital, thiolate π interaction

Table 6. SCF-Xα-SW Results for $[CH_3S-CuCl_3]^{3-}$ ($\phi = 110°$)

level	orbital label	energy (eV)	% Cu s	% Cu p	% Cu d	% Cu f	% S(thiolate) s	% S(thiolate) p	% S(thiolate) d	% CH_3 (total)	% Cl (total)
15a′	Cu d_{z^2}	−1.16	0	13	54	2	1	13	1	4	12
9a″	Cu d_{xz}	−1.39		2	68	1		12	1	2	13
14a′	Cu $d_{x^2-y^2}$	−1.53	0	3	80	0	0	0	1	0	15
8a″	Cu d_{xy}	−1.73		1	82	0		7	0	1	9
13a′	Cu d_{yz}	−1.94	0	0	90	0	0	0	2	1	7
7a″	Cys π	−2.96		1	19	2		58	0	5	13
12a′	Cys pseudo-σ	−3.95	3	5	25	1	1	52	1	5	6
6a′	Cys σ	−6.91	8	3	3	1	2	41	4	32	7
2a″	C−H	−8.59	0	0	0	0	0	4	1	93	0
5a′	C−H	−8.67		0	0	0		3	1	96	0
4a′	S 3s	−12.79	2	3	3	1	56	2	0	32	0

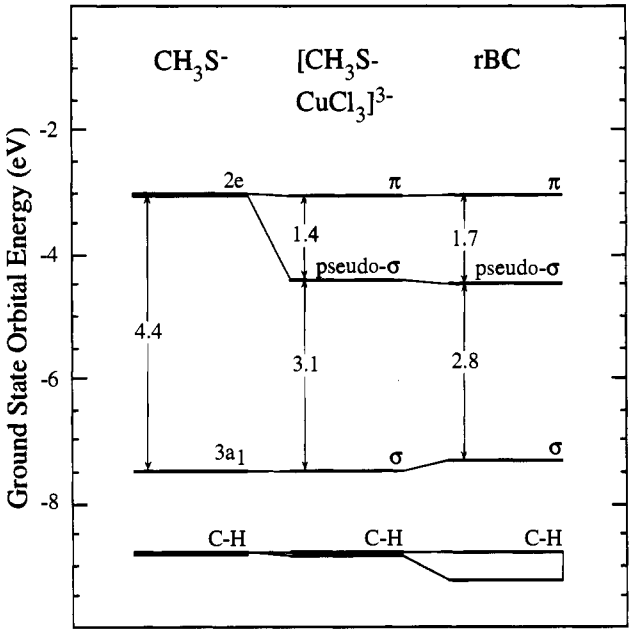

Figure 17. Valence molecular levels from SCF-Xα-SW calculations of CH_3S^-, $[CH_3S\text{-}CuCl_3]^{2-}$ ($\phi = 110°$), and rBC. The highest energy C−H orbitals have been aligned to the unbound ligand. Orbital energies have been adjusted for intersphere constant potential contributions. The chloride-derived levels are not shown.

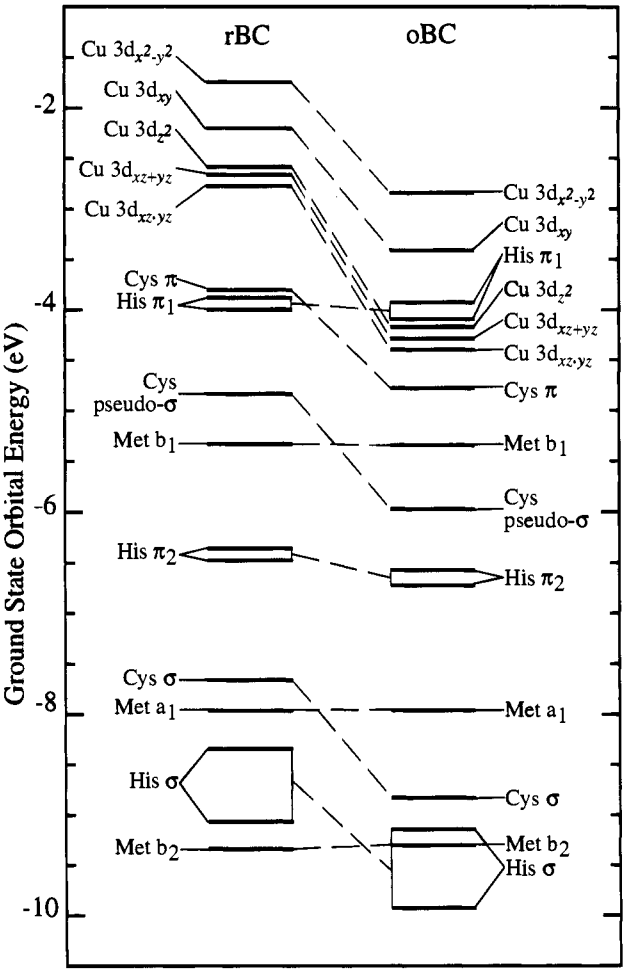

Figure 18. Valence molecular levels from SCF-Xα-SW calculations of rBC and oBC. Orbital energies of oBC have been aligned to the Met a_1 level of rBC. No adjustments have been made for intersphere constant potential contributions.

with Cu(I) is limited by the pure π-symmetry of the orbital; however, significant Cu(I) overlap is observed in the electron density contour plot of this MO, Figure 16H. The stabilization of the Cys π level observed in Figure 17 is small when compared to the extent of Cu(I) mixing in this level due to the energies of the CH_3S^- valence orbitals being too low.[72] The π overlap is also reflected in the extent of thiolate mixing in the Cu 3d manifold of $[CH_3S-CuCl_3]^{3-}$ (Table 6), where the 13% S(thiolate) covalency in the π-symmetry 9a″ Cu $3d_{xz}$ orbital is nearly equal to the 15% S in the σ-oriented 15a′ Cu $3d_{z^2}$ orbital. Overlap of the 6a′ Cys σ orbital in Figure 16B with Cu(I) is limited by the strong S−C interaction in this MO, which draws electron density from the Cu(I)−S bond, and by the fact that at $\phi = 110°$, the S 3p orbital of the thiolate σ MO is rotated 70° off the Cu(I)−S bond axis. Despite these limitations, 15% Cu character is found in the 6a′ Cys σ orbital; however, only a slight stabilization of this level is observed in Figure 18.[72]

The sums of the valence electron occupations for each basis function in the SCF-Xα-SW calculations of CH_3S^-, $CuCl_3^{2-}$, and $[CH_3S\text{-}CuCl_3]^{3-}$ are presented in Table 7, with the shifts in electronic populations listed in the final column. The electronic shifts indicate that nearly all the charge transferred to the metal originates from the S 3p components of the Cys pseudo-σ (0.35 electron) and σ (0.12 electron) orbitals and is gained almost exclusively in the σ-symmetry Cu $4p_z$ orbital (0.52 electron). No electronic charge is donated by the S 3p component of the Cys π MO, nor is any charge gained in the π-symmetry Cu $4p_x$ orbital. Thus, while significant Cu(I) overlap is observed in the π levels of the $[CH_3S-CuCl_3]^{3-}$ system, the metal interaction involves only overlap with the filled Cu 3d orbitals (Table 6) which does not contribute to the overall stabilization of the Cu(I)−thiolate bond. Only a slight gain in the Cu 4s electron charge is seen in Table 7, consistent with the CIS photoemission spectra F and G in Figure 4, which

(72) The adjustments to compensate for the intersphere contribution (see footnote 71) in the π and σ valence orbitals of CH_3S^- were relatively large compared to the C−H reference level in Figure 18, resulting in the π and σ levels of the unbound thiolate being too deep in energy.

Table 7. Electron Populations for $CuCl_3^{2-}$, CH_3S^-, and $[CH_3S-CuCl_3]^{3-}$

orbital	$CuCl_3^{2-}$	$[CH_3S-CuCl_3]^{2-}$	Δe^-
Cu s	0.62	0.70	+0.08
Cu p_x	0.39	0.40	+0.01
Cu p_y	0.39	0.39	+0.00
Cu p_z	0.12	0.64	+0.52
Cu $d_{x^2-y^2}$	2.10	2.07	−0.03
Cu d_{xz}	2.02	2.03	+0.01
CU d_{z^2}	1.97	1.94	−0.03
Cu d_{yz}	2.02	1.99	−0.03
Cu d_{xy}	2.10	2.08	−0.02
orbital	CH_3S^-	$[CH_3S-CuCl_3]^{2-}$	Δe^-
S s	1.81	1.76	−0.05
S p(π)	1.82	1.79	−0.03
S p(pseudo-σ)	1.82	1.47	−0.35
S p(σ)	1.17	1.05	−0.12

reveal no noticeable shift in the resonance intensity maximum of the Cu 3d valence satellite. Finally, no loss of charge is observed in the Cu 3d manifold in Table 6, indicating a lack of metal-to-ligand back donation of charge, consistent with the absence of shake-up satellite structure in the S 2p XPS of CH_3S/Cu_2O(111) in Figure 5C. Thus, the Cu(I)−thiolate bond can be defined as consisting primarily of σ interactions dominated by thiolate S 3p(pseudo-σ) → Cu $4p_z$ charge transfer with weak ligand-to-metal π-bonding contributions and no participation of metal-to-ligand back bonding.

In summary, the bonding of imidazole, thioether, and thiolate to Cu(I) involves, in each case, primarily L p → Cu $4p_z$ σ interactions along the copper C_{3v} axis. The relative increases in electronic charge that occur in the Cu $4p_z$ orbital upon binding each of the three ligands demonstrate that thiolate is the strongest σ donor, followed by thioether and imidazole which are approximately equal in donor strength. No significant ligand-to-metal π contribution or metal-to-ligand back donation is observed in Cu(I) bonding with any of the three ligands.

B. Electronic Structure of the Reduced Blue Copper Site. In the previous section, SCF-Xα-SW electronic structure calculations of imidazole, thioether, and thiolate individually bound to Cu(I) surface sites were calibrated, adjusted, and evaluated with respect to experimental PES data. In this section, the three ligand systems are combined in a $Cu^I[S(CH_3)_2(SCH_3)(N_2C_3H_4)_2]$ model cluster (rBC) to evaluate the electronic structure of the reduced blue copper protein active site.

As described above, the reduced blue copper active site consists of a Cu(I) ion surrounded by four amino acid residues in an approximate elongated C_{3v} site symmetry: an axial methionine at an unusually long distance from the Cu ion; and a cysteine and two histidines bound equatorial to and nearly coplanar with the Cu. For the SCF-Xα-SW calculations of the protein active site the histidine (His), methionine (Met) and cysteine (Cys) amino acid residues of blue copper have been approximated by imidazoles, dimethyl thioether and methanethiolate, respectively, in the C_s(met) approximation, where the imidazole rings are rotated so that they are bisected by a molecular S(Met)−Cu−S(Cys) mirror plane and the Cu(I)−S(Met) bond is collinear with the z axis.

SCF-Xα-SW orbital energies and charge distributions of the highest occupied valence orbitals or rBC are presented in Table 8, and a ground state energy level diagram including all Cu, His, Met, and Cys molecular orbitals above 12 eV is presented in Figure 18. Orbital energies associated with each amino acid residue in the blue copper calculation are also included in the energy level diagrams for the individual ligands in Figures 11, 14, and 18. Analysis of the electronic structure of Cu(I) bonding to each of the amino acid residues at the blue copper active site is presented below.

1. Cu(I)−Histidine. In the reduced active site, the His37 and His87 residues are bonded to Cu approximately in the xy plane of the metal ion. In the C_s(met) approximation used for the SCF-Xα-SW calculations of the blue copper active site, the molecular mirror plane that bisects the imidazoles leads to a″:a′ paired sets of His orbitals corresponding to the out-of-phase and in-phase orbital combinations of the two His ligands. SCF-Xα-SW electronic contour plots of the a′ components of the three highest occupied His orbitals are presented in parts J−L of Figure 10 in orientations corresponding to those of the [Im−$CuCl_3]^{2-}$ contour plots above in parts F−H of Figure 10.

The strongest ligand overlap with the Cu(I) center of the reduced blue copper active site occurs in the 16a″:18a′ His σ orbitals which contain an average of 25% Cu(I) character (Table 8) compared to 27% in the 12a′ His σ level of $[Im-CuCl_3]^{2-}$ (Table 1). The strong σ overlap is illustrated in the electron contour plot of the 18a′ His σ orbital of rBC in Figure 10J, which includes both His ligands in the approximate xy plane of the Cu ion. Similar to Cu(I)−imidazole bonding in the surface model, Cu(I) covalency in the His π levels of rBC is considerably weaker. The 17a″:21a′ His π_2 orbitals contain an average

Table 8. SCF-Xα-SW Results for rBC

			% Cu					% Cys		% Met		% His	
level	orbital label	energy (eV)	Cu[a]	s	p	d	[d orbital breakdown]	S	Cys[b]	S	Met[b]	N_2[c]	His[b]
21a″	Cu $d_{x^2-y^2}$	−1.74	68		2	65	$[0.01d_{xz+yz} + 0.99d_{x^2-y^2}]$	20	3	0	0	6	2
27a′	Cu d_{xy}	−2.20	81	7	7	67	$[0.11d_{z^2} + 0.32d_{xz-yz} + 0.57d_{xy}]$	10	1	2	0	2	3
26a′	Cu d_{z^2}	−2.61	93	1	2	90	$[0.86d_{xz-yz} + 0.13d_{xy}]$	2	1	2	0	1	0
20a″	Cu d_{xz+yz}	−2.69	93		1	92	$[0.98d_{xz+yz} + 0.02d_{x^2}$	2	0	0	0	2	3
25a′	Cu d_{xz-yz}	−2.78	94	0	0	94	$[0.01d_{z^2} + 0.71d_{xz-yz} + 0.29d_{xy}]$	3	1	0	0	1	0
19a″	Cys π	−3.80	28		5	21	$[0.21d_{xz+yz} + 0.88d_{x^2-y^2}]$	48	5	0	0	4	15
18a″	His π_1	−3.89	9		1	8	$[0.51d_{xz+yz} + 0.49d_{x^2-y^2}]$	8	0	0	0	6	77
24a′	His π_1	−4.02	2	0	1	1	$[0.08d_{z^2} + 0.91d_{xz-yz} + 0.01d_{xy}]$	0	0	0	0	7	91
23a′	Cys pseudo-σ	−4.85	35	3	7	22	$[0.20d_{z^2} + 0.07d_{xz-yz} + 0.73d_{xy}]$	58	5	1	0	1	0
22a′	Met b_1	−5.35	7	2	2	3	$[0.91d_{z^2} + 0.07d_{xz-yz} + 0.02d_{xy}]$	1	1	78	12	0	0
17a″	His π_2	−6.38	4		0	3	$[0.89d_{xz+yz} + 0.11d_{x^2-y^2}]$	0	0	0	0	51	45
21a′	His π_2	−6.51	4	0	1	3	$[0.08d_{z^2} + 0.55d_{xz-yz} + 0.37d_{xy}]$	0	0	1	1	50	44
20a′	Cys σ	−7.68	18	2	8	8	$[0.00d_{z^2} + 0.63d_{xz-yz} + 0.37d_{xy}]$	47	31	0	0	3	0
19a′	Met a_1	−8.00	4	0	2	2	$[0.96d_{z^2} + 0.04d_{xy-yz} + 0.00d_{xy}]$	0	0	59	32	3	0
16a″	His σ	−8.35	24		8	14	$[0.02d_{xz+yz} + 0.98d_{x^2-y^2}]$	0	0	0	0	52	24
18a′	His σ	−9.07	25	15	5	3	$[1.00d_{z^2}d_{z^2} + 0.00d_{xz-yz} + 0.00d_{xy}]$	2	3	1	1	49	19
14a″	Met b_2	−9.36	1		0	0	$[0.00d_{xz+yz} + 1.00d_{x^2-y^2}]$	0	0	23	43	4	28

[a] Total charge on the copper ion. [b] Total charge for all atoms of the ligand except for S or N coordinated to Cu. [c] Total charge for the coordinating N_2 atoms.

Table 9. Electron Charge Donation of Imidazole, Thioether, and Thiolate[a]

		$-CuCl_3^{2-}$		−rBC		−oBC	
ligand	unbound Σe^-	Σe^-	Δe^-	Σe^-	Δe^-	Σe^-	Δe^-
imidazole	26.00	25.58	−0.42	25.62	−0.38	25.33	−0.67
thioether	20.00	19.47	−0.53	19.76	−0.24	19.72	−0.28
thiolate	14.00	13.16	−0.84	12.60	−1.40	12.07	−1.93

[a] Summed over all valence levels.

of 4% Cu(I) (Table 8), virtually unchanged from the 3a″ His π_2 level of $[Im-CuCl_3]^{2-}$ (Table 1). The weak π interaction is reflected in the contour plots of the 17a″ His π_2 MO of rBC, Figure 10K, and the 3a″ His π_2 MO of $[Im-CuCl_3]^{2-}$, Figure 10G, which reveal only a slight decrease in the electron density shared between the Cu(I) center and the His N_2 atom in the protein relative to the surface model. In the 18a″:24a′ His π_1 orbitals of the reduced blue copper site, an average of 5% Cu(I) character is observed (Table 8), compared to <1% in the corresponding 8a″ His π_1 level of $[Im-CuCl_3]^{2-}$ (Table 1). The greater Cu(I) character is found primarily in the 18a″ partner of the two His π_1 orbitals, where significant S(Cys) character is also observed. From the contour plot of this MO, shown in Figure 10L, the greater Cu character primarily mixes with the sulfur of the Cys ligand; therefore, the Cu−His interaction is not significantly enhanced in this orbital.

In the Cu 3d manifold of rBC the most significant amount of N_2 character is observed in the 21a″ Cu $3d_{x^2-y^2}$ orbital (Table 8), providing further evidence of predominantly σ overlap with His. Since the equatorial Cu(I)−N(His) bonds are oriented along the lobes of the Cu $3d_{x^2-y^2}$ orbital, Figure 10J, the primary ligand interaction in this metal orbital involves the N_2 2p components of the His σ orbitals.

In the energy level diagram in Figure 11, the His orbitals of the blue copper active site appear to be stabilized relative to the free ligand values to a significantly greater extent than the $[Im-CuCl_3]^{2-}$ levels, despite the comparable Cu(I) mixing observed in the two complexes. These exaggerated energy shifts arise from the alignment of the highest energy His C−H level in the protein to the equivalent free ligand level. The His C−H orbitals of rBC are destabilized relative to the surface site by contributions from the Met b_2 orbital, so that the alignment of the His C−H levels results in a shift of the rBC His orbitals to deeper energy. The splitting of the His σ, π_2, and π_1 orbitals in Figure 11 is consistent, however, with the splitting of the $[Im-CuCl_3]^{2-}$ His orbitals, reflecting similar Cu(I) covalency.

Importantly, the only significant Cu 4s/4p mixing in the orbitals associated with His bonding at the reduced blue copper site is observed in the 16a″:18a′ His σ levels, which contain 0%:15% Cu 4s and 8%:5% Cu 4p character, respectively (Table 8). Thus, charge donation from the equatorial His σ orbitals into the Cu 4s/4p orbitals accounts for nearly all the Cu(I)−N(His) bonding interactions in rBC. Electron occupations summed over the imidazole valence levels for the calculations of unbound imidazole, $[Im-CuCl_3]^{2-}$, and rBC are listed in Table 9, along with the electronic shifts that occur upon His bonding to each of the Cu(I) sites. These shifts indicate that each His ligand donates only slightly less charge to Cu(I) in rBC than in $[Im-CuCl_3]^{2-}$ (0.38 *vs* 0.42 electron). The slight decrease in donor strength can be attributed to the Cu(I) ion in the blue copper site being oriented 0.3 Å above the NNS plane of the His and Cys groups. This orientation slightly diminishes direct σ overlap of the Cu $4p_{xy}$ orbitals with the His ligands, whereas in the surface complex the imidazole is oriented directly along the Cu $4p_z$ orbital. In summary, the electronic structure of the Cu(I)−His bonding in blue copper is qualitatively very similar to that of the $[Im-CuCl_3]^{2-}$ surface complex, consisting almost entirely of N_2(His) → Cu(I) 4s/4p σ charge transfer.

2. Cu(I)−Methionine. The sulfur of Met92 bonds to copper at an unusually long 2.82 Å distance approximately along the z axis with a Cu−S(Met)−C_2 angle (θ) of 130°, larger than the typically observed Cu−thioether value of ≈110°. SCF-Xα-SW electron contour plots of the highest occupied Met b_1, a_1, and b_2 valence orbitals of rBC are shown in Figure 16, parts J−L, in the same orientations as the corresponding contours of $[(CH_3)_2S-CuCl_3]^{2-}$ in Figure 16, parts F−H, with the Cu(I)−S(Met) bond collinear with the z axis.

Compared to the Cu(I)−S(Met) bonding description for the $[(CH_3)_2S-CuCl_3]^{2-}$ system, presented in Section IV.B, the extent of the Cu(I) interaction with the Met valence orbitals of the reduced blue copper site is greatly diminished. Of the three highest energy Met-derived molecular orbitals, the 22a′ Met b_1 oribtal undergoes the greatest interaction with the metal in rBC, but the 7% Cu(I) character in this level (Table 8) is substantially less than the 21% Cu(I) in the corresponding 10a′ Met b_1 MO of $[(CH_3)_2S-CuCl_3]^{2-}$ (Table 3). As a result, the Met b_1 level of the reduced active site is stabilized by only 0.6 eV from the unbound thioether value, much less than the shift observed for the Met b_1 level of the surface complex in Figure 14. The decreased Met b_1 σ overlap in rBC is also reflected in the contour plots, where an additional contour line, representing a 2-fold increase in electron density, is evident in the interatomic region between the Cu(I) ion and the Met sulfur atom of the 10a′ Met b_1 orbital of $[(CH_3)_2S-CuCl_3]^{2-}$ in Figure 13H compared to the 22a′ Met b_1 orbital of rBC in Figure 13L.

The 19a′ Met a_1 orbital of the reduced active site contains only 4% Cu(I) character (Table 8), compared to 13% Cu(I) in the equivalent 7a′ Met a_1 MO of the surface complex (Table 3). Correspondingly, the Met a_1 orbital of rBC is stabilized by only 0.5 eV from the free ligand value, approximately half the stabilization of the surface Met a_1 orbital seen in Figure 14. The contour plot of the 19a′ Met a_1 MO of rBC in Figure 13K illustrates the decreased overlap, revealing less electron density shared in the region of σ overlap between the Cu(I) ion and the Met sulfur relative to the 7a′ Met a_1 level of $[(CH_3)_2S-CuCl_3]^{2-}$ in Figure 13G.

Finally, the 14a″ Met b_2 MO exhibits no Cu(I) mixing in rBC (Table 8), consistent with the 5a″ Met b_2 level of the surface model in Table 3; and no Cu(I) overlap is observed in the contour density plot of the protein Met b_2 orbital, Figure 13J. Despite the absence of Cu(I) mixing in the reduced blue copper site, the Met b_2 orbital is observed 0.3 eV to deeper energy than the unbound thioether b_2 level as a result of the 4% N_2(His) contribution to this MO in the rBC calculation.

For rBC, the only Cu 3d orbital that exhibits any Met mixing is the 26a′ $3d_{z^2}$ orbital (Table 8), oriented σ with respect to the Cu(I)−S(Met) bond, but overlap is minimal even in this orbital, with only 2% S(Met) character.

Importantly, considerable reductions in Cu(I) 4s/4p interactions in the Met b_1 and a_1 orbitals accompany the overall reduction in metal−ligand overlap in rBC compared to the normal bonding scheme in $[(CH_3)_2S-CuCl_3]^{2-}$, indicative of a dramatically weaker Cu(I)−S(Met) bond. Total Cu(I) 4s/4p

mixing is reduced from 9% in the 10a′ Met b_1 level of $[(CH_3)_2S-CuCl_3]^{2-}$ (Table 3) to 4% in the 22a′ Met b_1 level of rBC (Table 8), and from 9% in the 7a′ Met a_1 level of $[(CH_3)_2S-CuCl_3]^{2-}$ (Table 3) to only 2% in the 19a′ Met a_1 level of rBC (Table 8). The electron contours of the Met b_1 and a_1 orbitals of rBC demonstrate that the predominant Cu 4p interaction involves the σ $4p_z$ orbital. Electron populations summed over the Met-derived valence orbitals for the calculations of the unbound ligand, $[(CH_3)_2S-CuCl_3]^{2-}$, and rBC are listed in Table 9, along with the electron shifts that occur upon Met bonding to the two Cu(I) sites. In rBC the Met ligand donates a total of only 0.24 electron, less than half the 0.53 electron donated by Met in $[(CH_3)_2S-CuCl_3]^{2-}$. An SCF-Xα-SW calculation of the reduced blue copper site with a Cu−S(Met) bond length of 2.30 Å reveals that at a normal bond length Met donates 0.71 electron to the Cu(I) ion; therefore, the elongated Cu−S(Met) bond does not derive from the electronic structure of the reduced blue copper site, but is imposed on the site by the tertiary structure of the protein.

In summary, the electronic structure of the Cu(I)−S(Met) bond in reduced blue copper is qualitatively similar to the normal Cu(I)−S(thioether) bond description, consisting predominantly of σ charge transfer from the Met b_1 orbital, and to a lesser extent the Met a_1 orbital, into the unoccupied Cu $4p_z$ orbital. However, at the unusually long 2.82-Å bond length in the protein, the donor strength of the Met ligand is reduced to less than half of the normal Cu(I)−S(Met) bond.

3. Cu(I)−Cysteine. A Cu(I)−S(Cys) bond length of 2.10 Å and a Cu−S−C bond angle of 110° were used in the SCF-Xα-SW electronic structure calculation of rBC. While the 110° Cu−S−C bonding angle is consistent with the angle observed in typical thiolate compoiunds, the 2.10-Å Cu(I)−S(Cys) bond length at the reduced blue copper site is ~0.1 Å shorter than those commonly observed for normal Cu(I)−thiolate species. In the SCF-Xα-SW calculation, the Cu(I)−S(Cys) bond lies approximately in the *xy* plane of the copper. Electron density contour plots of the highest occupied Cys σ, pseudo σ, and π orbitals of rBC are presented in Figure 17, parts J−L, where the active site model, shown in Figure 16I, has been oriented so that the Cys contour diagrams of the reduced blue copper site coincide with the corresponding plots of the $[CH_3S-CuCl_3]^{3-}$ surface model system above (Figure 16F−H).

At the shorter Cu(I)−S(Cys) bond length, the Cu(I) covalency in each of the three Cys valence bonding orbitals is greater than observed in the $[CH_3S-CuCl_3]^{3-}$ model. The Cys π orbital exhibits the greatest increase in Cu(I) covalency relative to the $[CH_3S-CuCl_3]^{3-}$ surface model, with the 19a″ Cys π orbital containing 28% Cu(I) character (Table 8) compared to 22% in the 7a″ Cys π level of the surface bonding description (Table 6). The strong Cu(I) π overlap in the reduced blue copper site can be seen in the electron density contour plots of the Cys π orbitals, in which greater metal−ligand overlap is observed in the Cys π orbital of rBC in Figure 16L relative to the same orbital in the surface model in Figure 16H. It should be noted that the π interaction in rBC involves the $d_{x^2-y^2}$ orbital which is bisected by the Cu−S(Cys) vector. The strongest Cu(I) interactions are found in the 23a′ Cys pseudo-σ orbital which contains 35% Cu(I) character (Table 8). Although the Cu(I) covalency in the blue copper pseudo-σ orbital is approximately equal to the 34% Cu(I) character in the 12a′ Cys pseudo-σ level of the surface complex (Table 6), the electron density contour plot of the pseudo-σ MO of rBC in Figure 16K exhibits greater electron density shared between copper and sulfur than in the $[CH_3S-CuCl_3]^{3-}$ complex in Figure 16G. In the 12a′ Cys pseudo-σ MO of the $[CH_3S-CuCl_3]^{3-}$ surface complex, Figure 16G, 6% chloride character (Table 6) is observed weakly bonding with Cu(I), resulting in the redistribution of electron density away from the Cu(I)−S(Cys) bond. No such non-thiolate ligand contributions are found in the 23a′ Cys pseudo-σ orbital of rBC (Table 6). Finally, the 20a′ Cys σ orbital of the reduced blue copper site contains 18% Cu(I) character (Table 8), a small increase over the 15% Cu(I) in the 12a′ Cys σ level of $[CH_3S-CuCl_3]^{3-}$ (Table 6), resulting in a slight increase in the amount of electron density shared between the metal and the ligand in rBC relative to $[CH_3S-CuCl_3]^{3-}$ (Figure 16J *vs* 16F).

In Figure 17 the orbital energies of the Cys valence levels of rBC do not adequately reflect the increases in Cu(I) covalency in the blue copper Cys levels relative to the $[CH_3S-CuCl_3]^{3-}$ surface complex. However, a significant amount of chloride character is observed in the Cys valence orbitals of the surface complex, whereas no non-thiolate ligand character is found in the corresponding Cys levels of rBC. The Cl-derived levels of $[CH_3S-CuCl_3]^{3-}$ lie energetically between the Cys pseudo-σ and σ orbitals; therefore, chloride contributions destabilize the Cys pseudo-σ and π orbitals and stabilize the Cys σ level in the surface complex, accounting for the observed energy shifts between $[CH_3S-CuCl_3]^{3-}$ and rBC.

From Table 8, considerable S(Cys) covalency is observed in the 21a″ Cu $3d_{x^2-y^2}$ orbital of rBC, which consists of 68% Cu(I), 20% S(Cys), 6% N_2(His) (3% per N_2), and 0% S(Met) character. The 20% S(Cys) represents a substantial increase over the S(thiolate) mixing in the corresponding Cu $3d_{xz}$ orbital of the surface model. Thus, in the reduced blue copper active site the strong Cys π interaction with the Cu(I) is important in determining the orientation and energy of the active site HOMO and, consequently, should have a significant impact on the redox properties and the geometry of blue copper active site as discussed below.

In conjunction with the overall increase in metal−ligand covalency at the shorter Cu(I)−S(Cys) bond of rBC, significant increases in Cu 4s/4p contributions are observed in the Cys valence orbitals, indicating a stronger Cu(I)−S(Cys) bond in rBC. In particular, nearly all of the increased metal covalency in the Cys π orbital is attributed to increased Cu 4p character, which grows from only 1% in the 7a″ Cys π level of $[CH_3S-CuCl_3]$ (Table 6) to 5% Cu 4p in the 19a″ Cys π level of rBC (Table 8). Bonding in the pseudo-σ orbital is moderately strengthened as well, exhibiting a total of 10% Cu 4s/4p character in the 23a′ level of the protein (Table 8) compared to 8% in the 12a′ level of the surface complex (Table 6). Similarly, the Cu 4p character in the Cys σ orbital increases from 3% in the 6a′ level of $[CH_3S-CuCl_3]^{3-}$ (Table 6) to 8% in the 20a′ level of rBC (Table 8). The Cu 4s character observed in the Cys σ orbital, on the other hand, actually decreases from 8% in the $[CH_3S-CuCl_3]^{3-}$ complex to 2% in rBC; however, this decrease is not indicative of a weakened Cu(I)−S(Cys) bond in reduced blue copper, because much of the Cu 4s character in the surface complex is involved in Cu−Cl bonding rather than in the Cu−Cys bonding, as seen in Figure 16F.

To quantitatively evaluate the increased Cu(I)−S(Cys) bond strength in rBC relative to the $[CH_3S-CuCl_3]^{3-}$ complex, the electron occupations summed over the thiolate valence orbitals are presented in Table 9, together with the charges in electron occupation that occur upon Cys bonding to Cu(I) in the $CuCl_3^{2-}$ cluster and in the protein active site model. These shifts reveal that at the shorter Cu(I)−Cys bond length in the protein the thiolate ligand donates 1.40 electrons to the Cu(I) ion, significantly more charge than the 0.84 electron donated by the thiolate

Table 10. Electron Charge Donation[a] *vs* Cys and Met Bond Lengths

		geometry I Met 2.30 Å, Cys 2.20 Å		geometry II Met 2.82 Å, Cys 2.20 Å		geometry III Met 2.82 Å, Cys 2.10 Å	
ligand	unbound Σe^-	Σe^-	Δe^-	Σe^-	Σe^-	Σe^-	Δe^-
NH_3	8.00	7.47	−0.53	7.48	−0.52	7.44	−0.56
Met	20.00	19.35	−0.65	19.48	−0.52	19.76	−0.24
Cys	14.00	12.97	−1.03	13.09	−0.91	12.72	−1.28

[a] Summed over all valence levels.

in the $[CH_3S-CuCl_3]^{3-}$ surface model complex and substantially more charge than is donated by the Met and His ligands of rBC.

In summary, the electronic structure of the Cu(I)−Cys bond at the reduced blue copper active site differs in significant ways from the surface Cu(I)−thiolate bonding description for $[CH_3S-CuCl_3]^{3-}$. In both rBC and the surface model, the Cu(I)−S(Cys) bond is dominated by σ charge transfer from the Cys pseudo-σ orbital to the Cu 4p orbitals; however, a considerably greater π interaction is present in the reduced blue copper active site. The shorter bond length in the protein site strengthens the bonding interactions of each of the Cys valence orbitals, resulting in a Cu(I)−S(Cys) bond approximately 1.5× stronger than a normal Cu(I)−thiolate bond at 2.20 Å.

4. Origin of the Short Cu(I)−S(Cys) Bond. By determining the energy and orientation of the reduced blue copper active site HOMO, the strong π interaction of the shortened Cu(I)−S(Cys) bond at the reduced blue copper active site should profoundly affect the redox properties of blue copper proteins. Therefore, it is of considerable interest to understand the origin of this short Cu(I)−S(Cys) bond. To this end, SCF-Xα-SW calculations have been extended to a C_s(met)−$Cu^I[S(CH_3)_2(SCH_3)(NH_3)_2]$ blue copper model, where the Cu(I)−S(thioether) and Cu(I)−S(thiolate) bond lengths are systematically altered. Since NH_3 has been shown to reasonably model His bonding to Cu(I), the imidazoles in the rBC model have been replaced by ammines at a Cu(I)−N bond length of 2.05 Å to reduce calculation times. The three C_s geometries investigated were as follows: (I) Met and Cys at normal Cu(I) bond lengths of 2.30 and 2.20 Å, respectively; (II) a long Cu(I)−Met bond at 2.82 Å and a normal Cu(I)−Cys bond at 2.20 Å; and (III) a long Cu(I)−Met bond at 2.82 Å and a short Cu(I)−Cys bond at 2.10 Å. The total valence electron occupations summed over each of the ligands at the three cluster geometries are presented in Table 10, along with the differences in electron populations relative to the corresponding free ligand. In all three geometries, the charge donation from the NH_3 ligands remains approximately constant.

In geometry I, using normal Cu(I)−Met and Cu(I)−Cys bond distances, significant charge is shifted to the Cu(I) ion from both the Cys and Met ligands. Cys dominates the charge transfer, donating 1.03 electrons, compared to the 0.65 electron lost by Met. In geometry II, elongation of the Cu(I)−Met bond to 2.82 Å reduces the effective Cu(I)−S(Met) overlap, thereby reducing the efficiency of the Met → Cu(I) charge transfer from 0.65 to 0.52 electron. (Note that the slight decrease in Cys charge donation in geometry II relative to geometry I derives from the larger intersphere volume of geometry II, which results in more charge being repartitioned onto the ligands.) In geometry III, in which the Cu(I)−S(Cys) bond is shortened to 2.10 Å, Met to Cu(I) charge donation is again reduced, to 0.24 electron, but the amount of charge donated by Cys increases significantly to 1.28 electrons. The 2.10-Å Cu(I)−S(Cys) bond is substantially stronger than at 2.20 Å, and dominates the Cu(I) bonding at the reduced blue copper active site. Thus, the unusually long 2.82-Å Cu(I)−S(Met) bond length observed in the blue copper active site results in a significant loss of charge donated to the Cu(I) center. Since the shorter 2.30-Å Cu−Met bond is electronically more favorable than the elongated bond, the protein structure must be responsible for imposing the less favorable, long Cu(I)−S(Met) geometry on the reduced site. The short Cu(I)−Cys bond then serves to compensate for the reduced charge at the Cu(I) center through increased σ and π donor interactions which increase the strength of this bond.

C. Electronic Structure Changes in the Blue Copper Active Site upon Oxidation. In order to establish the electronic structure changes that occur at the blue copper active site upon oxidation, SCF-Xα-SW molecular orbital calculations have also been performed on a $Cu^{II}[S(CH_3)_2(SCH_3)(N_2C_3H_4)_2]^+$ cluster in the oxidized state, employing the same C_s(met) approximation as used for the reduced state. Although electronic structure calculations of the oxidized blue copper active site have been previously reported by this group,[24,27] the results presented here represent a refinement of the prior calculation in several respects. The $Cu^{II}[S(CH_3)_2(SCH_3)(N_2C_3H_4)_2]^+$ cluster (oBC) used in the present study is a more complete model of the blue copper active site since imidazoles, rather than ammines, are used to model the His amino acids, while retaining the axial thioether. Shorter Cu−L bond lengths are used in the current study, taken from a more recent X-ray crystal structure[1] of poplar plastocyanin refined to 1.33 Å (Cu(II)−S(Met) = 2.82 Å; Cu(II)−S(Cys) = 2.07 Å; and Cu(II)−N_2(His) = 1.98 Å, the average of the 2.06-Å and 1.91-Å Cu−N bonds of the crystal structure). The atomic sphere radii used for oBC are consistent with our earlier study, except that a S(Met) radius of 2.20 bohr (*cf.* 2.30 bohr in the previous calculation) was used to match PES experiments, and hydrogen radii of 1.00 bohr were used rather than the value of 1.17 bohr used earlier. Also, in the present calculation of the reduced and oxidized model sites the polarization basis functions have been expanded to $l = 3$ for Cu and $l = 2$ for sulfur and nitrogen. Finally, our present computing capabilities allowed us to consider a calculation converged when the largest change in the potential between successive iterations was less than 10^{-4}. A complete list of atomic coordinates and input values for the calculation of oBC are available as supplementary material.

The SCF-Xα-SW wave functions of the highest occupied molecular orbitals of oBC are presented in Table 11, and the SCF-Xα-SW ground state energies of the highest occupied molecular orbitals of oBC are presented on the right side of Figure 18. The oxidized orbital energies in Figure 18 have been shifted by an additive constant of +0.34 eV to align the 19a′ Met a_1 level of the oBC calculation to the 20a′ Met a_1 level of rBC, since the wave function of this orbital exhibits essentially no change upon oxidation (Tables 8 and 11).

The electronic structure description of the Cu−L bonding at the oxidized blue copper active site is generally consistent with our previously reported results. Both calculations result in a highly covalent Cu $3d_{x^2-y^2}$ active site HOMO, containing ~35% S(Cys) character and ~5% total N_2(His) character. While the 54% Cu character in the HOMO of the present calculation is somewhat greater than the value from our previous study (42%) and the experimental value (38%), the present calculation is appropriate for comparison to the parallel rBC calculation. A larger splitting of the Met valence orbitals in the present calculation indicates that the shorter bond distance and smaller

Table 11. SCF-Xα-SW Results for oBC

			% Cu					% Cys		% Met		% His	
level	orbital label	energy (eV)	Cu[a]	s	p	d	[d orbital breakdown]	S	Cys[b]	S	Met[b]	N_2[c]	His[b]
21a″	Cu $d_{x^2-y^2}$	−3.26	54		1	52	$[0.00d_{xz+yz} + 1.00d_{x^2-y^2}]$	35	3	0	0	6	2
27a′	Cu d_{xy}	−3.85	71	6	7	57	$[0.03d_{z^2} + 0.08d_{xz-yz} + 0.31d_{xy}]$	16	1	3	0	2	7
20a′	His π_1	−4.36	17		0	16	$[0.85d_{xz+yz} + 0.01d_{x^2-y^2}]$	0	0	0	0	9	73
20a″	His π_1	−4.36	17		0	16	$[0.85d_{xz+yz} + 0.01d_{x^2-y^2}]$	0	0	0	0	9	73
25a′	Cu d_{z^2}	−4.52	87	0	3	84	$[0.64d_{z^2} + 0.00d_{xz-yz} + 0.03d_{xy}]$	1	1	6	1	2	1
26a′	His π_1	−4.58	14	1	1	12	$[0.04d_{z^2} + 0.13d_{xz-yz} + 0.58d_{xy}]$	3	0	0	0	5	78
19a″	Cu d_{xz+yz}	−4.68	70		3	66	$[0.77d_{xz+yz} + 0.01d_{x^2-y^2}]$	8	0	0	0	2	19
24a′	Cu d_{xz-yz}	−4.82	83	0	0	83	$[0.00d_{z^2} + 0.61d_{xz-yz} + 0.05d_{xy}]$	3	1	1	0	1	11
18a″	Cys π	−5.20	33		5	45	$[0.18d_{xz+yz} + 0.32d_{x^2-y^2}]$	36	3	0	0	3	4
23a′	Met b_1	−5.74	15	2	2	11	$[0.83d_{z^2} + 0.01d_{xz-yz} + 0.00d_{xy}]$	0	0	72	12	0	0
22a′	Cys pseudo-σ	−6.34	37	2	6	27	$[0.03d_{z^2} + 0.00d_{xz-yz} + 0.64d_{xy}]$	54	6	0	0	2	2
17a″	His π_2	−7.02	8		0	7	$[0.83d_{xz+yz} + 0.01d_{x^2-y^2}]$	0	0	0	0	49	42
21a′	His π_2	−7.17	9	0	1	7	$[0.02d_{z^2} + 0.19d_{xz-yz} + 0.18d_{xy}]$	1	0	2	1	47	40
20a′	Met a_1	−8.34	4	0	2	2	$[0.79d_{z^2} + 0.01d_{xz-yz} + 0.00d_{xy}]$	0	0	61	31	2	1
19a′	Cys σ	−9.25	22	1	9	10	$[0.00d_{z^2} + 0.35d_{xz-yz} + 0.16d_{xy}]$	43	29	0	0	5	1
15a″	His σ	−9.57	23		7	14	$[0.00d_{xz+yz} + 0.96d_{x^2-y^2}]$	0	0	1	2	35	38
15a″	Met b_2	−9.64	1		0	1	$[0.00d_{xz} + 1.00d_{x^2-y^2}]$	0	0	33	61	2	2
18a′	His σ	−10.33	28	15	5	4	$[1.00d_{z^2} + 0.00d_{xz-yz} + 0.00d_{xy}]$	3	5	0	0	42	21

[a] Total charge on the copper ion. [b] Total charge for all atoms of the ligand except the S or N coordinated to Cu. [c] Total charge for the coordinating N_2 atoms.

S(Met) radius results in greater Met interaction with the metal center than presented in our previous calculation; however, as the Cu−Met mixing is small to begin with, the effect of this difference on the overall bonding scheme of the blue copper active site is minimal.

Upon oxidation of the blue copper active site, the increased effective nuclear charge of the Cu(II) ion induces competing effects on the overall covalency of the ligand valence orbitals. From Figure 18, the energies of the Cu 3d orbitals are lowered by an average of ~1.5 eV relative to the reduced state, decreasing the energy difference between the metal 3d orbitals and the ligand valence orbitals and contributing to an overall increase in covalency. On the other hand, the metal orbitals contract upon oxidation, reducing metal−ligand overlap, tending to decrease covalency. In addition to the increased effective nuclear charge of the Cu ion, changes in the geometry of the active site also contribute to changes in covalency of the ligand valence levels by increasing specific metal−ligand overlap interactions. Increased mixing of the filled Cu d levels into the ligand orbitals does not contribute to Cu−L bonding; only the mixing of the unoccupied Cu 4s/4p orbitals and the newly half-occupied Cu $3d_{x^2-y^2}$ orbital with the filled ligand levels contributes to the strength of the individual Cu−L bonds and the stabilization of the oxidized active site. The changes in electronic structure of each Cu−L bond upon oxidation of the blue copper active site are described below.

1. Cu(II)−Histidine. The average Cu−N(His) bond length of oxidized poplar plastocyanin[1,73,74] is 0.07 Å shorter than the average bond length of the reduced active site.[75] In oBC the Cu mixing is greater in the His π_1, π_2, and σ orbitals than in the corresponding orbitals of rBC, indicating that upon oxidation the reduced energy difference between the metal and ligand levels and the increased overlap from the shortened bond overcome the contraction of the metal orbitals. In the His π_1 orbitals, the Cu character increases from an average of 5% in the 18a″/24a′ levels (Table 8) to over 15% in the 20a″/26a′ orbitals of the oxidized active site (Table 11), with nearly all of the increase occurring as enhanced Cu 3d interaction. From Figure 18, the increase in Cu mixing leads to only a 0.2-eV stabilization because the 3d manifold of oBC is lowered in energy to the extent that the $3d_{z^2}$, $3d_{xz+yz}$, and $3d_{xz-yz}$ mixing in the His π_1 orbital is antibonding, counteracting much of the stabilization arising from mixing of higher energy metal orbitals. Note that, as described in Section IV.A, the His π levels are too high in energy due to intersphere effects that result in the π_1 level being approximately equal to the Cu 3d manifold. From a comparison of the experimental gas-phase energies to the calculated His π energies, the π_1 level in Figure 18 should be ~2 eV deeper in energy and the π_2 level should be ~1 eV deeper. The Cu character in the His π_2 orbitals also increases upon oxidation, from an average of 4% in the 17a″/21a′ orbitals of rBC (Table 8) to an average of 8% in the corresponding 17a″/21a′ levels of oBC (Table 11), where, again, an increased Cu 3d contribution accounts for nearly all the increase in covalency. The greater Cu character is reflected in Figure 18 as a 0.31-eV stabilization of the His π_2 levels of oBC relative to the same levels of rBC. The His σ orbitals, which contain the greatest amount of Cu character, exhibit practically no increase in covalency upon oxidation, from an average of 24% in the 16a″/18a″ orbitals of rBC (Table 8) to 25% in the 16a″/18a′ levels of oBC (Table 11). Since the amount of Cu character in the His σ orbitals remains largely unchanged upon oxidation, the 0.9-eV stabilization of these levels relative to the reduced site must arise as the result of the increased contributions from Cys, Met, and the imidazole ring atoms observed in the His σ molecular orbitals of oBC (Table 11 *vs* 8).

From Table 9, the amount of charge donated by the His ligand to the Cu ion increases from 0.38 to 0.67 electron upon oxidation of the blue copper active site, indicating a stronger Cu−His bond in oBC. No increase is observed in the Cu 4s/4p mixing in any of the His valence levels of oBC (Table 11) relative to the corresponding orbitals of rBC (Table 8); therefore, the increased His donor strength is entirely due to overlap of the 21a″ Cu $3d_{x^2-y^2}$ HOMO, which becomes half-occupied in the oxidized state. The only His valence orbital of oBC that exhibits any significant Cu $3d_{x^2-y^2}$ mixing is the 16a″ His σ orbital, which contains 14% Cu $3d_{x^2-y^2}$ character.

2. Cu(II)−Methionine. Upon oxidation of the blue copper active site, the Cu(I)−Met bond length remains constant at 2.82 Å, and the small amount of Cu−Met interaction observed in rBC is mirrored in oBC. No change in the amount of Cu

(73) Scott, R. A.; Hahn, J. E.; Doniach, S.; Freeman, H. C.; Hodgson, K. O. *J. Am. Chem. Soc.* **1982**, *104*, 5364−9.
(74) Murphy, L. M.; Hasnain, S. S.; Strange, R. W.; Harvey, I.; Ingledew, W. J. In *X-ray Absorption Fine Structure*; Hasnain, S. S., Ed.; Chichester: Ellis Harwood: 1990; pp 152−4.
(75) Tullius, T. D. Ph.D. Thesis, Stanford University, 1979.

character is seen in the lower energy b_2 and a_1 Met valence levels, suggesting that the deeper energy of the Cu(II) 3d manifold is offset by the reduced overlap due to metal orbital contraction upon oxidation. From Tables 8 (rBC) and 11 (oBC), the 14a″ Met b_2 level of rBC and the 15a″ Met b_2 level of oBC both contain <1% Cu, while the 19a′ Met a_1 orbital of rBC and the 20a′ Met a_1 orbital of oBC both contain 4% Cu character. Consequently, no significant stabilization of these Met valence levels is observed in Figure 18. The Cu mixing in the Met b_1 orbital, on the other hand, increases from 7% in the 22a′ level of rBC (Table 8) to 15% in the 23a′ level of oBC (Table 11), with all of the increased covalency due to enhanced Cu 3d interaction. Upon oxidation the Met b_1 stabilization from increased Cu mixing is countered to some extent, however, by the loss of Cys pseudo-σ mixing in this MO which in rBC contributes to the stabilization of the Met b_1 level.

No change in Cu 4s/4p mixing is observed in the b_2, a_1, or b_1 Met valence orbitals upon oxidation, nor is any significant Cu $3d_{x^2-y^2}$ character found in any of the Met valence orbitals since this ligand is oriented approximately along the z axis of the active site. Furthermore, the total electron occupancy of the Met ligand remains virtually unchanged (Table 9), rising only slightly from 0.24 electron in the reduced state to 0.28 electron in oBC. Thus, no significant change in the electronic structure of the Cu−Met bond accompanies the oxidation of the blue copper active site.

3. Cu(II)−Cysteine. The short 2.10-Å Cu(I)−Cys bond of the reduced blue copper active site is shortened further to 2.07 Å upon oxidation. Similar to the Cu−His description above, greater Cu mixing is observed in the three highest occupied Cys valence orbitals of oBC relative to rBC. Moderate increases in Cu character are observed in the Cys σ and pseudo-σ orbitals. From Tables 8 and 11, Cu mixing in the Cys σ orbital increases from 18% in the 20a′ level of rBC to 22% in the 19a′ level of oBC, and in the Cys pseudo-σ orbital from 35% in the 23a′ level (Table 8) to 37% in the 22a′ level (Table 11). The most dramatic change in the Cys valence levels, however, occurs in the Cys π orbital, where a substantial increase in Cu character is observed, from 28% in the 19a″ level of rBC (Table 8) to 35% in the 18a″ level of oBC (Table 11), with gains in Cu 3d mixing accounting for all of the increased covalency. The greater Cu mixing in the Cys valence levels of oBC is reflected in Figure 18, where the Cys π, pseudo-σ, and σ orbitals are all stabilized by ~1.1 eV upon oxidation of the reduced site. The fact that the Cys π level is not stabilized more relative to the energy shifts of the pseudo-σ and σ orbitals, despite the greater increase in Cu mixing, derives from the antibonding 12% Cu $3d_{xz+yz}$ mixing in this MO, which to some extent offsets the stabilization of the Cys π orbital due to $3d_{x^2-y^2}$ mixing. The antibonding Cu $3d_{xz+yz}$ interaction does not affect the overall Cu−Cys bonding, however, as both the Cys π and Cu $3d_{xz+yz}$ orbitals are filled levels.

The electron occupations summed over the Cys valence levels of rBC and oBC in Table 9 indicate that the thiolate ligand donates 1.93 electrons to the Cu(II) ion, considerably more charge than the 1.40 electrons donated by Cys in rBC, indicating a significantly stronger Cu−Cys bond in the oxidized site. The strengthened bond cannot be attributed to increased Cu 4s/4p interactions since the mixing of these orbitals in the filled Cys π, pseudo-σ, and σ levels remains approximately unchanged upon oxidation. The stronger donor interaction arises entirely from the half-occupied Cu $3d_{x^2-y^2}$ mixing in the Cys π orbital. The 26% Cu $3d_{x^2-y^2}$ character in the Cys π orbital of oBC (Table 11) represents a significant increase from the 18% observed in rBC (Table 8), providing further evidence of a much stronger Cu−Cys π interaction. The dominant Cys bonding observed in the Cu $3d_{x^2-y^2}$ orbital is consistent with the fact that the His σ orbitals show no increase in Cu $3d_{x^2-y^2}$ mixing upon oxidation, even at the shorter bond length of the oxidized site. The increased bonding contribution from the Cys π donor interaction is also reflected in the charge distribution of the Cu $3d_{x^2-y^2}$ HOMO of oBC, which increases from 20% to 36% S(Cys) character upon oxidation.

In summary, the long axial Cu−Met bond does not undergo any significant geometric or electronic structure change upon oxidation of the reduced blue copper active site. No increase in Cu 4s/4p mixing is observed, and no Cu $3d_{x^2-y^2}$ character is found in the Met valence orbitals, indicating that no change occurs in the Met ligand donor interaction. The Cu−His bond is strengthened somewhat by the half-occupied Cu $3d_{x^2-y^2}$ contributions in the His σ orbitals, but the mixing of the HOMO in the ligand valence levels does not increase upon oxidation of the active site. The most important Cu bonding changes upon oxidation involve the Cys ligand. Strong overlap of the Cu $3d_{x^2-y^2}$ orbital in the Cys π level of the reduced site is further increased upon oxidation; and, being half-occupied in the oxidized site, the substantial mixing of the HOMO contributes significantly to the strengthening of the Cu−Cys bond. The strengthening of the Cu−Cys π bond upon oxidation and the resulting stabilization of the oxidized active site should have important implications in determining the redox properties of the blue copper proteins as discussed below.

D. Electronic Structure Contributions to Reduction Potentials. Reduction potentials ($E°$) have been measured for a wide range of blue copper proteins. In general, these potentials are quite positive, favoring the reduced Cu(I) oxidation state, ranging from a low of 180 mV for stellacyanin[76] to a high of 780 mV for fungal laccase,[77,78] with the plastocyanins exhibiting potentials of ~380 mV.[50,79,80] Having developed an electronic structure description of the reduced and oxidized blue copper sites, we have undertaken an investigation of the electronic structure contributions to the reduction potential of this center in plastocyanin. Starting with a pseudotetrahedral $Cu(NH_3)_4^+$ model, the effects on the ionization energy of ammine substitution with imidazole, thioether, and thiolate are investigated to systematically build a blue copper active model. While it is recognized that many factors contribute to protein reduction potentials,[81,82] including the dielectric effects of the surrounding medium, specific hydrogen bonding, and entropy terms,[83] the aim of this study is to focus on and evaluate the electronic contributions to the potential.

The pseudotetrahedral $Cu(NH_3)_4^+$ model used for this study is based on the bis[2,2′-bis(2-imidazolyl)biphenyl]copper complex reported by Schugar *et al.*[49] Bond lengths and bond angles for the $Cu(NH_3)_4^+$ cluster were taken from the X-ray crystal structure of the reduced Schugar complex: Cu(I)−N = 2.05 Å, ∠N−Cu(I)−N′ = 120°. The Schugar model provides an excellent starting point for this study for several reasons. The

(76) Peisach, J.; Levine, W. G.; Blumberg, W. E. *J. Biol. Chem.* **1967**, *242*, 2847−58.
(77) Malmström, B. G. In *New Trends in Bio-inorganic Chemistry*; Williams, R. J. P., DaSilva, R. J. R. F., Eds.; Academic Press: London, 1978; pp 59−78.
(78) Reinhammar, B. R. M. *Biochim. Biophys. Acta* **1972**, *275*, 245−59.
(79) Büchi, F. N.; Bond, A. M.; Codd, R.; Huq, L. N.; Freeman, H. C. *Inorg. Chem.* **1992**, *31*, 5007−14.
(80) Armstrong, F. A.; Butt, J. N.; Govindaraju, K.; McGinnis, J.; Powls, R.; Sykes, A. G. *Inorg. Chem.* **1990**, *29*,
(81) Marcus, R. A.; Sutin, N. *Biochim. Biophys. Acta* **1985**, *811*, 265−322.
(82) Gray, H. B. *Chem. Soc. Rev.* **1986**, *15*, 17−30.
(83) Richardson, D. *Inorg. Chem.* **1990**, *29*, 3213−7.

pseudotetrahedral CuN_4 structure is a useful first-approximation of the blue copper active site geometry, and X-ray crystallography indicates that upon oxidation the Cu coordination number is conserved[84] and the geometric changes about the metal are limited due to the sterically constraining bidentate ligands of the complex. Most unconstrained Cu complexes exhibit larger distortions upon oxidation, from a tetrahedral Cu(I) environment toward a square-planar Cu(II) geometry. These geometry changes stabilize the Cu(II) site, reduce the adiabatic ionization energy, and thus lower the reduction potential. By comparing the experimental reduction potential of the constrained Schugar complex[49] ($E°$ = 360 mV) to the reduction potentials of less-constrained CuN_4 systems[85,86] ($E° \approx -200$ mV), an estimate of ~600 mV can be made for the geometric contribution to the reduction potential deriving from the restriction of the structural change that occurs on oxidation.

Using the Slater transition state formalism, ionization energies (IE) have been calculated for the CuN_4 model and for a series of CuN_3L and CuN_2LL' clusters where L = imidazole, methyl thioether, or methanethiolate. These ionization energies have been used to estimate reduction potentials[83,87-90] by considering the reduction potential as

$$E° = -\mathrm{IE} + U + (0.6\ \mathrm{V} - 4.5\ \mathrm{V}) \qquad (1)$$

where 0.6 V is the estimated geometry contribution, −4.5 V is an additive constant to convert the potential to the standard normal hydrogen electrode (NHE) scale, and U is a solvation term to account for the reorganization of the solvent upon reduction. If the radii of the reduced and oxidized complexes are nearly equal, *e.g.* in the Schugar complex and in the blue copper site where little geometry change occurs upon oxidation, the difference in solvation energy between the two oxidation states can be approximated using the Born equation,

$$U = -\frac{e^2}{2r_0}\left(\frac{\epsilon - 1}{\epsilon}\right) \qquad (2)$$

where U is the energy associated with transferring a charge from a conducting sphere in a vacuum to a sphere of equal radius in a dielectric medium, e is the charge (e^2 = 14.4 eV Å for a unit charge), r is the radius of the sphere in angstroms, and ϵ is the dielectric constant of the solvent. Thus, for a one-electron reduction in a protein/water environment ($\epsilon \approx 10$), the differential solvation term reduces to $-6.5/r_0$ eV, where r_0 is assumed to be the radius of the cluster used in the calculation of the ionization energy.[91] The calculated ionization energies and reduction potentials of CuN_4, CuN_3L, and CuN_2LL' are presented graphically in Figure 19, with complexes favoring the reduced Cu(I) state nearer the upper right corner, and those favoring the oxidized Cu(II) state toward the lower left corner. It is important to realize that the reduction potentials in Figure 19 are only crude estimates since the spherical cavity used to determine U does not adequately reflect the actual protein active site environment,[88] but the reduction potentials do exhibit the same trends as the ionization energies, and thus reflect the differences in electronic contributions in each model cluster.

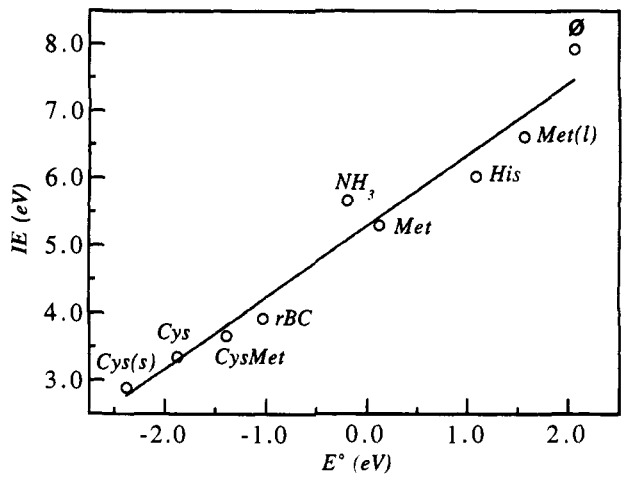

Figure 19. Calculated ionization energy *vs* reduction potential: CuN_3L clusters, where L = open coordination site (Ø), NH_3 at 2.05 Å, His at 2.05 Å, Met at 2.30 and 2.82 Å (*l*), Cys at 2.20 and 2.10 Å (*s*); CuN_2LL', where L = Cys at 2.10 Å and L′ = Met at 2.82 Å; and rBC.

Starting with the CuN_4 (L = NH_3) cluster as a reference, an upper limit to the reduction potential is reached with the removal of one ammine to form the three coordinate CuN_3 species (L = Ø in Figure 19), consistent with the fact that a lower coordination number favors the reduced Cu(I) oxidation state. Substitution of ammine with thioether or imidazole (L = Met, His) results in potentials close to the value of the tetraammine. Imidazole substitution increases the ionization energy relative to ammine, reflecting the fact that imidazole is a somewhat poorer charge donor, providing less stabilization of the higher Cu(II) oxidation state. Replacing an ammine with the negatively charged thiolate (L = Cys) at 2.2 Å dramatically decreases the ionization energy due to the strong charge donor ability of the thiolate anion which provides substantial stabilization of the Cu(II) site and significantly lowers the reduction potential.

As described earlier, in the reduced blue copper active site the Met ligand is held at an exceptionally long distance from the Cu ion. In Figure 19, at 2.8 Å the long Cu−Met bond length (L = Met(*l*)) shifts the potential significantly to more positive values as the interaction between the thioether and the metal ion is dramatically reduced, and this cluster approaches the CuN_3 limit (L = Ø). From Section IV.B, the resulting charge reduction at the Cu ion from the elongation of the Cu−Met bond results in a shortening of the Cu−Cys bond. Shortening the Cu−Cys bond in the CuN_3Cys cluster in Figure 19 (L = Cys(*s*)) lowers the potential below the predicted value for CuN_3-Cys at 2.2 Å, as the Cu−Cys bond is strengthened through increased ligand charge donation into the half-occupied Cu(II) $3d_{x^2-y^2}$ HOMO, further stabilizing the oxidized site. Combining the effects of the long Met and short Cys bonds, the CuN_2-CysMet cluster exhibits a potential intermediate between those of the CuN_3Cys and the CuN_3Met clusters. Finally, replacing the two remaining ammines of the $CuN_2CysMet$ cluster with imidazoles to create the rBC model shifts the reduction potential slightly higher, consistent with the single His substitution above. Thus, at normal Cu−Met bond lengths, the blue copper site would be expected to have a much lower reduction potential as

(84) Goodwin, J. A.; Bodager, G. A.; Wilson, L. J.; Stanbury, D. M.; Scheidt, W. R. *Inorg. Chem.* **1989**, *28*, 35−42.
(85) Nikles, D. E.; Powers, M. J.; Urbach, F. L. *Inorg. Chem.* **1983**, *22*, 3210−7.
(86) Patterson, G. S.; Holm, R. H. *Bioinorg. Chem.* **1975**, *4*, 257−75.
(87) Bair, R. A.; Goddard, W. A. I. *J. Am. Chem. Soc.* **1978**, *100*, 5669−76.
(88) Noodleman, L.; Baerends, J. B. *J. Am. Chem. Soc.* **1984**, *106*, 2316−27.
(89) Bursten, B. E.; Green, M. R. *Prog. Inorg. Chem.* **1988**, *36*, 393−485.
(90) Lichtenberger, D. L.; Kellog, G. E.; Landis, G. H. *J. Chem. Phys.* **1985**, *83*, 2759−68.
(91) The radii used to calculate U values are likely all too small relative to the cavity of the actual protein; however, the radius of the tetraammine is especially underestimated due to dielectric saturation that results from H-bonding between the ligands and the solvating molecules. A larger radius compensating for this effect would yield a more positive reduction potential for this complex. See: Brunschwig, B. S.; Stanton, E.; Sutin, N. *J. Phys. Chem.* **1986**, *90*, 3657−68.

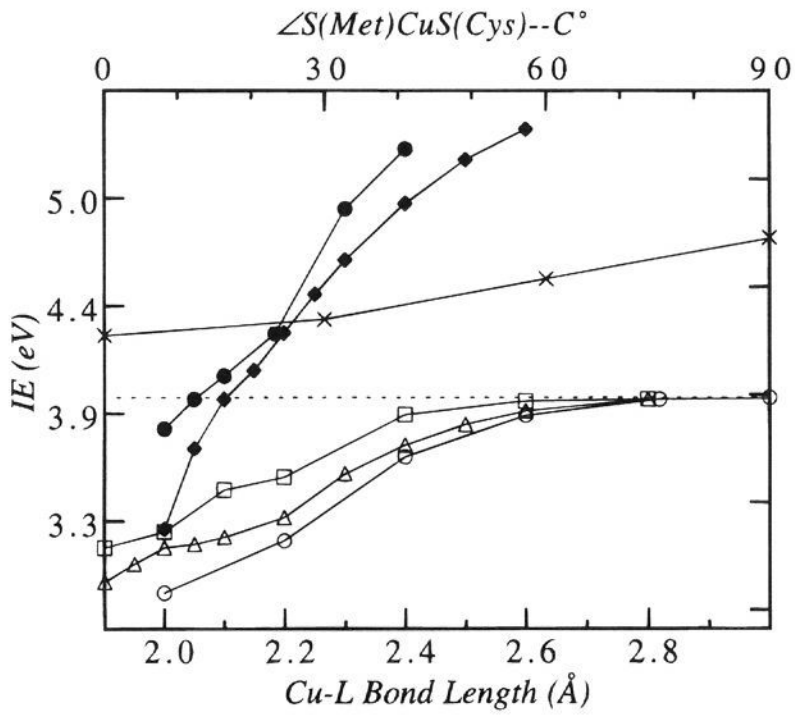

Figure 20. Effects on the rBC calculated ionization energy of the S(Met)CuS(Cys)- - C dihedral angle (×) (top axis) and the Cu−L bond lengths (bottom axis): L = (●) equatorial His, (♦) equatorial Cys, (○) axial Met, (□) axial H_2O, (△) axial His.

the thiolate anion greatly stabilizes the Cu(II) site; and, therefore, the weak bonding of the elongated Cu−Met bond is a key electronic factor in determining the high potentials of the blue copper proteins.

Considering the range of $E°$ values observed for different blue copper sites, it is of interest to elucidate the general effects on ionization energies of changing the structure of the plastocyanin active site on the potentials; therefore, ionization energies have been calculated for a series of rBC geometries, where bond lengths and the S(Met)CuS(Cys) - - C dihedral angle have been systematically varied. The resulting ionization energies are presented in Figure 20. Because of the large number of calculations required for this study, ammine was used to model the His amino acid. From Figure 20, rotation about the Cu−S(Cys) bond to vary the dihedral S(Met)CuS(Cys) - - C angle, has little effect on the IE of the cluster. While the long Met bond is found to greatly raise the reduction potential, variations in the bond length at the long axial distances found in the blue copper sites have little effect on IE due to the very limited overlap of this ligand with the redox active Cu $3d_{x^2-y^2}$ HOMO. Furthermore, replacing the axial Met with water or His has little effect on the ionization energy at long distances from the Cu ion, but would lower the potential at shorter bond lengths. Also, shorter equatorial bond lengths may arise to compensate for a long axial bond partially offsetting the dramatically raised reduction potential.

We have estimated the individual ligand electronic structure contributions to the reduction potential of the blue copper active. Relative to ammine, His ligation in the CuN_4 cluster shifts the potential to slightly higher values due to the somewhat weaker charge donor strength of His; substitution of an ammine with Cys at 2.10 Å drives $E°$ to substantially lower values; and, substitution of ammine by Met at 2.82 Å contributes a dramatic positive shift in $E°$. Therefore, the long Cu−Met bond is of fundamental importance in determining the high potential of the blue copper active site by reducing the charge donated to the Cu(II) ion at the long distance, and thus destabilizing the oxidized site.

E. Electronic Structure Contributions to Geometry. As noted earlier, four-coordinate Cu(I) complexes typically undergo substantial geometric changes upon oxidation, distorting from an approximate tetrahedral geometry in the reduced state toward

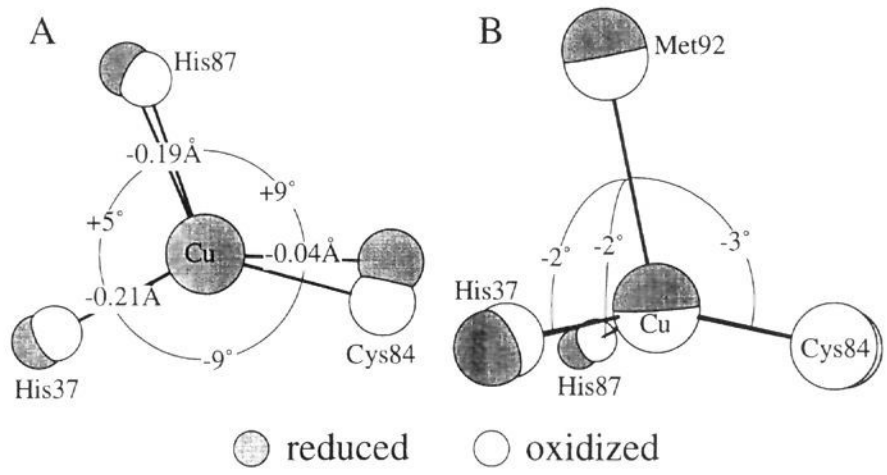

Figure 21. Geometry changes of the blue copper active site upon oxidation (shaded circles = reduced; empty circles = oxidized): (A) in the bond lengths and angles in the NNS equatorial plane with the axial Met removed, and (B) in the S(Met)CuL angles.

a D_{4h} square-planar Cu(II) structure. The origin of the structural change derives in part from the fact that a T_d Cu(II) site would have a triply degenerate $^2T_2$ ground state, leading to a Jahn−Teller distortion. The possible distorting modes of the $^2T_2$ ground state are given by the symmetric direct product $[T_2 \times T_2] = a_1 + e + t_2$, so that a Jahn−Teller distorting force may arise along the e and t_2 normal modes of vibration. In most cases, distortions along the e-symmetry D_{2d} bending mode are observed, flattening the system toward a square-planar structure. In addition, the higher effective nuclear charge of the Cu(II) ion induces a shortening of the metal−ligand bonds, corresponding to a distortion along the a_1 mode. The reduced blue copper site is exceptional, however, in that it distorts relatively little upon oxidation compared to the changes that occur in normal copper compounds, resulting in a low Franck−Condon barrier to redox and allowing a rapid rate of electron transfer.

The crystallographically determined structural changes that occur upon oxidation of the blue copper site in poplar plastocyanin are illustrated in Figure 21.[1,92] The short Cu−Cys bond contracts by 0.04 Å and the Cu−His bond lengths both decrease by approximately 0.2 Å (an average Cu−N(His) bond contraction of 0.07 Å is observed[73−75] from EXAFS). Additionally, the three equatorial ligands shift slightly toward the axial Met ligand upon oxidation so that the Cu ion is more nearly in the NNS(Cys) plane, and the Cys ligand moves in the NNS plane toward His37. Both the longer average Cu−His bond—relative to EXAFS experiments—and the rotation of the Cu−Cys bond in the NNS equatorial plane that are observed in the crystal structure of plastocyanin may be artifacts of the pH effect observed in reduced plastocyanin, which results in the protonation and dissociation of His87 in acidic conditions. The crystal structures of reduced and oxidized *A.d.* azurin exhibit no such equatorial bond angle distortion and a much smaller decrease in the Cu−His bond lengths (0.05 Å).[7]

The geometry differences between the reduced and oxidized blue copper sites arise as a result of the electronic structure changes that occur upon oxidation. The electronic structure changes lead to driving forces toward distortion of the complex relative to the reduced structure along the normal modes of vibration of the molecule. An entatic or rack state of the protein would oppose these electronic forces and limit the distortion of the molecule. We have used the electronic structural changes of the blue copper site upon oxidation as described in Section IV.C to elucidate the geometric distortions that the plastocyanin active site would undergo in an unconstrained environment, *i.e.* in the absence of an entatic or rack state. Starting with the reduced active site structure, SCF-Xα-SW Slater transition state

(92) Guss, J. M.; Freeman, H. C. *J. Mol. Biol.* **1986**, *192*, 361.

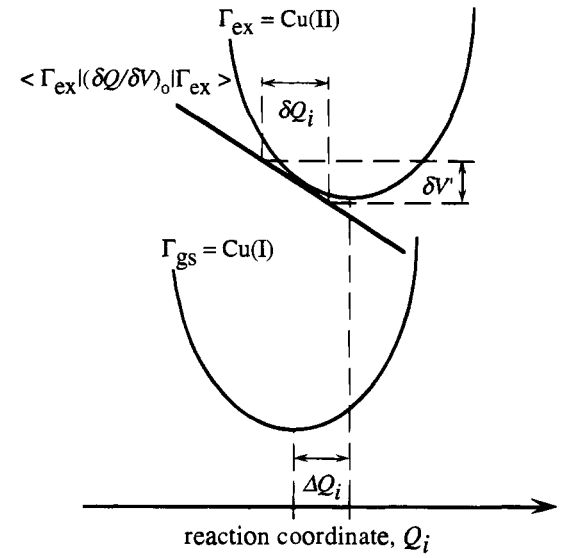

Figure 22. Configuration coordinate diagram of the linear coupling term for the distorting force along the *i*th normal mode of vibration on the oxidized Cu(II) blue copper site relative to the reduced Cu(I) ground state. δV is the energy change calculated for a distortion δQ_i of the molecule. ΔQ_i is the expected distortion along the normal mode for the calculated linear coupling term.

ionization energies have been used to determine the relative distorting forces in the oxidized excited state along all of the normal vibrational modes (Q_i) of the blue copper site. Figure 22 illustrates that the distorting force along the *i*th normal mode Q_i associated with an electronic excited state Γ_{ex} is given by a non-zero slope of a linear coupling term evaluated along a given vibrational mode, $\langle\Gamma_{ex}|(\delta V/\delta Q_i)_0|\Gamma_{ex}\rangle$, where the excited state Γ_{ex} in this analysis is the oxidized Cu(II) site, V is the ligand field potential, and $(\delta V/\delta Q_i)_0$ indicates that the slope is evaluated at the reduced ground state geometry.[93,94] Since the reduced active site structure is known, the linear coupling terms of the oxidized state relative to the reduced state can be determined by the transition state ionization energies of the molecule distorted slightly from the reduced equilibrium geometry in both directions of the normal mode of vibration. It follows then that an entatic or rack state corresponds to a non-zero slope for a linear coupling term in a direction for which the molecule does *not* distort.

A normal coordinate analysis was performed on a C_s trigonal-pyramidal CuN_2S model of the reduced blue copper active site. The ligands were treated as point masses corresponding to the total masses of CH_3S (47 amu) and imidazole (67 amu) and were positioned such that the Cu ion and the Cys sulfur were contained in the C_s mirror plane bisecting the two His nitrogens. Due to the large number of SCF-Xα-SW electronic structure calculations required to determine the slopes for the linear coupling terms along all the normal modes, the Met ligand was eliminated from the model. This approximation is considered reasonable since the Met bonding to Cu(I) was found in Section IV.A to be weak, and the removal of the axial ligand does not alter the C_s symmetry of the site. The six normal modes of vibration resulting from this analysis are depicted on the left side of Table 12. Mixing of bends and stretches was found to be negligible in this simple approximation to the blue copper site, and therefore, each normal mode was treated as a pure stretch or bend. The SCF-Xα-SW Slater transition state ionization energies were calculated for a reduced, equilibrium structure of CuN_2S based on the rBC geometry, and for this CuN_2S model distorted slightly in both the positive and negative directions along each normal mode. The resulting energy changes (δV) for distortions along each normal mode are listed in Table 12 along with the $\delta V/\delta Q_i$ values, where δQ_i is the distortion imposed on the molecule for the analysis. The normal modes are pictured in Table 12 in the direction the molecule would distort as predicted by $\delta V/\delta Q_i$, defined as the positive distortion.

The calculated $\delta V/\delta Q_i$ values in Table 12 indicate that the largest driving forces are found in the stretching modes, especially in the symmetric 1a′ and 3a′ modes which exhibit slopes of 4.35 and 3.28 eV/Å, respectively. The $\delta V/\delta Q_i$ values of the bending modes are approximately a factor of 10^{-3} smaller, with the 6a′ bend exhibiting the dominant bending force. Estimates of the distortions along the normal modes can be obtained using approximate force constants and frequencies for each normal mode of vibration. The frequencies ν (cm^{-1}) of the normal modes listed in Table 12 represent reasonable estimates of the experimental vibrational frequencies[95-97] observed for plastocyanin and Cu(II)–His complexes.[98] The force constant for each normal mode was determined from the frequency and the molal reduced mass (μ_i) as $k_i = 4\pi^2c^2\mu_i\nu_i^2$. The expected distortion along each mode ΔQ_i was then determined as $\Delta Q_i = k_i^{-1}\langle\Gamma_{ex}|(\delta V/\delta Q_i)_0|\Gamma_{ex}\rangle$, and the change in each internal coordinate (ΔR) defining the normal mode was obtained from the expression $\Delta Q_i = (\sum_n l_{in}^2)^{-1/2}(l_{i1}\Delta R_1 + l_{i2}\Delta R_2 + \ldots + l_{in}\Delta R_n)$. From Table 12, the 1a′ normal mode exhibits the largest $\delta V/\delta Q_i$, but the predicted distortion along this mode ($\Delta Q_i = 0.25$ Å) is less than half that predicted for the 3a′ mode ($\Delta Q_i = 0.56$ Å). The 1a′ mode is composed primarily of the Cu–Cys stretch; therefore, the higher force constant associated with the short Cu–Cys bond relative to the Cu–His bond limits the distortion of the molecule in this direction.

Summing the internal coordinate changes along each normal mode leads to a prediction of the total distortion of the molecule. According to this model, upon oxidation of the reduced blue copper site the Cu–S(Cys) bond should contact by ~0.37 Å, the Cu–His bonds would both contract by ~0.29 Å, and the only bond angle changes would be observed along the 6a′ bending mode, reducing the angle between each of the equatorial ligands and the axial Met ligand. These predicted distortions derive from the changes in electronic structure on oxidation of the blue copper site described in Section IV.C. The Cu–Cys bond contracts due to the increased Cys π bonding interaction with the redox active Cu $d_{x^2-y^2}$ orbital, and the His bonds contract as a result of the increased σ bonding with the HOMO. The angular distortions are predominantly along the 6a′ vibrational mode as this mode moves the equatorial ligands toward the Cu xy plane, resulting in better overlap with the Cu $d_{x^2-y^2}$ orbital. On the basis of the electronic structure and the calculated $\delta V/\delta Q_i$ values, the predicted geometry change of the reduced blue copper site upon oxidation is in general agreement with the experimentally observed distortions shown in Figure 21. The Cu–Cys bond contraction is exaggerated in this analysis as a result of the neglect of anharmonicity in the potential energy surface. The anharmonicity should be rather

(93) Wilson, R. B.; Solomon, E. I. *Inorg. Chem.* **1978**, *17*, 1729–36.
(94) Wilson, R. B.; Solomon, E. I. *J. Am. Chem. Soc.* **1980**, *102*, 4085–95.
(95) Thamann, T. J.; Frank, P.; Willis, L. J.; Loehr, T. M. *Proc. Natl. Acad. Sci. U.S.A.* **1982**, *79*, 6396–400.
(96) Loehr, T. M.; Sanders-Loehr, J. In *Copper Proteins Copper Enzymes*; CRC: Boca Raton, FL: 1984; pp 115–55.
(97) Nestor, L.; Larrabee, J. A.; Woolery, G.; Reinhammer, B.; Spiro, T. G. *Biochem. J.* **1984**, *23*, 1084–93.
(98) The frequencies of the bending modes may be somewhat lower in energy than expected; however, attempts to increase these frequencies led to poorer energies of the stretches without significantly varying the descriptions of the normal modes.

Table 12. Normal Coordinate Analysis of a CuNNS Model

normal modes stretches[a]		δV (eV)	δQ_i [b] (Å)	$\delta V/\delta Q_i$ (eV/Å)	ν_i [c] (cm^{-1})	μ_i (amu)	k_i (md/Å)	ΔQ_i (Å)	ΔR (Å) ΔCu-S	ΔCu-N
	1a' (+)	-3.209	.052	4.35	400	29.96	2.21	0.248	-0.204	+0.078
	(−)	-3.435								
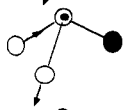	2a" (+)	-3.323	.023	0.17	275	34.38	1.52	0.018	0.000	±0.012
	(−)	-3.327								
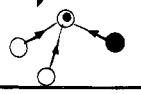	3a' (+)	-3.244	.051	3.28	220	33.00	0.94	0.560	-0.169	-0.365
	(−)	-3.408								
normal modes bends[a]		δV (eV)	δQ_i [b] (°)	$\delta V/\delta Q_i$ (10^{-3} eV/°)	ν_i [c] (cm^{-1})	μ_i (amu)	k_i (md/Å)	ΔQ_i (°)	ΔR° ΔSCuN	ΔNCuN
	4a" (+)	-3.330	5.0°	0.60	70	49.74	0.14	0.118°	±0.083	0.000
	(−)	-3.329								
	5a' (+)	-3.327	8.1°	0.49	60	56.40	0.13	0.106°	+0.052	-0.075
	(−)	-3.331								
	6a' (+)	-3.312	8.1°	4.45	40	56.08	0.05	2.657°	+1.344	+1.854
	(−)	-3.348								

◉ Cu ○ His ● Cys

[a] Pictured distortion corresponds to the direction predicted by the slope of $\delta V/\delta Q_i$ and is assigned as the (+) direction. [b] Total distortion along each mode used to calculate $\delta V/\delta Q_i$. [c] Estimated from Raman spectra of blue copper.

significant for the short, strong Cu−Cys bond, causing the energy of the Cu(II) site to rapidly increase upon contraction of this bond.

Thus, the results summarized in Table 12 indicate that the limited distortion of the reduced blue copper site which occurs upon oxidation is to be expected for this structure; and, therefore, no high-energy geometric conformation is imposed upon the Cu(II) site by an entatic or rack state of the protein. The absence of a strong distorting force upon oxidation of the reduced blue copper site can be understood based upon the following model. As indicated above, starting in a high-symmetry T_d limit, the Cu(II) ion is in a $^2T_2$ ground state which gives rise to two possible Jahn−Teller active distorting modes, e and t_2. The e mode involves the D_{2d} distortion toward a square-planar geometry and the t_2 mode involves a C_{3v} distortion arising from the elongation of one bond. The C_{3v} distortion associated with the t_2 vibrational mode is already imposed on the reduced blue copper site by the elongated Cu−Met bond, trapping the oxidized site in a Jahn−Teller energy minimum. It is therefore the *reduced* site, with the long Cu−Met bond as described in Section IV.B, that should be considered as being in an entatic or rack state, effectively lowering the symmetry from a tetrahedral to an elongated C_{3v} geometry. However, even in this elongated C_{3v} geometry, the Cu(II) ground state would be a ^2E with a hole in the degenerate $d_{x^2-y^2}$ and d_{xy} orbitals, so that the site would still be Jahn−Teller active. The possible distorting symmetries for the Cu(II) C_{3v} site are given by the symmetric direct product $[E \times E] = a_1 + e$, where the Jahn−Teller force of the doubly degenerate E mode would result in a further distortion of the site from $C_{3v} \rightarrow C_s$ or C_1 symmetry, originating from a non-zero linear coupling term between the $d_{x^2-y^2}$ and d_{xy} orbitals, $\langle x^2-y^2|(\delta V/\delta Q_{\theta,\epsilon})_0|xy\rangle$, where θ and ϵ are the two components of the e vibrational mode. However, just as the elongated Met bond lowered the site from T_d symmetry, the short Cu−Cys bond, which arises to compensate for the reduced charge donation to the Cu ion brought about by the long Met bond, lowers the symmetry further from C_{3v} to C_s. From NMR MCD, the strong Cys π interaction with the Cu at the short Cu−Cys bond length splits the degeneracy of $d_{x^2-y^2}$ and d_{xy} orbitals by 10 800 cm^{-1}, quenching the remaining Jahn−Teller interaction between these levels.

In summary, other than the limited contraction of bonds arising from increased bonding with the half-occupied $d_{x^2-y^2}$ HOMO of the Cu(II), the reduced blue copper active site undergoes very little geometric distortion upon oxidation. The long Cu−Met bond and the resulting short Cu−Cys bond lower the symmetry of the copper site, removing the distorting forces in the oxidized structure and effectively trapping the Cu(II) site in a Jahn−Teller energy minimum.

V. Discussion

In this study we have developed a detailed electronic structure description of the reduced blue copper active site of plastocyanin. For the d^{10} site, the d orbitals are completely filled, and as a result, no net stabilization arises from covalent ligand interaction with these orbitals. The metal−ligand bonding at the reduced blue copper active site has been found to arise predominantly from ligand 2p/3p → Cu 4p charge transfer, with little or no contribution from metal-to-ligand π back bonding. The unusually long 2.8-Å Cu−Met bond at the reduced site results in a weak interaction relative to a normal 2.3-Å Cu−thioether bond, which greatly reduces the amount of charge donated to the Cu(I) ion. The reduced charge at the Cu center is largely compensated by a decrease in the length and an increase in the strength of the equatorial Cu−Cys bond.

Upon oxidation of the reduced site, very little change is observed in the extent of Cu 4s/4p interaction with the ligands. However, new Cu 3d bonding contributions arise as a result of the hole created in the $d_{x^2-y^2}$ HOMO when the Cu is ionized from a d^{10} to a d^9 configuration. These new 3d contributions are significant as the higher effective nuclear charge of the Cu-

(II) ion shifts the 3d manifold to deeper energy, closer to the ligand valence orbitals, enhancing covalent mixing. The methionine sulfur is oriented approximately along the z axis of the active site so that the thioether has little interaction with the $d_{x^2-y^2}$ orbital; therefore, no significant change in the Cu−Met bonding is observed on oxidation. The histidine residues exhibit limited σ overlap with the $d_{x^2-y^2}$ orbital and, as a result, experience a moderate increase in σ bonding in the oxidized site relative to the reduced site. The most significant electronic structure change upon oxidation is observed in the Cu−Cys bond. The covalent delocalization of the $d_{x^2-y^2}$ HOMO onto the thiolate is substantial so that the removal of an electron from the $d_{x^2-y^2}$ orbital results in a very strong Cu−thiolate π bond.

In the past, the high reduction potentials of blue copper proteins have generally been ascribed to the Cu(I) geometry being imposed on the Cu(II) site and to the coordination of the soft thiolate and thioether sulfur ligands to the Cu ion. Using a sterically constrained CuN_4 model as a reference, we have evaluated the electronic structure contributions to the high potential, assuming all other factors are constant, and determined the individual contribution of each ligand at the plastocyanin active site. The normal D_{2d} distortion (tetrahedral → square planar) that lowers the reduction potentials of most Cu(I) complexes by stabilizing the oxidized state is limited in the CuN_4 model by the chelating ligands. The CuN_4 model is therefore a useful reference for the blue copper site which also undergoes only limited geometry changes on oxidation. Relative to CuN_4, the short Cu−thiolate bond of the blue copper site lowers the reduction potential by stabilizing the Cu(II) state through the strong charge donation of this ligand into the $d_{x^2-y^2}$ orbital of the Cu(II) ion. At normal bond lengths, thioether would also stabilize the Cu(II) state relative to CuN_4, albeit to a much lesser extent than the thiolate anion. In the blue copper site, the axial Cu−thioether interaction at a normal bond length of ~2.3 Å would rotate the half-occupied $d_{x^2-y^2}$ HOMO, leading to better overlap with the Met ligand and greater Met charge donation to the metal center, stabilizing the Cu(II) state. However, at the long Cu−Met bond length found at the blue copper site thioether mixes very little with the $d_{x^2-y^2}$ HOMO; therefore, the axial Met ligand provides little stabilization of the Cu(II) site, resulting in the high reduction potentials of the plastocyanin and azurin type blue copper proteins. For blue copper sites with alternate axial ligand coordination, such as in stellacyanin[99] where the Met appears to be replaced by a glutamine, a stronger, shorter Cu(I)−ligand bond would tend to stabilize the oxidized site and lower the reduction potential (E° = 180 mV for stellacyanin).

The limited geometry changes that occur upon oxidation of the blue copper site include a contraction of the Cu−ligand bonds and a shift of the Cu ion toward the NNS equatorial plane. In the past, the fact that the geometry change on oxidation is small has been attributed to an entatic or rack state of the protein, which imposes the Cu(I) geometry on the oxidized site, overcoming the tendency of the pseudotetrahedral Cu(II) structure to distort toward a square-planar structure (*i.e.* the Jahn−Teller effect). In the present work, the distortions observed upon oxidation of the blue copper site have been found to be consistent with the changes in electronic structure that occur on oxidation. The Cu−His and Cu−Cys bonds contract due to increased ligand σ and π donation, respectively, arising from ligand mixing with the half-occupied $d_{x^2-y^2}$ HOMO. The Cu−Cys bond contracts to a lesser degree due to the higher force constant associated with this short, strong bond. In addition, the Cu atom shifts toward the NNS equatorial plane as the His and Cys bonding interaction with the $d_{x^2-y^2}$ HOMO is strengthened. Therefore, the protein matrix does not impose a reduced Cu(I) structure on the oxidized site. Rather, the constraints of the protein environment lower the symmetry of the reduced site from $T_d \rightarrow C_{3v} \rightarrow C_s$ through the elongation of the Cu−Met bond and the associated shortening of the Cu−Cys bond. All ground state orbital degeneracy is therefore lifted in the oxidized site, eliminating the Jahn−Teller distorting forces that are normally associated with tetrahedral Cu(II) systems.

In conclusion, the unique electronic and geometric structure of the blue copper active site derives from the elongated axial Cu−Met bond and the strong equatorial Cu−Cys bond which results from the weakened thioether interaction. The long Cu−Met bond plays a fundamental role in determining the high reduction potentials of blue copper proteins, and in limiting the distortion of the site upon oxidation which leads to a low Franck−Condon barrier to electron transfer. The strong Cu−Cys interaction results in a large anisotropic covalent delocalization of the Cu $3d_{x^2-y^2}$ redox active orbital onto the cysteine, activating this ligand as an effective superexchange pathway for electron transfer.

Acknowledgment. This research has been supported by the NSC (CHE-9217628). We would like to thank Paul Jones, Brad Reitz, and Jennifer May for their assistance in running PES experiments and the Stanford Synchrotron Radiation Laboratory, operated by the Department of Energy, Division of Chemical Sciences, for experimental time and support.

Supplementary Material Available: Tables of Cartesian coordinates and input parameters for SCF-Xα-SW calculations (14 pages). This material is contained in many libraries on microfiche, immediately follows this article in microfilm version of this journal, can be ordered from the ACS, and can be downloaded from the Internet; see any current masthead page for ordering information and Internet access instructions.

JA943745B

(99) Thomann, H.; Bernardo, M.; Baldwin, M. J.; Lowery, M. D.; Solomon, E. I. *J. Am. Chem. Soc.* **1991**, *113*, 5911−3.